



**HAL**  
open science

# Investigation of the applicability of the lattice Boltzmann method to free-surface hydrodynamic problems in marine engineering

Weijin Cao

► **To cite this version:**

Weijin Cao. Investigation of the applicability of the lattice Boltzmann method to free-surface hydrodynamic problems in marine engineering. Fluids mechanics [physics.class-ph]. École centrale de Nantes, 2019. English. NNT : 2019ECDN0011 . tel-02383174

**HAL Id: tel-02383174**

**<https://theses.hal.science/tel-02383174>**

Submitted on 27 Nov 2019

**HAL** is a multi-disciplinary open access archive for the deposit and dissemination of scientific research documents, whether they are published or not. The documents may come from teaching and research institutions in France or abroad, or from public or private research centers.

L'archive ouverte pluridisciplinaire **HAL**, est destinée au dépôt et à la diffusion de documents scientifiques de niveau recherche, publiés ou non, émanant des établissements d'enseignement et de recherche français ou étrangers, des laboratoires publics ou privés.

# THESE DE DOCTORAT DE

L'ÉCOLE CENTRALE DE NANTES  
COMUE UNIVERSITE BRETAGNE LOIRE

ÉCOLE DOCTORALE N° 602  
*Sciences pour l'Ingénieur*  
Spécialité : Mécanique des Milieux Fluides

Par

**Wenjin CAO**

## **INVESTIGATION OF THE APPLICABILITY OF THE LATTICE BOLTZMANN METHOD TO FREE-SURFACE HYDRODYNAMIC PROBLEMS IN MARINE ENGINEERING**

Thèse présentée et soutenue à Nantes, le 08/04/2019

Unité de recherche : LABORATOIRE DE RECHERCHE EN HYDRODYNAMIQUE, ÉNERGÉTIQUE ET ENVIRONNEMENT ATMOSPHÉRIQUE

### **Rapporteurs avant soutenance :**

Irina GINZBURG      Chercheur, HDR, IRSTEA, Antony Régional Centre, HYCAR  
François DUBOIS      Professeur, Conservatoire National des Arts et Métiers

### **Composition du Jury :**

Président :	Florian DE VUYST	Professeur, Université de Technologie de Compiègne
Examineurs :	Florian DE VUYST	Professeur, Université de Technologie de Compiègne
	Julien FAVIER	Maître de conférence, HDR, Aix-Marseille Université
Dir. de thèse :	David LE TOUZÉ	Professeur, École Centrale de Nantes
Co-encadrant :	Zhe LI	Maître de conférence, École Centrale de Nantes

À mes parents.



# Acknowledgments

This dissertation presents a study on free-surface hydrodynamic problems in marine engineering, using the emerging lattice Boltzmann method (LBM). It is an attempt to find an alternative numerical tool for free-surface flows and to broaden the range of applicability of the LBM. I present this dissertation as a final report and summary of the last three years of my researching work, hoping to donate my tiny contribution to the human race in the field of computational fluid dynamics (CFD), and to provide some early and basic LBM work for the *Laboratoire de Recherche en Hydrodynamique, Énergétique et Environnement Atmosphérique (LHEEA)*.

I personally regard this period of being a PhD student in France as an adventure, since it is challenging to study the LBM which is new to both the lab and me, and to work as a foreigner with a different cultural background. This work can not be accomplished without the help of my supervisors, my colleagues, my fiends and my family. I would like to dedicate this dissertation to them with my sincere respects and acknowledgments.

First of all, this PhD position is within the collaborative project between the *China Scholarship Council (CSC)* and the *École Centrale de Nantes (ECN)*. I would like to give my special thanks to *Mr. Pierre FERRANT* and *Mr. David LE TOUZÉ* for offering me this opportunity and honor to study in the ECN, and to the CSC and the ECN for their financial support.

This dissertation is under the supervision of *Mr. David LE TOUZÉ* and *Mr. Zhe LI*. I feel very lucky to work with them, since we have a harmonious working pattern. It is the constructive and sagacious instructions from David and the artful and profound technical suggestions from Zhe that make this dissertation possible. The things that I learned from them will definitely be helpful in the rest of my life, and words are not enough to express my gratitude.

I am also grateful to *Mrs. Irina GINZBURG* and *Mr. Francois DUBOIS* for accepting to be my rapporteurs, and to *Mr. Florian DE VUYST* and *Mr. Julien FAVIER* for being the committee member of my PhD dissertation defense. Their elaborate reports and their instructive suggestions during our discussions deepen a lot my understanding of the LBM.

Besides, the nice and productive talks with my colleagues are also very helpful during this PhD work, so I give my thankfulness to *Xuhui LI*, *Youngmyung CHOI*, *Chunmei XIE*, *Zhenrong JING* and *Pengnan SUN*.

Apart from the scientific work, the three years' life experiences in France is memorable and precious to me. I appreciate very much all the friends that I met in France and to those who cares about me in China. Especially, I thank *Jing CHANG* who teaches me to live elegantly and poetically, and I thank *Zhuang JIN* for accompanying me since the very beginning of this project. We start the adventure together and share many unforgettable memories. I would also like to thank *Pierre-Yves WILLAUME* and *Vincent LEROY* for kindly introducing every interesting aspects of the french culture to me. Also, I won't forget the support from *Junan ZHOU* and *Yongbo DU* in China and all the happy times with *Ran ZHU*, *Huan WANG*, *Jie YANG*, *Niannian WU*, *Xiaoqing YANG*, *Guoxin SUI*, etc.

At last, I would like to express my deepest gratitude to my family, who encourage and support me strongly with endless love.

# Abstract

The numerical simulation of the free-surface flows for marine engineering applications is a very challenging issue in the field of computational fluid dynamics (CFD). In this thesis, we propose a solution, which is to use the regularized lattice Boltzmann method (RLBM) with a volume-of-fluid (VOF) based single-phase free-surface lattice Boltzmann (LB) model, and we investigate its feasibility and its reliability.

The theoretical insights of the lattice Boltzmann method (LBM) are given at first, through the Hermite expansion and the Chapman-Enskog analysis. From this perspective, the idea of the RLBM is summarized as the Hermite regularization of the distribution functions. On the test-cases of the Taylor-Green vortex and the lid-driven cavity flow, the RLBM is verified to have a 2<sup>nd</sup>-order accuracy and an improved stability.

The adopted free-surface model is then implemented into the RLBM and validated through simulating a viscous standing wave and a dambreak flow problems. It is shown that the regularization not only strongly stabilizes the calculation by reducing spurious pressure oscillations, which is very beneficial for obtaining accurate free-surface motions, but also does not introduce any extra numerical dissipation.

Furthermore, a new reconstruction method for the distribution functions at the free-surface is proposed. The present model is more consistent with the RLBM, which provides an effective way for simulating high-Reynolds-number free-surface flows in marine engineering.

**Keywords:** marine engineering, LBM, free-surface, regularization



# Résumé

La simulation numérique des écoulements à surface libre pour les applications du génie maritime est un problème qui présente de grands défis dans le domaine de la dynamique des fluides numérique (CFD). On propose dans cette thèse une solution, qui consiste à utiliser la méthode de Boltzmann sur réseau régularisée (RLBM) avec un modèle de surface libre basé sur le volume-de-fluide (VOF), et on étudie sa faisabilité et sa fiabilité.

Les connaissances théoriques de la méthode de Boltzmann sur réseau (LBM) sont présentées dans un premier temps, sur la base d'un développement polynomial d'Hermite et d'une analyse de Chapman-Enskog. De cette perspective, l'idée de la RLBM se résume comme étant la régularisation d'Hermite des fonctions de distribution. Dans les cas tests suivants du vortex de Taylor-Green et de la cavité entraînée, il est vérifié que la RLBM possède une précision de second ordre et une stabilité améliorée.

On a alors ensuite implémenté le modèle de surface libre dans la RLBM. Sur la simulation d'une onde de gravité visqueuse stationnaire et d'un écoulement de dambreak, il est montré que la régularisation stabilise fortement le calcul en réduisant les oscillations de pression, ce qui est très bénéfique pour obtenir des écoulements à surface libre précis, et que la RLBM n'introduit pas non plus de dissipation numérique supplémentaire.

De plus, une nouvelle méthode de reconstruction des fonctions de distribution à la surface libre est proposée. Le modèle proposé est ainsi plus consistant avec la RLBM, ce qui offre un moyen efficace pour simuler des écoulements à surface libre à un grand nombre de Reynolds en génie maritime.

**Mot clés:** génie maritime, LBM, surface libre, régularisation



# Contents

<b>Symbols and Notations</b>	<b>xiii</b>
<b>1 Introduction</b>	<b>1</b>
1.1 Background and motivation . . . . .	3
1.2 A brief LBM history . . . . .	4
1.2.1 Emergence of the LBM from the LGA . . . . .	4
1.2.2 Derivation of the LBE from the CBE . . . . .	5
1.3 Challenges and improvements of the stability of the LBM . . . . .	7
1.3.1 Assessment of the numerical instability of the LBM . . . . .	7
1.3.2 Stabilization techniques for the standard LBM . . . . .	8
1.4 Existing free-surface models in LBM . . . . .	10
1.4.1 Multi-phase LB models for two fluid flows with large density ratios . . . . .	10
1.4.2 Single-phase free-surface LB models . . . . .	12
1.5 Strategy for adopting appropriate numerical tools . . . . .	14
1.5.1 Multi-phase LB models or single-phase LB models? . . . . .	15
1.5.2 Which stabilization technique to be adopted? . . . . .	16
1.5.3 Open-source software or in-house code? . . . . .	17
1.6 Outline of the thesis . . . . .	17
<b>2 Lattice Boltzmann method</b>	<b>19</b>
2.1 Boltzmann description of fluid flow . . . . .	21
2.1.1 Descriptions of fluid flow . . . . .	21
2.1.2 Continuous Boltzmann equation . . . . .	22
2.1.3 Single-relaxation-time collision model . . . . .	24
2.2 From the continuous Boltzmann equation to the lattice Boltzmann equation . . . . .	24
2.2.1 Hermite expansion of the distribution function . . . . .	25
2.2.2 Discretizing the velocity space . . . . .	26
2.2.3 Lattice Boltzmann equation . . . . .	30
2.3 Lattice arrangement . . . . .	33

2.4	Force model . . . . .	35
2.5	Multi-scale analysis . . . . .	37
2.5.1	Starting from the lattice Boltzmann equation . . . . .	37
2.5.2	Adopting Taylor expansion and multi-scale expansion . . . . .	38
2.5.3	Velocity moments of associated ingredients . . . . .	41
2.5.4	Velocity moment of $\mathcal{O}(\varepsilon^1)$ and $\mathcal{O}(\varepsilon^2)$ terms . . . . .	42
2.5.5	Specifying $\mathbf{\Pi}^{(1)}$ . . . . .	43
2.5.6	Recovering the Navier-Stokes equation . . . . .	45
2.6	Boundary conditions . . . . .	47
2.6.1	Bounce back boundary condition . . . . .	47
2.6.2	Specular boundary condition . . . . .	48
2.6.3	Zou-He boundary condition . . . . .	49
2.6.4	Periodic boundary condition . . . . .	50
2.6.5	Free-surface boundary condition . . . . .	51
2.7	Rescaling factors . . . . .	51
2.8	Algorithm . . . . .	52
<b>3</b>	<b>Regularized lattice Boltzmann method</b>	<b>53</b>
3.1	Instability analysis from the viewpoint of regularization . . . . .	55
3.1.1	Non-hydrodynamic information contained in the LBE . . . . .	55
3.1.2	Hermite regularization of the non-equilibrium distribution function . . . . .	58
3.2	Algorithm . . . . .	61
3.3	Convergency analysis of the RLBM . . . . .	62
3.4	Numerical validation on the lid-driven cavity . . . . .	64
3.4.1	Regularization-based boundary condition . . . . .	65
3.4.2	Numerical results . . . . .	69
<b>4</b>	<b>Free-surface model</b>	<b>77</b>
4.1	Free-surface representation . . . . .	79
4.2	Flag evolution . . . . .	80
4.3	Mass conservation . . . . .	82
4.3.1	Mass evolution during the streaming process . . . . .	83
4.3.2	Mass evolution due to the flag change . . . . .	84
4.4	Reconstruction of the distribution functions at the free-surface . . . . .	86
4.5	Algorithm . . . . .	88
4.6	Validations . . . . .	89
4.6.1	Viscous standing wave . . . . .	89
4.6.2	Dambreak flow . . . . .	93

---

4.7	An improved free-surface LB model . . . . .	103
4.7.1	Dilemmas of the original free-surface LB model . . . . .	103
4.7.2	A new distribution method for the distribution functions at the free-surface . . . . .	104
4.7.3	Algorithm . . . . .	106
4.7.4	Validation . . . . .	106
<b>5</b>	<b>Conslusions and perspectives</b>	<b>111</b>
5.1	Conclusions . . . . .	112
5.2	Perspectives . . . . .	113
<b>A</b>	<b>Some mathematical tools</b>	<b>115</b>
A.1	Operations on vectors and matrices . . . . .	115
A.1.1	Dot product of two vectors . . . . .	115
A.1.2	Dyadic product of two vectors . . . . .	115
A.1.3	Double dot product of two matrices . . . . .	115
A.2	Velocity moments of functions in a special form . . . . .	116
A.3	Gauss-Hermite quadrature . . . . .	116
A.4	Hermite expansion by Hermite polynomials . . . . .	116
<b>B</b>	<b>Multi-relaxation-time collision model</b>	<b>119</b>
<b>C</b>	<b>Open-source software or in-house code</b>	<b>121</b>
	<b>Bibliography</b>	<b>123</b>



# Symbols and Notations

## Latin letters

$A$	wave amplitude, equals a half of the wave height
$a$	expansion coefficient in Hermite expansion
$C$	rescaling coefficient and the coefficient of mass exchange
$c$	a lattice constant
$c_s$	sound speed
$d$	distance
$dim$	spacial dimension
$\mathbb{D}$	strain rate tensor
$E$	internal energy
$Error$	error
$f$	distribution function
$\mathbf{F}$	external force
$F_i$	discrete external force component in $i$ direction
$flag$	cell flag
$Fr$	Froude number
$\mathbf{g}$	acceleration
$H$	channel width and water level
$h$	current water depth
$\mathcal{H}$	Hermite polynomial
$\mathbb{H}$	Hilbert space
$i, j, k$	indexes, exceptionally $k$ indicates the wave number in Section <a href="#">4.6.1</a>
$\mathbf{I}$	identity tensor
$L$	physical length
$l, m, n$	indexes
$M$	cell mass
$m$	molecule mass
$Ma$	Mach number
$n, N$	a natural number
$\mathbf{n}$	unit normal vector at the free-surface

$N_I$	total number of interface cells
$p$	pressure
$p_0, p_G$	reference pressure
$p^*$	relative pressure
$q$	number of lattice speeds in a given lattice
$\mathbf{Q}$	stands for $\xi_i \xi_i - c_s^2 \mathbf{I}$
$R$	gas constant
$Re$	Reynolds number
$T$	period
$t$	time
$\mathbb{T}$	stress tensor
$\mathbf{t}$	stress vector
$U_0, U_{\text{lid}}$	characteristic velocity
$\mathbf{u}^*$	fluid velocity, only when the force model of [62] is adopted
$\mathbf{u}$	fluid velocity, only when the force model of [62] is not adopted
$\tilde{\mathbf{u}}$	dimensionless fluid velocity
$V_0$	cell volume
$v_x, v_y$	velocity component in $x$ - and $y$ -direction
$w_i$	weight, a lattice parameter
$w_i^\dagger$	weight in the inverse distance extrapolation
$w_i^M$	weight of distributing excess cell mass
$\mathbf{x}$	coordinate vector
$x, y$	$x$ - and $y$ -coordinate
$\mathbb{Z}$	integer space

### Greek letters

$\alpha$	volume fraction
$\beta$	margin
$\chi$	a parameter that distinguishes different force models
$\delta$	Kronecker delta
$\Delta t$	time increment
$\Delta x$	spacing increment
$\Delta \xi$	microscopic velocity increment
$\epsilon$	wave steepness
$\varepsilon$	a small positive parameter used in the multi-scale expansions
$\tilde{\boldsymbol{\eta}}$	a vector used in variable substitution
$\boldsymbol{\Gamma}$	3 <sup>rd</sup> -order moment of a distribution function
$\lambda$	wavelength
$\mu$	dynamic viscosity

$\nabla$	nabla symbol, used in gradient operator and divergence operator
$\nu$	kinetic viscosity
$\omega$	weighting function, exceptionally indicates the wave frequency in Section 4.6.1
$\Omega$	collision operator
$\phi$	an arbitrary variable used for explaining a definition
$\varphi$	velocity potential
$\pi$	Pi constant
$\mathbf{\Pi}$	2 <sup>nd</sup> -order moment of a distribution function
$\Psi$	a polynomial
$\rho, \rho_0$	fluid density
$\tau$	dimensionless relaxation time
$\boldsymbol{\tau}$	unit tangential vector at the free-surface
$\Theta$	temperature
$\tilde{\Theta}$	dimensionless temperature
$\boldsymbol{\xi}$	microscopic velocity
$\tilde{\boldsymbol{\xi}}$	dimensionless microscope velocity
$\zeta$	bulk viscosity

### Superscripts

$\square^{\text{ana}}$	analytical result
$\bar{\square}$	inversed direction
$\square^{\text{eq}}$	equilibrium state variables
$\square^{\text{lat}}$	lattice value
$\square^{\text{neq}}$	non-equilibrium state values
$\square^{\text{num}}$	numerical result
$\square^{\text{orig}}$	variables of the standard LBM without adopting the force model in [62]
$\square^{\text{pc}}$	post-collision values
$\square^{\text{phy}}$	physical value
$\square^{\text{T}}$	transposition operator

### Subscripts

$\square_{\text{ex}}$	exceeded value above the limit
$\square_{\text{max}}$	maximum value
$\square_{\text{receive}}$	received value from neighboring cells
$\square_{\text{Ref}}$	reference result

### Other notations

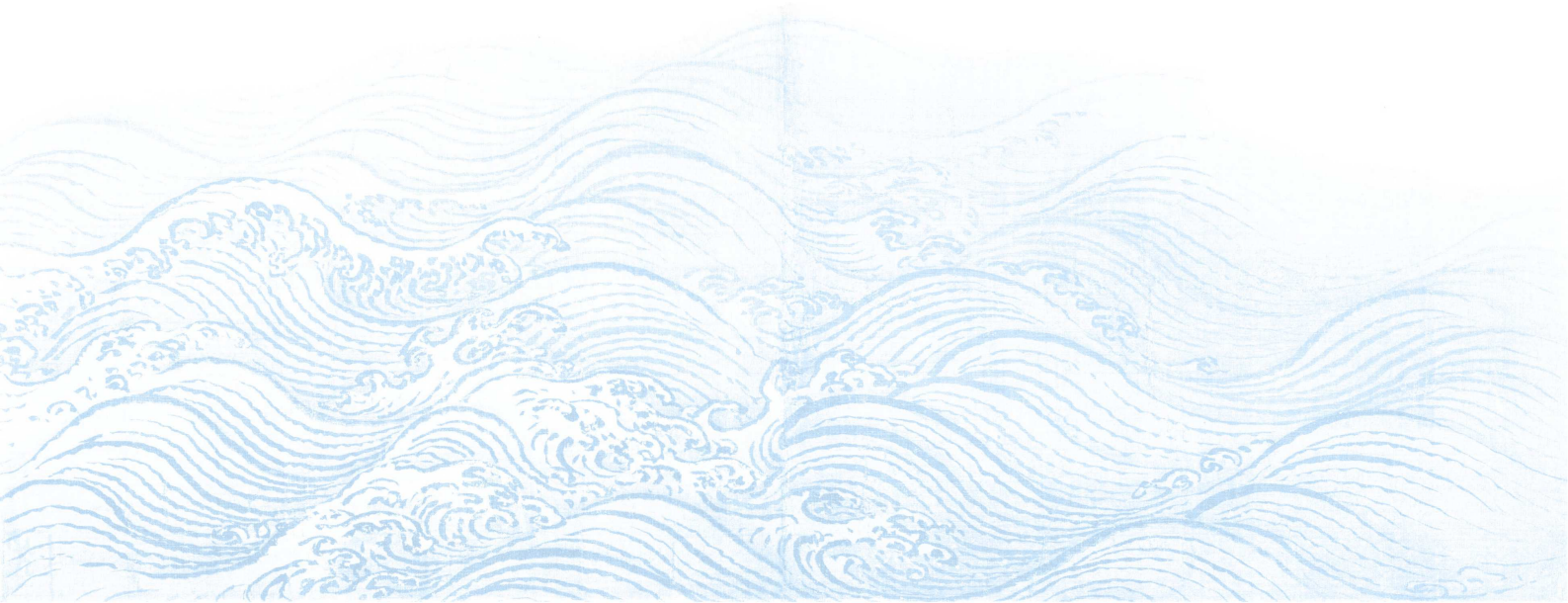
D	a differential operator
$DdQq$	a $d$ -dimensional lattice with $q$ lattice speeds
G, I, L	cell flag types, respectively stands for gas, interface and liquid
H1-4	locations of water height sensors
P1-4	locations of pressure sensors

# Chapter 1

## Introduction

This chapter consists of three principal parts. The first part illustrates the demand of a reliable numerical tool for simulating free-surface flows, which motivates the present study on the lattice Boltzmann method (LBM) for free-surface flows. In the following part, the LBM history, the existing stabilization techniques for LBM and the state-of-the-art of free-surface models for LBM are reviewed, respectively. Finally, the selection of the adopted free-surface model and stabilization technique, as well as the choice of developing an in-house code, are explained. The outline of the thesis is listed in the end.

Ce chapitre comprend trois parties principales. La première partie illustre la motivation de cette étude quant à l'utilisation de la LBM pour simuler des écoulements à surface libre, qui fait face à la demande d'un outil numérique fiable dans ce domaine. Dans la partie suivante, sont respectivement revus l'histoire de la LBM, les techniques existantes pour stabiliser la LBM, et l'état de l'art des modèles de surface libre pour la LBM. Enfin, la sélection du modèle de surface libre adopté et de la technique de stabilisation utilisée sont expliquées, ainsi que le choix de développer un code interne. Les structure de cette thèse est présentée à la fin.



## Contents

---

<b>1.1</b>	<b>Background and motivation . . . . .</b>	<b>3</b>
<b>1.2</b>	<b>A brief LBM history . . . . .</b>	<b>4</b>
1.2.1	Emergence of the LBM from the LGA . . . . .	4
1.2.2	Derivation of the LBE from the CBE . . . . .	5
<b>1.3</b>	<b>Challenges and improvements of the stability of the LBM . . . . .</b>	<b>7</b>
1.3.1	Assessment of the numerical instability of the LBM . . .	7
1.3.2	Stabilization techniques for the standard LBM . . . . .	8
<b>1.4</b>	<b>Existing free-surface models in LBM . . . . .</b>	<b>10</b>
1.4.1	Multi-phase LB models for two fluid flows with large density ratios . . . . .	10
1.4.2	Single-phase free-surface LB models . . . . .	12
<b>1.5</b>	<b>Strategy for adopting appropriate numerical tools . . .</b>	<b>14</b>
1.5.1	Multi-phase LB models or single-phase LB models? . . .	15
1.5.2	Which stabilization technique to be adopted? . . . . .	16
1.5.3	Open-source software or in-house code? . . . . .	17
<b>1.6</b>	<b>Outline of the thesis . . . . .</b>	<b>17</b>

---

## 1.1 Background and motivation

The computational fluid dynamics (CFD) has been of great significance and attention in marine engineering researches of the last decades, since it is both less expensive and more risk-free than full-scale experiments, and also able to provide numerical approximations of the governing equations for fluid flows, for which the fluid mechanics theory cannot provide exact solutions. Owing to the fast development in computer science and the prosperous pioneer works in advanced numerical methods, CFD is now adapted into powerful tools, and still has much potential for further amelioration. One of the challenging direction of amelioration is the free-surface problems in marine engineering. Among those, one can give examples as the advance of a ship on the free-surface, the motion of offshore structures like the floating production storage and offloading units (FPSOs), the behavior of renewable marine energy converters in waves, etc. All these applications share some common ingredients, such as fluid-structure interaction, large density ratio, moving free-surface and even large deformation like in wave breaking, which bring large difficulties for CFD simulations. To provide a reliable numerical tool for such phenomena with good performance on both accuracy and efficiency, much efforts are in demand.

One of the successful numerical method for marine sciences is the inviscid potential flow theory, which is combined with the boundary element method (BEM) using the complex Green function or Rankine source on the fluid-structure interface and free-surface with some far-field boundary condition. The potential theory plays a pivotal role in solving linear physical problems. Nevertheless, highly nonlinear situations and viscous effects, for example wave breaking and merge, water entry, boundary layer separation, etc., are beyond the capability of the potential theory [131, 112]. In this aspect, the CFD methods directly solve the viscous Navier-Stokes (N-S) equations, and are able to capture nearly all the nonlinear hydrodynamic effects. As a price, conventional incompressible CFD methods compute the pressure by solving a Poisson equation, which involves global data communication and turns out to be time-consuming [115]. Other limitations of the conventional CFD can be seen as the existence of nonlinear convective terms and the hardness of implementing boundary conditions on complex geometries [115, 77]. Indeed, there do exist a substitutive category of methods, called the meshfree methods, of which the smooth particle hydrodynamics (SPH) [48, 128] and the moving particle semi-implicit method (MPS) [95] are two representatives. The mesh-free methods use free-moving Lagrangian particles to describe the fluid, thus eliminate the convection term and simplify the treatment of boundary conditions at material surfaces. In this thesis, another alternative method is spotlighted,

which is the lattice Boltzmann method (LBM).

The LBM is based on the continuous Boltzmann equation (CBE), which describes the motion of microscopic molecules. Strict mathematical proof shows that the lattice Boltzmann equation (LBE) is a special discretization of the CBE, and that the N-S equations are recovered from the LBE if proper lattice parameters are chosen, despite the information loss during the discretization [158]. The details of the LBM will be elaborated in the rest of the thesis, but one is still able to summarise the advantages of the LBM from the literature. Firstly, the complex convection is reduced to a simple advection by distribution function streaming. Secondly, the LBM gets rid of solving any Poisson equation. Lastly, the data communication is always local, which is ideal for parallel computing. Besides, the LBM has been shown to have a 2<sup>nd</sup>-order accuracy both in time and space. Despite these appealing features of the LBM, its imperfections can also be assessed [162] mainly in the fact that the requirement for lattice symmetry determines the lattice to be a uniform space-time grid which is not well suited to body-fitted coordinates and adaptive time-stepping, that it is not a good choice for steady-state computation due to its explicit solving, and that the boundary treatment sometimes becomes laborious although the underlying mechanism is simple.

Fairly speaking, the benefits of the LBM largely outweigh its demerits, which motivates the author to investigate the applicability of the LBM into the free-surface hydrodynamic problems.

## 1.2 A brief LBM history

### 1.2.1 Emergence of the LBM from the LGA

In the past three decades, the study of the LBM has become a flourishing branch of numerical methodologies for simulating fluid flows. Modern researches often start directly from introducing the LBE. The standard LBE with a single-relaxation-time (SRT) Bhatnagar-Gross-Krook (BGK) [12] collision operator reads

$$f_i(\mathbf{x} + \boldsymbol{\xi}_i \Delta t, t + \delta t) - f_i(\mathbf{x}, t) = -\frac{1}{\tau} [f_i(\mathbf{x}, t) - f_i^{\text{eq}}(\mathbf{x}, t)]. \quad (1.1)$$

If one takes for granted the classic forms of the collision operator, the streaming rule, the symmetric characters of the chosen lattices, as well as the various boundary conditions, it is able to build up simple codes to simulate fluid flows without encountering too many difficulties. However, it may be more helpful for the understanding of the underlying physics if one keeps in mind some knowledge about the historical origin of the methodology. Dating back in time, one can

find out that the LBM has an intimate relation with its precursor, the lattice gas automata (LGA). The LGA stands on a microscopic viewpoint by defining a boolean population variable, which indicates the presence state of the particles at the lattice nodes. The evolution of the boolean population describes the particle behavior that each particle can move to its nearest lattice node within one time unit and change its direction immediately at its arrival due to some scattering rules [26]. After an averaging process over calculations of large regions of the lattice, long times and a wide range of initial conditions, the macroscopic flow fields can be approximately obtained [11]. In 1973, Hardy, de Pazzis and Pomeau (HPP) [64, 63] casted the LGA evolution on a square lattice and observed two typical hydrodynamical modes, the sound waves and the vorticity diffusion. Nevertheless, the HPP model failed to fully reproduce the N-S equations due to the lack of isotropy of their lattice [11]. This problem was solved by Frisch, Hasslacher and Pomeau (FHP) [45] with a triangular lattice for 2-dimensional cases and by d’Humière et al. [37, 44] with the face-centered hypercubic (FCHC) lattice for 3-dimensional cases. However, as pointed out in [142], although these models are suitable for parallel processing and irregular boundary conditions, they have the common disadvantages of large statistical noises. In order to remove this noise, McNamara and Zannetti [132] proposed to substitute the boolean population in the LGA evolution equation with an ensemble-averaged one under the Boltzmann assumption of molecular chaos, making it more efficient than the original post-averaging LGA [90, 162]. This work is regarded as an important stepping stone as the earliest LB scheme for simulating hydrodynamic problems [162]. Inspired by this, a series of developments were intensively achieved in the following several years. Higuera and Jiménez [73] expanded the distribution function about its local equilibrium value and thus linearized the collision operator. Later on, Qian et al. [140] further simplified the calculation by replacing the collision operator with a relaxation process with one single relaxation coefficient, which coincided with the SRT model proposed by BGK [12]. In the same year, Chen et al. [24] obtained a similar SRT model and proved it to be not only inheritably noiseless but also able to eliminate the nonphysical effects of the FHP model in terms of the non-Galilean invariance and the velocity-dependent equation of state.

### 1.2.2 Derivation of the LBE from the CBE

The aforementioned articles briefly outline the historical story of the birth of LBM within a LGA configuration. Alternatively, another branch of studies showed that the LBM can be directly derived from the continuous Boltzmann equation (CBE), and such an a priori derivation is completely independent of the LGA [69]. Starting

from the continuous Boltzmann equation with the BGK collision operator, He and Luo [68] obtained the  $D2Q9$  lattice Boltzmann equation by discretization in both time and space. Not long after, they provided more details of the derivation from the CBE to the LBE in their following paper [69]. By integrating the CBE over a time step along its characteristic line, the CBE was discretized in time and 2<sup>nd</sup>-order accuracy in time was proved. Besides, they showed that with a properly chosen lattice (where the weighting function and lattice speeds along the lattice directions are specifically designed) and a coupled equilibrium distribution function, the hydrodynamic macroscopic variables can be precisely calculated on the discretized phase space and the necessary symmetries required by the N-S equations are retained. As a demonstration, they carried out such a discretization procedure on  $D2Q6$ ,  $D2Q7$ ,  $D2Q9$  and  $D3Q15$  lattices. Furthermore, He and Luo [67] illustrated the recovery of the incompressible N-S equations from the LBE through a multi-scale Chapman-Enskog analysis. The works in [68, 69, 67] carefully proved that the LBE is a special discretized form of the CBE [115], and that the LBM is a very good alternative incompressible solver of the N-S equations. Likewise, the same fundamental findings of the LBM theory were published by other researchers almost simultaneously with He and Luo, in the fruitful period of the 1990s. For example, Abe [1] pointed out, as what He and Luo stated in [69], that the equilibrium distribution function is in fact a truncated small velocity expansion of the Maxwell-Boltzmann distribution, and that the discrete lattice velocities turn out to be the abscissae of the Gaussian-Hermite quadratures to ensure the accurate evaluation of the hydrodynamic moments of the distribution functions. Shan and He [157] provided a clearer mathematical proof of such features. Nevertheless, rigorous and systematic analysis of the underlying physics of the LBM was in lack in the existing literatures until Shan et al. [158] published their phenomenal paper in 2006. Based on the sound mathematical ground of Hermite expansion, Shan et al. projected the Boltzmann-BGK equation onto the Hermite basis, including the equilibrium distribution function. Then they proved that different levels of macroscopic conservation equations can be recovered from the LBE if the Hermite expansions are truncated at sufficient orders. For instance the leading 2<sup>nd</sup>-order terms are enough for hydrodynamic equations and a truncation up to the 3<sup>rd</sup>-order is necessary for thermo-hydrodynamic equations. In short, the LBM was revealed to be a powerful tool for solving even beyond the N-S equation with a sound theoretical basis.

## 1.3 Challenges and improvements of the stability of the LBM

### 1.3.1 Assessment of the numerical instability of the LBM

The CBE governs the evolution of the fluid particles with a Maxwellian velocity distribution function, of which the macroscopic behavior follows the N-S equations of fluid flows [143, 70]. From the admirable works listed in the former Section 1.2.2, one can understand that the N-S equations are ultimately the macroscopic statement of mass and momentum conservation, which are not sensitive to the details of the underlying microscopic dynamics [11]. In other words, although the CBE is discretized on a discrete velocity space and some high-order components in the equilibrium distribution function are casted away, the basic ingredients at the macroscopic N-S level are still retained [11, 158]. In this spirit, the LBM is developed to use the simplest microscopic description that gives the macroscopic behavior of interest [161]. However, numerical instability arises during such a simplification. The cause of the instability has been noticed and explained by several authors [161, 22, 26, 182, 137]. Among those, Cao et al. [22] argued that in terms of the Courant-Friedricks-Lewey (CFL) condition which meets the requirement for stable numerical schemes, this CFL condition is usually marginally satisfied or even not satisfied in the common lattice arrangements, which gives rise to instability for small viscosities. Others held an opinion based on the traditional kinetic theory. In traditional kinetic theory, the  $H$ -theorem states that the Maxwellian equilibrium distribution function corresponds to the maximum entropy state, hence the relaxation from any initial state towards the equilibria experiences an increase of entropy and subsequently ensures the complete stability of the CBE. However, the  $H$ -theorem is no longer satisfied in the LBE, where only a small set of discrete velocities is used and the Maxwellian equilibrium distribution function is substituted by its truncated expansion. Since the  $H$ -theorem is not guaranteed, the LBM is subjected to numerical instability. In this context, stability analysis is imposed to the LBM. A von Neumann linearized stability analysis was carried out by Sterling and Chen [161] and Worthing et al. [179], and conclusions were made that the LBM is linearly stable for positive viscosities, i.e. when the dimensionless relaxation time  $\tau$  is bigger than 0.5. In addition, several other analyses were reported by Lallemand and Luo [99] and Ricot et al. [145]. They found that the LBM is stable when the mean flow velocity is below a maximum value which is associated with the sound speed, the relaxation time and the wave number. Moreover, evidence accumulates from various researchers such as Chen et al. [27] and Behrend et al. [10]. All these investigations pointed to a common knowledge that

the LBM encounters instability when the dimensionless relaxation time is close to 0.5. For high-Reynolds number problems, the relaxation time inevitably approaches 0.5, which makes it very challenging for LBM computation. Additionally, numerical instability can also be generated from inadequate initial conditions, geometric singularities or in regions with large numerical approximation like at the interface of grid refinements [145].

### 1.3.2 Stabilization techniques for the standard LBM

Many researches have been reported in literature, aiming to alleviate the numerical instability of the standard SRT-LBM at high Reynolds numbers. In this section, all the different stabilization techniques are included to the best knowledge of the author.

**Multi-relaxation-time lattice Boltzmann method** The multi-relaxation-time lattice Boltzmann method (MRT-LBM) revives the early form of the LBM scheme where the collision is described by a scattering matrix (as previously reviewed in Section 1.2.1). The basic idea is to construct a generalized LBE in the moment space based on a given discrete velocity set [35], hence allowing the resulting moments to be relaxed in freely adjustable rates which are known as the multiple relaxation times [99]. Such a separation of the relaxation rates for different physical and kinetic modes was shown to effectively enhance the numerical stability [99, 96, 125]. Indeed, there exists another MRT scheme proposed by Shan and Chen [156], which was derived from a Hermite expansion representation of the LBE. The most widely used MRT-LBM scheme refers to the one introduced by Lallemand and Luo [99] and d’Humière et al. [36]. Unfortunately, the large freedom of choosing the multiple relaxation times leads to a new problem, which is that there is not yet a universal principle for optimizing the parameter choosing strategy, despite that several well-known value sets were given in [99, 123] and some nice tries could be seen such as the adjoint lattice Boltzmann model for parameter identification proposed by Tekitek et al. [168].

**Two-relaxation-time lattice Boltzmann method** The two-relaxation-time lattice Boltzmann method (TRT-LBM) was carefully and comprehensively introduced by Ginzburg et al. in [57], based on the former works of Ginzburg [51, 52, 53, 54]. The two relaxation times correspond to the relaxation rate of the symmetric and anti-symmetric components of the distribution function. If properly choosing the free relaxation parameter, it is expected to perform better stability and to reduce the spatial errors with respect to the standard SRT-LBM

[57]. It is also noticed that the TRT-LBM can be regarded as a special form of the MRT-LBM, and the SRT-LBM can be obtained if the two relaxation times are equal.

**Cascaded lattice Boltzmann method** Geier et al. [46] came up with a cascaded LBM scheme which is closely related to the MRT-LBM. They regarded the relaxation as an act on the central moments defined in the reference frame moving with the fluid. Because the central moments can be expressed as a polynomial of the raw moments defined in the fixed lattice reference frame up to the same order, it was pointed out that the relaxed raw moments by MRT-LBM will affect higher order central moments, and they identified this insufficient degree of Galilean invariance as a source of instability [46, 126]. Therefore in the cascaded LBM, the relaxation parameters are adjusted in a single way from low orders to high orders, and a non-commuting collision operator is constructed. With support from sufficient lattices, a stabilized collision operator with higher order of Galilean invariance is achieved. Moreover, Dubois et al. [38] presented a LB scheme with relative velocities that the velocity moments of distribution functions are dependent on an arbitrary velocity field, which provided a generalized form for the cascaded LBM and the MRT-LBM.

**Entropic lattice Boltzmann method** Recalling the statements in Section 1.3.1, the numerical instability of the LBM is caused by the lack of the  $H$ -theorem. In this context, a possible way to enhance the LBM stability is to comply a discrete entropy  $H$ -theorem [145]. Some early works were done by Karlin et al. [88, 87] and Wagner [176], and an entropic lattice Boltzmann method (ELBM) was introduced by Karlin et al. [86] later. For a chosen  $H$  function, the collision operator should guarantee a non-increasing  $H$  value [13]. The ELBM firstly finds an equivalent state which is of same entropy level in the  $H$  function and another state with the maximized entropy. Then an over-relaxation parameter is chosen to relax the distribution function to a middle state between the equivalent state and the maximum entropy state. By re-introducing the  $H$ -theorem to the LBM, the ELBM has been validated to be a stabilized LB scheme by various researchers [5, 4, 29, 89].

**Regularized lattice Boltzmann method** Compared with other stabilization methods, the regularized lattice Boltzmann method (RLBM) is theoretically straightforward, easy to implement, and effective. Based on the sound ground of the Hermite formulation of the LBE [158], the regularization concept is to construct a set of pre-collision distribution functions that are only related to the macroscopic hydrodynamic moments, while the higher order components are fil-

tered out [134, 163, 21]. Different regularization techniques have been proposed and investigated in the literature. For example, through the Chapman-Enskog analysis, Latt and Chopard [100, 101] proposed to reconstruct the non-equilibrium part of the pre-collision distribution function using the gradient of the macroscopic fluid velocity. In the same spirit, Latt et al. [102] also proposed a straight velocity boundary condition treatment. Another regularization procedure was introduced by Zhang et al. [189] where the non-equilibrium part of the pre-collision distribution function was projected onto the Hilbert sub-space spanned by the Hermite polynomials. Both these procedures are simple extensions of the original SRT-LBM scheme, therefore an overall simplicity can be inherited in the RLBM. The effectiveness of the RLBM in terms of enhancing the stability was validated by various tests [138, 82, 127].

**Some other stabilization strategies** Li et al. [111] observed the appearance of negative values in the distribution function under low viscosity condition and the accompanying instability. To prevent the negative distribution function from occurring, they simply allowed the relaxation time to locally increase in order to ensure the positivity of distribution functions. Qian [141] and Fan et al. [41] proposed another solution based on the fractional volumetric LB scheme [23, 188], where numerical dissipation was added. The mechanism is to introduce a numerical diffusion at higher than the viscous order (the so-called hyper-viscosity effect). Similarly, by testing different interpolation schemes of the LBE, Niu et al. [137] found out that the upwind interpolations are more stable than the central interpolations because of the hyper-viscosity effect. Alternatively, Ricot et al. [145] designed a selective viscosity filtering method, of which the filter coefficients are optimized in the Fourier space. This filter damps the unphysical instabilities without affecting the physical shear and acoustic waves. In addition, Dellar [33] showed that a larger bulk viscosity is helpful for better stability. Hence a method that adjusts the bulk viscosity independently from the shear viscosity was introduced in [33].

## 1.4 Existing free-surface models in LBM

### 1.4.1 Multi-phase LB models for two fluid flows with large density ratios

Physically, the free-surface flow in marine engineering can be classified into multi-phase flows with a density ratio of the liquid density to the gas density as large as  $1.0 \times 10^3$ . In the past two decades of profuse developments in the LBM, the multi-

phase problem has always been one of the most attractive issues. Several numerical models for simulating multi-phase flows have been inserted into the LBM. These models were reviewed by Li et al. [110] and Liu et al. [121] independently in 2016 in their retrospective papers, in which four major categories were distinguished, i.e. the color-gradient model, the free-energy model, the pseudo-potential model and the phase-field model. Here, the author keeps this four-category classification while examining the existing multi-phase LB models.

**The color-gradient LB model** The color-gradient LB model simulates two immiscible fluids with two colored particle distribution functions. Its title "color-gradient" comes from the fact that the interface is located where the local color gradient reaches the maximum value. In the collision step, a perturbation is added to the particle distribution near the interface, and a following recoloring step is designed to redistribute the mass with a zero mass diffusivity of one color into the other, and subsequently ensure a separation of the two fluids. This idea was firstly proposed by Rothman and Keller [147] for the FHP lattice-gas model and later brought to the LBM by Gunstensen et al. [60]. The model of Gunstensen et al. [60] is only suitable for two fluids with same density and viscosity. It is extended by Grunau et al. [58] for two fluids with unequal densities and viscosities in a  $D2Q7$  lattice and later by Tölke et al. [175] for a  $D3Q19$  lattice. Besides, the original model in [60] is also improved by Lishchuk et al. [119] by modifying the perturbation step and by Latva-Kokko and Rothman [103] and Reis and Phillips [144] with adapted recoloring rules.

**The free-energy LB model** The free-energy LB model was firstly introduced by Swift et al. [166, 165], where a non-ideal thermodynamic pressure tensor was included into the 2<sup>nd</sup>-order moment of the distribution function, enabling the phase separation to be governed by the non-ideal equation of state [110]. However, Luo [124] criticised that this model suffers from several drawbacks such as leading to incorrect energy balance equation, among which the non-Galilean invariant nature has also been widely noticed by other researches [165, 70, 79]. In this context, studies were made to bring back the Galilean invariance by adding some correction terms to the distribution function [79, 85, 139]. What is more, Wagner [177] and Pooley and Furtado [139] observed spurious velocities around the interface between the two fluids due to the fact that the interfacial tension force was introduced by imposing additional constraints on the equilibrium distribution function. The free-energy model is also extended to simulating bubble motion under gravity [167] by considering buoyancy effect and to investigating contact line motion [20] by introducing a wetting boundary condition.

**The pseudo-potential LB model** The pseudo-potential LB model, proposed by Shan and Chen [154, 155], defines an inter-particle potential based force to mimic particle interactions. This model owes its great popularity to its simplicity in the sense that the inter-particle force is written in a general form for every lattice node and the automatic phase separation frees the model from extra interface tracking or capturing operation. In contrast, the demerits of the model can be summarized [25] as: the existence of spurious currents, the thermodynamic inconsistency and the limited density and viscosity ratios. In response to these issues, several countermeasures were developed in the literature. Shan [153] and Sbragaglia et al. [151] identified the cause of the spurious velocities as the anisotropic contributions of the discrete gradient operator. Yuan and Schaefer [186] and Zhang and Tian [187] incorporated different equations of state into the model, trying to reduce the spurious velocities. Incorporating realistic equations of state was also found to be useful for larger density ratios [97, 8]. Besides, improved forcing terms were proposed by Huang et al. [75], Li et al. [109] and Sun et al. [164]. It is also found that when adopting relatively more stable LB schemes like the MRT-LBM, the applicable density ratios increased as a by-product effect [151, 185].

**The phase-field LB model** The phase-field LB model came up in the work of He et al. [66, 71], where an index distribution function and a pressure distribution function were employed, instead of only one density distribution function used in the original LBM. As pointed out by Lee and Lin [106], the evolution of the index distribution function leads to a macroscopic equation that is similar to the Cahn-Hilliard equation which describes the phase separation [83], hence Li et al. [110] classified this model into the phase-field category. Similarly to the strategy used by He et al. [66, 71], Inamuro et al. [80] and Lee and Lin [107] proposed their two-distribution-function systems, where Cahn-Hilliard-liked equation can be recovered. Zheng et al. [191] noted that the Cahn-Hilliard equation was not truly recovered by the three mentioned models [66, 80, 107], and provided a modified discretization form of the LBEs for the index distribution function and a newly defined distribution function for the average density of the two fluids. Additionally, there exist other extensions of Inamuro's, Lee's and Zheng's model, which made efforts to simulate multi-phase flows with large density ratios [108, 39, 81].

### 1.4.2 Single-phase free-surface LB models

A typical feature of marine free-surface flow phenomena is that the liquid flow is usually considered to be free from being affected by the gas motion. Such a common assumption enables one to use single-phase models for free-surface simulation. This

assumption is valid for the liquid flow up to when gas is entrapped within the liquid. When the latter occurs, this assumption is questionable as investigated in [129]. As an alternative to the multi-phase models in simulating free-surface flows, the single-phase models are innovated by the idea of reducing the multi-phase flow with phase separation to a single-phase approach with a free-surface boundary. In this spirit, Ginzburg et al. [50, 56] proposed a free-surface model within the color-gradient framework, where the small density phase is considered as vacuum and the original recoloring step is replaced by a boundary condition based on the local 2<sup>nd</sup>-order boundary method [49].

**VOF-based LB models** Körner et al. [94] developed a free-surface model directly in a single-phase fashion. They borrowed the free-surface representation from the volume-of-fluid (VOF) method, where the cell flag is labeled by the variable of liquid volume fraction. The mass flux calculation between lattice cells is a built-in operation in the streaming step, and the unknown distribution functions on the interface are given by a dynamic boundary condition that ensures a balanced hydrodynamic force against the gas pressure. The free-surface evolution is driven by the cell mass change, which means the cell flag shall change if the volume fraction reaches zero or one. As a complement to the original model, Thürey et al. [171] described the meticulous rules of the flag evolution. Thürey et al. [172] introduced a scheme with adaptive time-steps. Thürey and Rüde [173] employed the free-surface model on adaptively refined grids by implementing a LB turbulence model [160, 74, 184], adaptive time-step [172], and grid refinement technique [43]. Besides, this model was extended for thermal free-surface flows with liquid-solid phase transition [7]. Further, though this model involves careful operations on cell mass computing and flag change, the total number of required operations for interface cells is a small percentage within the whole domain, which guarantees an overall simplicity and good efficiency. Thanks to its easy implementation, this family of free-surface model has been used in various problems such as bubble motion [3], wetting effect [6], droplet falling [180, 159], floating body [16], viscous wave [190], metal foaming [94, 91], electron beam melting [92, 93, 9, 2], physical animation [174, 170], etc.

Another free-surface model was introduced by Janssen and Krafczyk [84], which is very similar to Körner's model [94]. Instead of using a cell-centered lattice as done in [94], Janssen and Krafczyk constructed a node-centered lattice which is more friendly for the mass flux calculation with grid refinement technique. In terms of the free-surface boundary, the reconstruction of the unknown distribution function on the interface remained the same as in [94], whereas a piecewise linear reconstruction method (PLIC) [183, 59] was adopted for free-surface capturing.

They also used a LB turbulence model [96] and the MRT-LBM scheme [36] to achieve better stability for high Reynolds numbers.

**Level-set LB model** In addition, Thürey and Rüde [148] mentioned a level-set free-surface model based on the free-surface model in [94], where a level-set front tracking method [152] was used to determine flag change. The benefits are a smooth surface in case of insufficient number of particles and the easy calculation of the normal vector and the curvature. However, the mass conservation cannot be perfectly guaranteed.

As an appraisal, the single-phase models serve as a successful substitute for multi-phase models in free-surface simulations. Indeed, the physical nature of the free-surface is a fluid-fluid interface, but the common hypothesis of the negligible influence of the gas makes the single-phase model feasible in the limit already mentioned that the air phase is not significantly mixed in the liquid. Moreover, the absence of calculation in the gas domain not only massively saves computational time but also avoids the great difficulty of dealing with large density ratio in multi-phase models. In return, it requires careful treatment of the free-surface boundary.

**LBM for shallow-water** We should also mention here the LB models for simulating shallow-water flows where a free-surface naturally exists. It is a branch of the LBM targeting the shallow-water equations, which can be derived from depth-integrating the N-S equations under the assumption that the horizontal length scale is much greater than the vertical one [169]. The shallow-water LB model was introduced by Salmon [149, 150] for studying ocean circulation due to the planetary geostrophy. Various applications have been simulated using this model, such as wind-driven ocean circulation [118], two-layers shallow-water flow [146], tidal waves [192], flows in open channel junctions [120], etc. However, if one seeks a general free-surface model without being constrained by the shallow-water limit, or if one wants to study complex free-surface flows like wave breaking, these shallow-water models shall be discarded.

## 1.5 Strategy for adopting appropriate numerical tools

In order to make use of the previously reviewed various free-surface LB models and stabilization techniques for marine engineering applications, one should determine a strategy of establishing a reliable numerical tool, by answering to the following three questions:

- (i) Which one to choose among the existing free-surface LB models?
- (ii) Which stabilization technique is ideal for free-surface LB computing?
- (iii) Whether find and learn how to use an open-source software or develop an in-house code?

### 1.5.1 Multi-phase LB models or single-phase LB models?

The single-phase free-surface models automatically dodge the difficulty of the large ratio at the water-air interface. Therefore, it is very interesting and important to assess the capacity of dealing with large density ratios of the four mainstream multi-phase free-surface LB models that are mentioned in Section 1.4.1.

Firstly, the original phase-field model [60] can only be applied to two fluids with same density. In the later version suitable for density variations [58], tests with a density ratio of  $\mathcal{O}(10)$  were presented. Meanwhile, it was noticed in [58] that this model cannot simulate high velocity flows due to the inevitable accumulation of rest particles in the embedded operation of high particle mass ratio assignment. The possible density ratio was improved to  $\mathcal{O}(100)$  by Leclaire et al. [105]. Later on, Lesclaire et al. [104] showed a simulation with a density ratio of  $\mathcal{O}(1000)$ , but only for steady bubbles. These evidences coincide with the comments in [58, 121, 110] that the applicable density ratio for color-gradient model can be up to  $\mathcal{O}(1000)$  for stationary bubble or droplet tests, whereas it is restricted to  $\mathcal{O}(10)$  for dynamic problems due to numerical instability.

Secondly, to the best of the author's knowledge, the free-energy model has not been frequently used for large density ratio fluids. From the original model of Swift et al. [166, 165] to its extensions in [79, 167], the presented test-cases are of a density ratio less than 10. Distinctively, Mazloomi et al. [30] adopted the ELBM for stable calculation and succeeded to simulate a bubble motion with a density ratio of  $\mathcal{O}(100)$ . The cause of the instability of the free-energy model at large density ratios were assessed [110] as the common operation in the mentioned papers of adding density-gradient associated correction terms in order to remove the non-Navier-Stokes terms in the macroscopic equations.

Thirdly, as for the pseudo-potential model, its early forms also start from low density ratios about  $\mathcal{O}(10)$  [40, 25]. Several advanced techniques have been proposed including modifying the equation of state [186, 187], increasing the isotropy order of the inter-particle interaction force [153, 151], improving the forcing term [97, 75, 109, 164] and adopting stable collision operators [151, 98, 185]. All these improvements are beneficial in enlarging the density ratio range, for an example the density ratio was reported to be able to reach  $\mathcal{O}(100)$  in [151] and  $\mathcal{O}(1000)$

in [186, 185, 75].

Lastly, among the implementations of the phase-field category for large density ratios, the more representative models are those proposed by Inamuro et al. [80], Lee and Lin [107] and Zheng et al. [191]. The original Inamuro's model [80] is applicable for density ratios only of  $\mathcal{O}(50)$  but it was renovated to  $\mathcal{O}(1000)$  in a recent version by Inamuro et al. [81]. The other two, i.e. Lee's model [107] and Zheng's model [191], tolerate density ratios of  $\mathcal{O}(1000)$  since their emergence. Many applications of these models can be found in the literature including but not limited to [181, 135, 28, 108, 178]. However, one should be aware of the other side of the coin. Consensual critical statements can be found in [191, 39, 110] that Inamuro's model involves solving a Poisson equation for pressure correction which reduces the efficiency, and that Lee's model not only is powerless for large velocity flows and fast deformation but also executes different discretization forms for the gradients before/after the streaming step which adds some extra complexity. Furthermore, [39, 110] analyzed Zheng's model and demonstrated its shortcoming of using the distribution function for the mean density of both phases, so that the numerical tests on two fluids with different combination of densities will produce exactly the same results if the average value of the two fluid densities is kept the same.

To summarize, compared with the color-gradient model and the free-energy model, the pseudo-potential model and the phase-field model are relatively more effective in simulating large-density-ratio multi-phase flows (up to  $\mathcal{O}(1000)$ ) and enjoy better popularity. Nevertheless, their applications reported in the literature did not provide much evidence of their applicability for real marine applications, compared with those of the single-phase free-surface LB models. It seems that, in the viewpoint of the author, the single-phase free-surface LB models are more fit for the present study. The free-surface model adopted in this thesis would be the VOF-based single-phase model proposed by Körner et al. [94].

## 1.5.2 Which stabilization technique to be adopted?

Among all the free-surface LBM applications mentioned in this introduction, some have already adopted the stabilization techniques aforementioned in Section 1.3.2. To give an example, one can find the use of the TRT-LBM [14, 17, 15], the MRT-LBM [84], the ELBM [78] and the cascaded LBM [126], for free-surface simulations in the literature. However, the study of the implementation of the RLBM for stable calculation of free-surface flows at high Reynolds numbers is rarely seen, which is quite a pity since the RLBM is a successful and simple variation of the LBM, with a sound mathematical backup. In fact, the present work is targeting at the

numerical validation of the combination of the free-surface LBM for large-density-ratio free-surface flows and the RLBM for high-Reynolds number conditions.

### 1.5.3 Open-source software or in-house code?

It is a primary and painful question for many CFD researchers. Indeed, both options have obvious advantages and disadvantages. An open-source software is usually well coded in a way that many existing models are already embedded, but its documentation is sometimes very complex in order to achieve a maximum applicability for all kinds of problems. In this context, an open-source software requires much time for learning and getting familiar with the coding logic. On the contrary, by developing an in-house code, one can take full charge of every command, however the overall efficiency and applicability of the code may not be as good as the open-source software.

In the early stage of this thesis work, the author spent a lot of time in learning how to use the PALABOS <sup>(i)</sup> open-source LBM code. Like other open-source software, PALABOS is equipped with numerous embedded modules for things like discretizing complex geometries, boundary treatments, extracting data into files, animation making, etc. However, its huge framework is a barrier to the author from fully understanding the code and freely manipulating the implemented models. After several months, it appeared that the learning cost largely overshadowed the benefits of adopting PALABOS, hence a decision was made to develop an in-house LBM code, without trying other open-source LBM codes like OpenLB <sup>(ii)</sup> or waLBerla <sup>(iii)</sup>. The attempts that were made with PALABOS are illustrated in Appendix C.

## 1.6 Outline of the thesis

The thesis is organized as follows.

In Chapter 2, the necessary ingredients of the standard LBM are elaborately presented, which are: the basic equation, the lattice arrangements, the force models and the boundary conditions, as well as the dimensionless formulation. Particularly, the basic equation is illustrated step by step from the CBE all the way to the LBE, including the derivation of the discrete LB equation from the CBE, the derivation of the LBE from the discrete LB equation under the single-relaxation-time collision operator, and the strict mathematical proof of the recovery of the N-S equation from the LBE through a multi-scale analysis.

---

<sup>(i)</sup><http://www.palabos.org>

<sup>(ii)</sup><https://www.openlb.net>

<sup>(iii)</sup><http://walberla.net>

Chapter 3 is focused on the regularized LBM. Based on the Hermite representation of the LBE, the core idea of the RLBM is clarified as a Hermite regularization of the distribution function. Specifically, it is highlighted that the adopted force model requires a correction in the regularization formula, which is validated in a Poiseuille flow test-case. Then, two more test-cases are simulated. The first one is the Taylor-Green vortex flow, for which a convergence and efficiency study is carried out. The other is the lid-driven cavity flow, on which the RLBM is compared with other LBM schemes, in terms of accuracy, CPU time and ability of stabilizing the LB solution.

In Chapter 4, the adopted free-surface model is introduced comprehensively, including the VOF-based representation, the cell mass evolution, the cell flag update and the free-surface treatment. The present free-surface LBM is validated through two test-cases, which are the viscous standing wave and the dambreak flow. Afterwards, by observing that the original free-surface model might be caught in a dilemma about how many distribution functions should be reconstructed, a new technique is proposed for determining the distribution functions at the interface. A dambreak test-case is used for the validation of the new model.

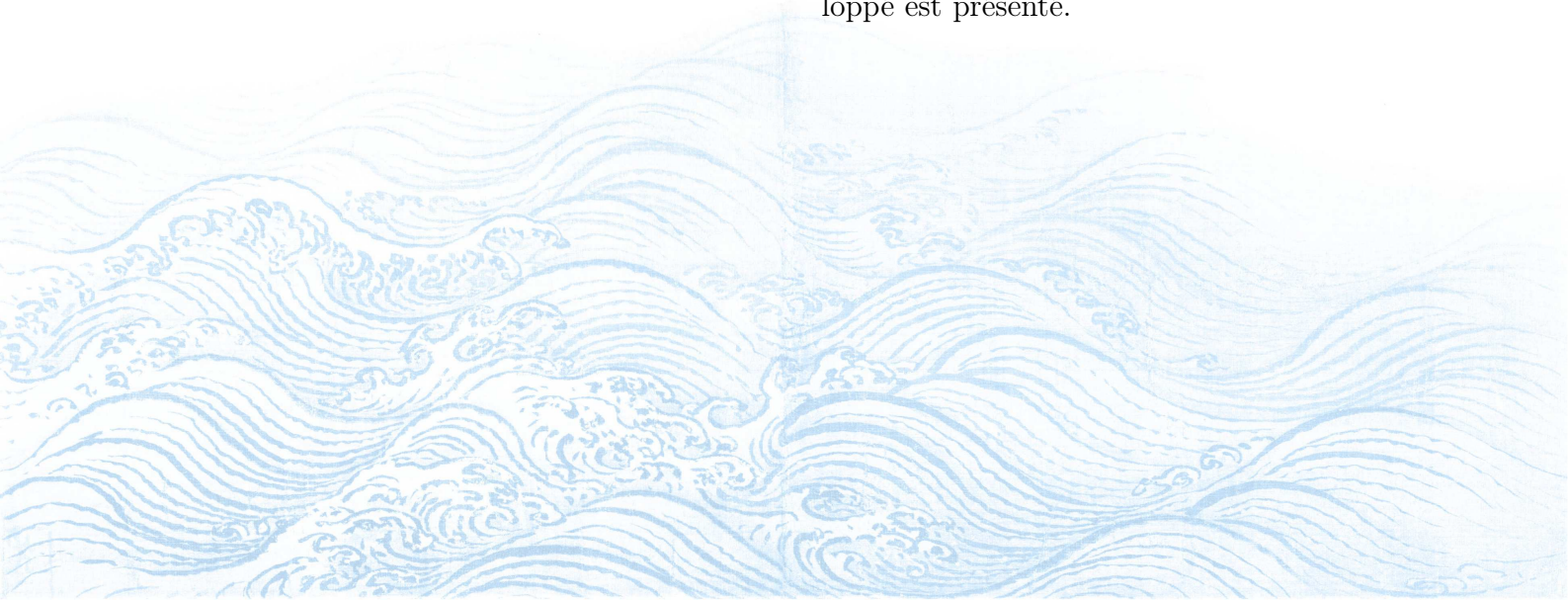
Finally the conclusions and perspectives are drawn in Chapter 5.

# Chapter 2

## Lattice Boltzmann method

The theory of lattice Boltzmann (LB) method is presented in this chapter. In the first part, the derivation of the lattice Boltzmann equation (LBE) from the continuous Boltzmann equation is elaborately presented by means of the Hermite expansion. In the meantime, the force models and the lattice arrangements are discussed. Then, through a multi-scale analysis, the LBE is validated to recover the weakly compressible Navier-Stokes equation. Next, the boundary conditions adopted in this thesis are illustrated. Finally, the rescaling factors for non-dimensionalizing the LBE are introduced, and the present LB algorithm is given.

La théorie de la méthode de Boltzmann sur réseau (LB) est présentée dans ce chapitre. La première partie présente la dérivation de l'équation de Boltzmann sur réseau (LBE) à partir de l'équation de Boltzmann continue, à l'aide du développement d'Hermite. Au passage, les modèles de force et les configurations du réseau sont discutés. Ensuite, on valide par une analyse multi-échelles que l'équation de Navier-Stokes faiblement compressible peut être obtenue à partir de la LBE. Puis, les conditions limites utilisées dans cette thèse sont illustrées. Enfin, les facteurs pour l'adimensionnalisation de la LBE sont introduits, et l'algorithme de LB développé est présenté.



## Contents

---

<b>2.1 Boltzmann description of fluid flow . . . . .</b>	<b>21</b>
2.1.1 Descriptions of fluid flow . . . . .	21
2.1.2 Continuous Boltzmann equation . . . . .	22
2.1.3 Single-relaxation-time collision model . . . . .	24
<b>2.2 From the continuous Boltzmann equation to the lattice Boltzmann equation . . . . .</b>	<b>24</b>
2.2.1 Hermite expansion of the distribution function . . . . .	25
2.2.2 Discretizing the velocity space . . . . .	26
2.2.3 Lattice Boltzmann equation . . . . .	30
<b>2.3 Lattice arrangement . . . . .</b>	<b>33</b>
<b>2.4 Force model . . . . .</b>	<b>35</b>
<b>2.5 Multi-scale analysis . . . . .</b>	<b>37</b>
2.5.1 Starting from the lattice Boltzmann equation . . . . .	37
2.5.2 Adopting Taylor expansion and multi-scale expansion . . . . .	38
2.5.3 Velocity moments of associated ingredients . . . . .	41
2.5.4 Velocity moment of $\mathcal{O}(\varepsilon^1)$ and $\mathcal{O}(\varepsilon^2)$ terms . . . . .	42
2.5.5 Specifying $\mathbf{\Pi}^{(1)}$ . . . . .	43
2.5.6 Recovering the Navier-Stokes equation . . . . .	45
<b>2.6 Boundary conditions . . . . .</b>	<b>47</b>
2.6.1 Bounce back boundary condition . . . . .	47
2.6.2 Specular boundary condition . . . . .	48
2.6.3 Zou-He boundary condition . . . . .	49
2.6.4 Periodic boundary condition . . . . .	50
2.6.5 Free-surface boundary condition . . . . .	51
<b>2.7 Rescaling factors . . . . .</b>	<b>51</b>
<b>2.8 Algorithm . . . . .</b>	<b>52</b>

---

## 2.1 Boltzmann description of fluid flow

### 2.1.1 Descriptions of fluid flow

The fluid mechanics is a branch of physical science developed to analyze the problems that involve fluid flows. In this discipline, a variety of ways to observe the fluid can be found throughout the spectrum of scales, i.e., from the macroscopic scale all the way down to the microscopic scale. Specifically, in the macroscopic scale, the state of a fluid can be described by several variables, such as the fluid density  $\rho$ , the flow velocity  $\mathbf{u}$ , the pressure  $p$ , the internal energy  $E$  and the temperature  $\Theta$ , etc. These variables are all defined in a continuum level, which means that their quantities are considered to be varying continuously in space and time. Meanwhile, their values at one point show the statistic properties of the numerous fluid molecules inside the small volume represented by the point, while the particulate nature of the molecule motions are neglected. For the isothermal problems that are commonly studied in marine engineering, the internal energy and temperature are not variables of interest. Hence the governing equation that only involves the rest of the variables is adequate for marine hydrodynamic problems. Such governing equation, which is known as the Navier-Stokes (N-S) equation, can be obtained from the conservation laws of mass and momentum as

$$\frac{\partial \rho}{\partial t} + \nabla \cdot (\rho \mathbf{u}) = 0, \quad (2.1)$$

$$\begin{aligned} \frac{\partial (\rho \mathbf{u})}{\partial t} + \nabla \cdot (\rho \mathbf{u} \mathbf{u}) = & -\nabla \cdot (p \mathbf{I}) + \nabla \cdot \left\{ \mu \left[ \nabla \mathbf{u} + (\nabla \mathbf{u})^T \right] \right\} \\ & + \nabla \cdot [\zeta (\nabla \cdot \mathbf{u}) \mathbf{I}] + \mathbf{F}, \end{aligned} \quad (2.2)$$

where  $\mu$  and  $\zeta$  respectively stand for the dynamic shear viscosity and the bulk viscosity,  $\mathbf{I}$  is the identity tensor, and  $\mathbf{F} = \rho \mathbf{g}$  is the external body force with  $\mathbf{g}$  being the acceleration. It is worth noticing that Equations (2.1) and (2.2) are written in a compressible form for Newtonian fluids. In that case, an equation of state is needed to relate pressure  $p$  and density  $\rho$  and thus close the system. As for incompressible fluids, the density is a constant value in space and time, i.e.  $\rho \equiv \rho_0$ , therefore the mass conservation equation becomes

$$\nabla \cdot \mathbf{u} = 0. \quad (2.3)$$

With the simplified mass conservation equation (2.3), the viscous term associated with the bulk viscosity in the momentum conservation equation (2.2) automati-

cally disappears, which gives

$$\frac{\partial \mathbf{u}}{\partial t} + \nabla \cdot (\mathbf{u}\mathbf{u}) = -\frac{1}{\rho} \nabla \cdot (p\mathbf{I}) + \nabla \cdot \left\{ \nu \left[ \nabla \mathbf{u} + (\nabla \mathbf{u})^T \right] \right\} + \mathbf{F}, \quad (2.4)$$

where  $\nu = \mu/\rho$  is the kinetic viscosity. Equation (2.3) and (2.4) are called the incompressible N-S equations. No matter the compressible form or the incompressible form, the N-S equations give the dynamic relations between the macroscopic variables, and the task of the computational fluid dynamics (CFD) is to find numerically the approximate solution of the N-S equation using appropriate numerical methods.

Alternatively, the fluid motion can be studied in a different way. Since the physicists in molecular dynamics (MD) revealed an inner world by observing the basic construction of all materials, it is now known to us that every macroscopic property has a microscopic nature. From a microscopic point of view, a fluid consists of numerous, randomly moving molecules. Despite the fact that the motion of each molecule is irregular, a huge amount of molecules exhibit some common macroscopic features. Thus it is theoretically possible to compute the macroscopic variables by tracking every molecule's behavior and through some statistical methods. Although the capacity of computer calculation has witnessed a mind-blowing breakthrough thanks to the quick development of the computer science, it is still unrealistic to use full MD simulations to study flows at micro-scales because of memory and computational time limitations [136].

As a substitute, the lattice Boltzmann method (LBM), which can be regarded as a mesoscopic method, lies between the macroscopic and microscopic methodology. It describes the fluid by defining a distribution function  $f(\mathbf{x}, \boldsymbol{\xi}, t)$ , which represents the proportion of the molecules having a microscopic velocity of  $\boldsymbol{\xi}$  at position  $\mathbf{x}$  and time  $t$ . This mesoscopic concept has both macroscopic and microscopic characteristics. Firstly, the macroscopic variables can be computed from the velocity moments of the distribution functions. Secondly, the distribution function has particulate behaviors, i.e. collision and streaming. In the following sections, the governing equation of the distribution function behavior which is known as the Boltzmann equation, as well as the recovery of the N-S equations from the lattice Boltzmann equation, will be elaborately discussed.

### 2.1.2 Continuous Boltzmann equation

As aforementioned in the previous section, the distribution function  $f(\mathbf{x}, \boldsymbol{\xi}, t)$  is a mesoscopic concept, which indicates the probability that the molecules move with

a velocity  $\boldsymbol{\xi}$  at  $(\boldsymbol{x}, t)$ . This definition may sound a little tortuous and complex, but the relation between the distribution function and the macroscopic variables is clear and straightforward, and it helps to better understand the definition of the distribution function. Taking the fluid density as an example, the total number of the molecules of any speed at  $(\boldsymbol{x}, t)$  can be computed from the integral of the distribution function with respect to  $\boldsymbol{\xi}$  as  $\int f(\boldsymbol{x}, \boldsymbol{\xi}, t) d\boldsymbol{\xi}$ . Assuming the molecule weight is  $m$ , the fluid density at  $(\boldsymbol{x}, t)$  can be expressed as

$$\rho(\boldsymbol{x}, t) = m \int f(\boldsymbol{x}, \boldsymbol{\xi}, t) d\boldsymbol{\xi}. \quad (2.5)$$

Similarly, the momentum and the internal energy can be respectively computed from the velocity moments of the first several orders as

$$\rho \boldsymbol{u}(\boldsymbol{x}, t) = m \int \boldsymbol{\xi} f(\boldsymbol{x}, \boldsymbol{\xi}, t) d\boldsymbol{\xi}, \quad (2.6)$$

$$\rho E(\boldsymbol{x}, t) = m \int \frac{1}{2} (\boldsymbol{\xi} - \boldsymbol{u})^2 f(\boldsymbol{x}, \boldsymbol{\xi}, t) d\boldsymbol{\xi}, \quad (2.7)$$

where  $\boldsymbol{u}$  is the fluid velocity, and  $E$  is the internal energy. The molecule mass  $m$  is hereafter assumed to be unit for simplicity.

Based on the definition of the distribution function, the streaming process can be expressed as

$$f(\boldsymbol{x} + \boldsymbol{\xi}\Delta t, \boldsymbol{\xi} + \Delta\boldsymbol{\xi}, t + \Delta t) = f(\boldsymbol{x}, \boldsymbol{\xi}, t). \quad (2.8)$$

It means that the molecules of a speed  $\boldsymbol{\xi}$  at  $(\boldsymbol{x}, t)$  will move to  $(\boldsymbol{x} + \boldsymbol{\xi}\Delta t, t + \Delta t)$  during a small time period  $\Delta t$ , with  $\frac{\Delta\boldsymbol{\xi}}{\Delta t} = \frac{\boldsymbol{F}}{m} = \boldsymbol{g}$  being the acceleration due to the external force  $\boldsymbol{F}$ . This equation describes a pure streaming process, without considering the collisions between molecules. Notice that the collision process is so complex that it is difficult to find a simple mathematical expression for it. Here a general form of the collision operator, i.e.  $\Omega$ , is used, which denotes the changing rate of the distribution function during a collision process as

$$f(\boldsymbol{x} + \boldsymbol{\xi}\Delta t, \boldsymbol{\xi} + \Delta\boldsymbol{\xi}, t + \Delta t) - f(\boldsymbol{x}, \boldsymbol{\xi}, t) = \Omega\Delta t. \quad (2.9)$$

Taking the limit where  $\Delta t \rightarrow 0$  and  $\Delta\boldsymbol{\xi} \rightarrow 0$  yields:

$$\frac{\partial f}{\partial t} + \boldsymbol{\xi} \cdot \nabla f + \boldsymbol{g} \cdot \nabla_{\boldsymbol{\xi}} f = \Omega, \quad (2.10)$$

where the gradient operator  $\nabla$  denotes the space gradient, and  $\nabla_{\boldsymbol{\xi}}$  denotes the gradient in the velocity space. Equation (2.10) is known as the continuous Boltzmann equation (CBE).

### 2.1.3 Single-relaxation-time collision model

One can observe that the collision operator  $\Omega$  plays a vital and fundamental role in the Boltzmann equation (2.10). However its expression is still undefined for the moment due to the very different possibilities of particle collisions. Therefore the major barrier in solving the Boltzmann equation is the difficulty of addressing a proper approximation of the collision operator. In 1954, an efficient and widely used single-relaxation-time (SRT) model is introduced by Bhatnagar, Gross and Krook (BGK) [12]. In their model, the collision operator  $\Omega$  is replaced by a relaxation process from a distribution state slightly off-set from its equilibrium as

$$\Omega = -\frac{1}{\tau\Delta t} (f - f^{\text{eq}}), \quad (2.11)$$

where  $\tau$  is the dimensionless relaxation time and  $f^{\text{eq}}$  is the so-called equilibrium distribution function.  $f^{\text{eq}}$  is chosen to be the continuous Maxwell-Boltzmann distribution function, which is expressed as

$$f^{\text{eq}} = \frac{\rho}{(2\pi R\Theta)^{\dim/2}} \exp\left[-\frac{(\boldsymbol{\xi} - \mathbf{u})^2}{2R\Theta}\right], \quad (2.12)$$

where  $\dim$  is the spatial dimension,  $\mathbf{u}$  is the macroscopic fluid velocity,  $R$  is the gas constant, and  $\Theta$  is the temperature.

The Boltzmann equation with the SRT collision model reads

$$\frac{\partial f}{\partial t} + \boldsymbol{\xi} \cdot \nabla f + \mathbf{g} \cdot \nabla_{\boldsymbol{\xi}} f = -\frac{1}{\tau\Delta t} (f - f^{\text{eq}}), \quad (2.13)$$

which gives the simplest and the most widely used governing equation of the distribution function, up to now. For this reason, the author will hereafter refer to Equation (2.13) when mentioning the *standard* Boltzmann equation.

## 2.2 From the continuous Boltzmann equation to the lattice Boltzmann equation

The N-S equations have been successfully recovered from the standard CBE (2.13) in [76], hence Equation (2.13) can be assessed as an elegant description of fluid flow considering its simplicity and effectiveness. However, the molecule velocity  $\boldsymbol{\xi}$  in the distribution function  $f(\mathbf{x}, \boldsymbol{\xi}, t)$  represents infinite degrees of freedom since it can be of an arbitrary value in the continuous velocity space, while the computer calculation can only handle a finite number of variables. Therefore, an appropriate discretization of the CBE is desired in a way that it is numerically solvable without

damaging the recovery of the N-S equation. In this context, the lattice Boltzmann equation (LBE) is developed following such an idea. To give a direct impression, the LBE is presented here as

$$f_i(\mathbf{x} + \boldsymbol{\xi}_i \Delta t, t + \Delta t) - f_i(\mathbf{x}, t) = -\frac{1}{\tau} [f_i(\mathbf{x}, t) - f_i^{\text{eq}}(\mathbf{x}, t)] + \Delta t F_i(\mathbf{x}, t), \quad (2.14)$$

where  $\mathbf{x}$  denotes the coordinate of a point in the discretized space (the lattice), and  $\{\boldsymbol{\xi}_i\}$  represents a set of discretized microscopic velocities associated with the chosen lattice where  $(i = 0, 1, \dots, q - 1)$  indicates one of the  $q$  possible directions of the lattice velocity  $\boldsymbol{\xi}_i$ . Correspondingly,  $f_i(\mathbf{x}, t)$  is the distribution function of the fluid particles with a lattice velocity  $\boldsymbol{\xi}_i$  at position  $(\mathbf{x}, t)$ , and  $f_i^{\text{eq}}(\mathbf{x}, t)$  is its equilibrium.  $\Delta t$  is the time increment within one time step. The derivation of Equation (2.14) from the CBE (2.13) will be analyzed step by step in this section.

### 2.2.1 Hermite expansion of the distribution function

Before starting, it is important to note that from Equation (2.15) to (2.48), the following analysis is based on a dimensionless form of the continuous Boltzmann equation (2.13), namely the microscopic velocity  $\tilde{\boldsymbol{\xi}}$  and the fluid velocity  $\tilde{\mathbf{u}}$  are dimensionless variables scaled by the sound speed  $c_s$ , and the temperature  $\Theta$  is replaced by the dimensionless temperature  $\tilde{\Theta}$ .

As just stated, the LBE uses a minimized number of discretized velocities to provide as many macroscopic details as the CBE. This is done with the help of the Hermite polynomials and the Gauss-Hermite quadrature, and some necessary mathematical support is given in Appendix A.4.

Starting from the CBE (2.13), the distribution function  $f(\mathbf{x}, \tilde{\boldsymbol{\xi}}, t)$  is chosen to be expanded by the Hermite polynomials as

$$f(\mathbf{x}, \tilde{\boldsymbol{\xi}}, t) = \omega(\tilde{\boldsymbol{\xi}}) \sum_{n=0}^{\infty} \frac{1}{n!} \mathbf{a}^{(n)}(\mathbf{x}, t) : \mathcal{H}^{(n)}(\tilde{\boldsymbol{\xi}}), \quad (2.15)$$

where  $\omega(\tilde{\boldsymbol{\xi}})$  is the weighting function,  $\mathcal{H}^{(n)}(\tilde{\boldsymbol{\xi}})$  is the  $n^{\text{th}}$ -order Hermite polynomial, and  $\mathbf{a}^{(n)}(\mathbf{x}, t)$  is the corresponding expansion coefficient.

The weighting function  $\omega(\tilde{\boldsymbol{\xi}})$  is given as

$$\omega(\tilde{\boldsymbol{\xi}}) = \frac{1}{(2\pi)^{\dim/2}} \exp\left(-\frac{\tilde{\boldsymbol{\xi}} \cdot \tilde{\boldsymbol{\xi}}}{2}\right), \quad (2.16)$$

and the  $n^{\text{th}}$ -order Hermite polynomial can be calculated from  $\omega(\tilde{\boldsymbol{\xi}})$  as

$$\mathcal{H}^{(n)}(\tilde{\boldsymbol{\xi}}) = \frac{(-1)^n}{\omega(\tilde{\boldsymbol{\xi}})} \nabla_{\tilde{\boldsymbol{\xi}}}^n \omega(\tilde{\boldsymbol{\xi}}). \quad (2.17)$$

The corresponding expansion coefficient  $\mathbf{a}^{(n)}(\mathbf{x}, t)$  is computed from

$$\mathbf{a}^{(n)}(\mathbf{x}, t) = \int f(\mathbf{x}, \tilde{\boldsymbol{\xi}}, t) \mathcal{H}^{(n)}(\tilde{\boldsymbol{\xi}}) d\tilde{\boldsymbol{\xi}}. \quad (2.18)$$

More specifically, the first several Hermite polynomials can be obtained from Equation (2.17) as

$$\begin{cases} \mathcal{H}^{(0)}(\tilde{\boldsymbol{\xi}}) = 1, \\ \mathcal{H}^{(1)}(\tilde{\boldsymbol{\xi}}) = \tilde{\boldsymbol{\xi}}, \\ \mathcal{H}^{(2)}(\tilde{\boldsymbol{\xi}}) = \tilde{\boldsymbol{\xi}}\tilde{\boldsymbol{\xi}} - I, \end{cases} \quad (2.19)$$

and the first several expansion coefficients are

$$\begin{cases} \mathbf{a}^{(0)}(\mathbf{x}, t) = \rho(\mathbf{x}, t) \\ \mathbf{a}^{(1)}(\mathbf{x}, t) = \rho(\mathbf{x}, t) \tilde{\mathbf{u}}(\mathbf{x}, t). \end{cases} \quad (2.20)$$

One can observe that the expansion coefficient at the leading orders are the moments of the distribution function in the velocity space, which correspond to the macroscopic variables. Such observation is vital in this analysis, and it is the reason of applying the Hermite expansion to the distribution function. The readers are suggested to keep this observation in mind, and it will be mentioned again in the following analysis.

## 2.2.2 Discretizing the velocity space

Equation (2.15) indicates that the distribution function can be identically computed through the summation of an infinite number of terms which correspond to the Hermite polynomials. However, the distribution function contains more information than just the hydrodynamics of fluid flows, because what matter in the N-S equations are only the first several velocity moments of the distribution function. Hence, it would be more convenient if less information can be included in the calculation while keeping the first several velocity moments unaffected. Fortunately, the Hermite polynomials provide a possible solution. Consider a truncated

Hermite expansion to the  $N^{\text{th}}$ -order, which is marked as

$$f^N(\mathbf{x}, \tilde{\boldsymbol{\xi}}, t) = \omega(\tilde{\boldsymbol{\xi}}) \sum_{n=0}^N \frac{1}{n!} \mathbf{a}_N^{(n)}(\mathbf{x}, t) : \mathcal{H}^{(n)}(\tilde{\boldsymbol{\xi}}), \quad (2.21)$$

the first  $N$  expansion coefficients of the truncated expansion  $f^N(\mathbf{x}, \tilde{\boldsymbol{\xi}}, t)$  are exactly the same as those for the full expansion of  $f(\mathbf{x}, \tilde{\boldsymbol{\xi}}, t)$ , thanks to the mutual orthogonality of the Hermite polynomials as expressed in Equation (A.13). The leading expansion coefficients are thus the same as before, i.e. the leading velocity moments, as formerly pointed out in the previous section. Therefore the truncation of the higher order terms does not affect the leading velocity moments.

To achieve one step further, another feature of the Hermite polynomials is used. As being pointed out in [158], the integrand in Equation (2.18) for calculating the expansion coefficient of the truncated expansion  $f^N(\mathbf{x}, \tilde{\boldsymbol{\xi}}, t)$  can be written as

$$f^N(\mathbf{x}, \tilde{\boldsymbol{\xi}}, t) \mathcal{H}^{(n)}(\tilde{\boldsymbol{\xi}}) = \omega(\tilde{\boldsymbol{\xi}}) \Psi(\mathbf{x}, \tilde{\boldsymbol{\xi}}, t), \quad (2.22)$$

where  $\Psi(\mathbf{x}, \tilde{\boldsymbol{\xi}}, t)$  is a polynomial in  $\tilde{\boldsymbol{\xi}}$  of a degree not greater than  $2N$ . Hence the expansion coefficient  $\mathbf{a}_N^{(n)}$  for  $f^N(\mathbf{x}, \tilde{\boldsymbol{\xi}}, t)$  is computed as

$$\mathbf{a}_N^{(n)} = \int f^N(\mathbf{x}, \tilde{\boldsymbol{\xi}}, t) \mathcal{H}^{(n)}(\tilde{\boldsymbol{\xi}}) d\tilde{\boldsymbol{\xi}} = \int \omega(\tilde{\boldsymbol{\xi}}) \Psi(\mathbf{x}, \tilde{\boldsymbol{\xi}}, t) d\tilde{\boldsymbol{\xi}}. \quad (2.23)$$

Note that the form of  $\Psi(\mathbf{x}, \tilde{\boldsymbol{\xi}}, t)$  is not important here, and it is obvious that the integral on the right-hand side matches the form of the Gauss-Hermite quadrature in Equation (A.7). Thus the expansion coefficient becomes

$$\begin{aligned} \mathbf{a}_N^{(n)} &= \int \omega(\tilde{\boldsymbol{\xi}}) \Psi(\mathbf{x}, \tilde{\boldsymbol{\xi}}, t) d\tilde{\boldsymbol{\xi}} = \sum_{i=1}^q w_i \Psi(\mathbf{x}, \tilde{\boldsymbol{\xi}}_i, t) \\ &= \sum_{i=1}^q \frac{w_i}{\omega(\tilde{\boldsymbol{\xi}}_i)} f^N(\mathbf{x}, \tilde{\boldsymbol{\xi}}_i, t) \mathcal{H}^{(n)}(\tilde{\boldsymbol{\xi}}_i), \end{aligned} \quad (2.24)$$

where  $w_i$  and  $\tilde{\boldsymbol{\xi}}_i$  are respectively the weights and the abscissae of a Gauss-Hermite quadrature, and  $q$  is the number of the chosen discretized velocities  $\tilde{\boldsymbol{\xi}}_i$ . Now, the expansion coefficients of the truncated expansion  $f^N(\mathbf{x}, \tilde{\boldsymbol{\xi}}, t)$  are accurately determined by a set of distribution functions with discrete velocities  $f^N(\mathbf{x}, \tilde{\boldsymbol{\xi}}_i, t)$ . As a result, the truncated expansion  $f^N(\mathbf{x}, \tilde{\boldsymbol{\xi}}, t)$  is also determined by the distribution functions of discrete velocities, through Equation (2.21).

The task of developing the LBE becomes seeking a governing equation of

$f^N(\mathbf{x}, \tilde{\boldsymbol{\xi}}_i, t)$  that contains the same level of hydrodynamic information as the original CBE (2.13). This is done by enforcing the same truncated Hermite expansion, as presented in this section, to every term in the CBE (2.13). Such operations on the equilibrium distribution function and the force term will be shown in the following paragraphs.

**Equilibrium distribution function** The equilibrium distribution function in the form of Equation (2.12) is to be substituted by its truncated Hermite expansion  $f_N^{\text{eq}}(\mathbf{x}, \tilde{\boldsymbol{\xi}}, t)$  as

$$f_N^{\text{eq}}(\mathbf{x}, \tilde{\boldsymbol{\xi}}, t) = \omega(\tilde{\boldsymbol{\xi}}) \sum_{n=0}^N \frac{1}{n!} \mathbf{a}_{N,\text{eq}}^{(n)}(\mathbf{x}, t) : \mathcal{H}^{(n)}(\tilde{\boldsymbol{\xi}}), \quad (2.25)$$

where the expansion coefficient  $\mathbf{a}_{N,\text{eq}}^{(n)}(\mathbf{x}, t)$  of leading orders are identical with those of  $f^{\text{eq}}(\mathbf{x}, \tilde{\boldsymbol{\xi}}, t)$  as

$$\mathbf{a}_{\text{eq}}^{(n)}(\mathbf{x}, t) = \int f^{\text{eq}}(\mathbf{x}, \tilde{\boldsymbol{\xi}}, t) \mathcal{H}^{(n)}(\tilde{\boldsymbol{\xi}}) d\tilde{\boldsymbol{\xi}}. \quad (2.26)$$

In order to calculate the first several expansion coefficients, the equilibrium distribution function is firstly written as

$$f^{\text{eq}}(\mathbf{x}, t) = \frac{\rho(\mathbf{x}, t)}{(\sqrt{\tilde{\Theta}})^{\text{dim}}} \omega\left(\frac{\tilde{\boldsymbol{\xi}} - \tilde{\mathbf{u}}(\mathbf{x}, t)}{\sqrt{\tilde{\Theta}}}\right), \quad (2.27)$$

with the help Equation (2.12) and (2.16), where  $\tilde{\Theta}$  is the dimensionless temperature and  $\tilde{\Theta} = 1$  for isothermal systems as in this study. Let  $\tilde{\boldsymbol{\eta}} = \frac{\tilde{\boldsymbol{\xi}} - \tilde{\mathbf{u}}}{\sqrt{\tilde{\Theta}}}$ , then  $\tilde{\boldsymbol{\xi}} = \sqrt{\tilde{\Theta}}\tilde{\boldsymbol{\eta}} + \tilde{\mathbf{u}}$ . Thus one has

$$f^{\text{eq}} = \frac{\rho}{(\sqrt{\tilde{\Theta}})^{\text{dim}}} \omega(\tilde{\boldsymbol{\eta}}) \quad (2.28)$$

and

$$\mathbf{a}_{\text{eq}}^{(n)} = \rho \int \frac{\omega(\tilde{\boldsymbol{\eta}})}{(\sqrt{\tilde{\Theta}})^{\text{dim}-1}} \mathcal{H}^{(n)}(\sqrt{\tilde{\Theta}}\tilde{\boldsymbol{\eta}} + \tilde{\mathbf{u}}) d\tilde{\boldsymbol{\eta}}. \quad (2.29)$$

In an isothermal system where  $\tilde{\Theta} = 1$ , the first several expansion coefficients can

be easily computed as

$$\begin{cases} \mathbf{a}_{N,\text{eq}}^{(0)} = \mathbf{a}_{\text{eq}}^{(0)} = \rho, \\ \mathbf{a}_{N,\text{eq}}^{(1)} = \mathbf{a}_{\text{eq}}^{(1)} = \rho \tilde{\mathbf{u}} \\ \mathbf{a}_{N,\text{eq}}^{(2)} = \mathbf{a}_{\text{eq}}^{(2)} = \rho \tilde{\mathbf{u}} \tilde{\mathbf{u}}. \end{cases} \quad (2.30)$$

Hence  $f_N^{\text{eq}}$  can be obtained from Equation (2.25) as

$$\begin{aligned} f_N^{\text{eq}} &= \omega(\tilde{\boldsymbol{\xi}}) \left[ \underbrace{\overbrace{\rho}^{0^{\text{th}}\text{-order}} + \overbrace{\rho \tilde{\mathbf{u}} \cdot \tilde{\boldsymbol{\xi}}}^{1^{\text{st}}\text{-order}} + \overbrace{\frac{1}{2} \rho \tilde{\mathbf{u}} \tilde{\mathbf{u}} : (\tilde{\boldsymbol{\xi}} \tilde{\boldsymbol{\xi}} - \mathbf{I})}^{2^{\text{nd}}\text{-order}}}_{(N+1) \text{ terms}} + \dots \right] \\ &= \omega(\tilde{\boldsymbol{\xi}}) \left\{ \underbrace{\overbrace{\rho}^{0^{\text{th}}\text{-order}} + \overbrace{\rho \tilde{\mathbf{u}} \cdot \tilde{\boldsymbol{\xi}}}^{1^{\text{st}}\text{-order}} + \left[ \frac{1}{2} \rho (\tilde{\mathbf{u}} \cdot \tilde{\boldsymbol{\xi}})^2 - \frac{1}{2} \rho \tilde{\mathbf{u}}^2 \right]}^{2^{\text{nd}}\text{-order}}}_{(N+1) \text{ terms}} + \dots \right\}. \end{aligned} \quad (2.31)$$

Note that the three terms listed in the braces above are respectively the 0<sup>th</sup>-, 1<sup>st</sup>-, and 2<sup>nd</sup>-order terms.

**Force term** Adopting the Hermite expansion (2.15), the gradient of the distribution function in the velocity space, i.e.  $\nabla_{\tilde{\boldsymbol{\xi}}} f(\mathbf{x}, \tilde{\boldsymbol{\xi}}, t)$  in the CBE (2.13), can be written as

$$\nabla_{\tilde{\boldsymbol{\xi}}} f(\mathbf{x}, \tilde{\boldsymbol{\xi}}, t) = \nabla_{\tilde{\boldsymbol{\xi}}} \left[ \omega(\tilde{\boldsymbol{\xi}}) \sum_{n=0}^{\infty} \frac{1}{n!} \mathbf{a}^{(n)}(\mathbf{x}, t) : \mathcal{H}^{(n)}(\tilde{\boldsymbol{\xi}}) \right]. \quad (2.32)$$

By inserting the gradient operator and the weighting function  $\omega(\tilde{\boldsymbol{\xi}})$  into the summation and using Equation (2.18) repeatedly,  $\nabla_{\tilde{\boldsymbol{\xi}}} f(\mathbf{x}, \tilde{\boldsymbol{\xi}}, t)$  can be expressed as

$$\begin{aligned} \nabla_{\tilde{\boldsymbol{\xi}}} f &= \sum_{n=0}^{\infty} \frac{1}{n!} \mathbf{a}^{(n)} \nabla_{\tilde{\boldsymbol{\xi}}} \left[ \omega(\tilde{\boldsymbol{\xi}}) \mathcal{H}^{(n)}(\tilde{\boldsymbol{\xi}}) \right] = \sum_{n=0}^{\infty} \frac{(-1)^n}{n!} \mathbf{a}^{(n)} \nabla_{\tilde{\boldsymbol{\xi}}}^{n+1} \omega(\tilde{\boldsymbol{\xi}}) \\ &= -\omega(\tilde{\boldsymbol{\xi}}) \sum_{n=0}^{\infty} \frac{1}{n!} \mathbf{a}^{(n)} \mathcal{H}^{(n+1)}(\tilde{\boldsymbol{\xi}}), \end{aligned} \quad (2.33)$$

where the products of two tensors of different orders means the sum of all possible permutations of tensor product [158].

Let the force term in the CBE (2.13) take the form of

$$\mathbf{F}(\mathbf{x}, \tilde{\boldsymbol{\xi}}, t) = -\mathbf{g}(\mathbf{x}, t) \cdot \nabla_{\tilde{\boldsymbol{\xi}}} f(\mathbf{x}, \tilde{\boldsymbol{\xi}}, t) = -\frac{\mathbf{g}(\mathbf{x}, t)}{c_s} \cdot \nabla_{\tilde{\boldsymbol{\xi}}} f(\mathbf{x}, \tilde{\boldsymbol{\xi}}, t) \quad (2.34)$$

which shall appear on the right-hand side in (2.13). Then, one has

$$\mathbf{F}(\mathbf{x}, \tilde{\boldsymbol{\xi}}, t) = \omega(\tilde{\boldsymbol{\xi}}) \sum_{n=0}^{\infty} \frac{1}{n!} \frac{\mathbf{g}(\mathbf{x}, t)}{c_s} \left[ \mathbf{a}^{(n)}(\mathbf{x}, t) \mathcal{H}^{(n+1)}(\tilde{\boldsymbol{\xi}}) \right] \quad (2.35)$$

by introducing the expression (2.33). Being substituted by a truncated Hermite expansion, the force term becomes

$$\mathbf{F}^N(\mathbf{x}, \tilde{\boldsymbol{\xi}}, t) = \omega(\tilde{\boldsymbol{\xi}}) \sum_{n=0}^N \frac{1}{n!} \frac{\mathbf{g}(\mathbf{x}, t)}{c_s} \left[ \mathbf{a}^{(n)}(\mathbf{x}, t) \mathcal{H}^{(n+1)}(\tilde{\boldsymbol{\xi}}) \right]. \quad (2.36)$$

The first several expansion coefficients are given as

$$\begin{cases} \mathbf{a}^{(0)}(\mathbf{x}, t) = \rho(\mathbf{x}, t) \\ \mathbf{a}^{(1)}(\mathbf{x}, t) = \rho(\mathbf{x}, t) \tilde{\mathbf{u}}(\mathbf{x}, t). \end{cases} \quad (2.37)$$

Therefore the force term in Equation (2.36) can be computed as

$$\begin{aligned} \mathbf{F}^N &= \frac{\omega(\tilde{\boldsymbol{\xi}})}{c_s} \left[ \underbrace{\rho(\mathbf{g} \cdot \tilde{\boldsymbol{\xi}})}_{\text{1st-order}} + \underbrace{(\rho \mathbf{g} \tilde{\mathbf{u}}) : (\tilde{\boldsymbol{\xi}} \tilde{\boldsymbol{\xi}} - \mathbf{I})}_{\text{2nd-order}} + \dots \right] \\ &= \frac{\omega(\tilde{\boldsymbol{\xi}})}{c_s} \rho \left\{ \underbrace{\mathbf{g} \cdot \tilde{\boldsymbol{\xi}}}_{\text{1st-order}} + \underbrace{\left[ (\mathbf{g} \cdot \tilde{\boldsymbol{\xi}}) (\tilde{\mathbf{u}} \cdot \tilde{\boldsymbol{\xi}}) - \mathbf{g} \cdot \tilde{\mathbf{u}} \right]}_{\text{2nd-order}} + \dots \right\}. \end{aligned} \quad (2.38)$$

Note that the two terms listed in the brace above are respectively the 1<sup>st</sup>- and 2<sup>nd</sup>-order terms.

### 2.2.3 Lattice Boltzmann equation

From the analysis in the previous Section 2.2.2, it is now known that following a truncated Hermite expansion and a Gauss-Hermite quadrature, a set of distribution function with discrete velocities are adequate to accurately compute the hydrodynamic moments of the original distribution function, as expressed in Equation (2.24). More specifically, in the expression (2.24) the first several orders are given as

$$\begin{cases} \rho(\mathbf{x}, t) = \sum_{i=1}^q \frac{w_i f^N(\mathbf{x}, \tilde{\boldsymbol{\xi}}_i, t)}{\omega(\tilde{\boldsymbol{\xi}}_i)}, \\ \rho(\mathbf{x}, t) \tilde{\mathbf{u}}(\mathbf{x}, t) = \sum_{i=1}^q \frac{w_i f^N(\mathbf{x}, \tilde{\boldsymbol{\xi}}_i, t) \tilde{\boldsymbol{\xi}}_i}{\omega(\tilde{\boldsymbol{\xi}}_i)}. \end{cases} \quad (2.39)$$

Defining

$$f_i(\mathbf{x}, t) \equiv \frac{w_i f^N(\mathbf{x}, \tilde{\boldsymbol{\xi}}_i, t)}{\omega(\tilde{\boldsymbol{\xi}}_i)} \quad (2.40)$$

with  $(i = 1, 2, \dots, q)$ , the above equations become

$$\left\{ \begin{array}{l} \rho(\mathbf{x}, t) = \sum_{i=1}^q f_i, \\ \rho(\mathbf{x}, t) \tilde{\mathbf{u}}(\mathbf{x}, t) = \sum_{i=1}^q f_i \tilde{\boldsymbol{\xi}}_i. \end{array} \right. \quad (2.41)$$

Similarly, a discrete equilibrium distribution function and a discrete force term are respectively defined as

$$f_i^{\text{eq}}(\mathbf{x}, t) \equiv \frac{w_i f^{\text{eq}}_N(\mathbf{x}, \tilde{\boldsymbol{\xi}}_i, t)}{\omega(\tilde{\boldsymbol{\xi}}_i)}, \quad (2.42)$$

$$F_i(\mathbf{x}, t) \equiv \frac{w_i F^N(\mathbf{x}, \tilde{\boldsymbol{\xi}}_i, t)}{\omega(\tilde{\boldsymbol{\xi}}_i)}, \quad (2.43)$$

where  $(i = 1, 2, \dots, q)$ . Using Equations (2.31) and (2.38),  $f_i^{\text{eq}}$  and  $F_i$  can be written as

$$f_i^{\text{eq}} = w_i \rho \left[ \underbrace{\overbrace{1}^{0^{\text{th}}\text{-order}} + \overbrace{\tilde{\mathbf{u}} \cdot \tilde{\boldsymbol{\xi}}}^{1^{\text{st}}\text{-order}} + \overbrace{\frac{1}{2}(\tilde{\mathbf{u}} \cdot \tilde{\boldsymbol{\xi}})^2 - \frac{1}{2}\tilde{\mathbf{u}}^2 + \dots}^{2^{\text{nd}}\text{-order}}}_{(N+1) \text{ terms}} \right], \quad (2.44)$$

and

$$F_i = \frac{w_i \rho}{c_s} \left\{ \underbrace{\overbrace{\mathbf{g} \cdot \tilde{\boldsymbol{\xi}}}^{1^{\text{st}}\text{-order}} + \overbrace{\left[ (\mathbf{g} \cdot \tilde{\boldsymbol{\xi}}) (\tilde{\mathbf{u}} \cdot \tilde{\boldsymbol{\xi}}) - \mathbf{g} \cdot \tilde{\mathbf{u}} \right]}^{2^{\text{nd}}\text{-order}}}_{N \text{ terms}} + \dots \right\}. \quad (2.45)$$

Based on the three definitions in Equation (2.40), (2.42) and (2.43), the following Boltzmann equation in a discretized velocity space is obtained, i.e.

$$\frac{\partial f_i}{\partial t} + \tilde{\boldsymbol{\xi}}_i \cdot \nabla f_i = -\frac{1}{\tau \Delta t} (f_i - f_i^{\text{eq}}) + F_i. \quad (2.46)$$

Equation (2.46) can be further discretized in space and time by employing a 1<sup>st</sup>-order up-wind finite-difference approximation of the derivatives on the left-hand side as

$$\frac{\partial f_i}{\partial t} + \tilde{\boldsymbol{\xi}}_i \cdot \nabla f_i \approx \frac{f_i(\mathbf{x} + \tilde{\boldsymbol{\xi}}_i \Delta t, t + \Delta t) - f_i(\mathbf{x}, t)}{\Delta t}. \quad (2.47)$$

Hence the standard LBE is finally obtained as

$$f_i(\mathbf{x} + \tilde{\boldsymbol{\xi}}_i \Delta t, t + \Delta t) - f_i(\mathbf{x}, t) = -\frac{1}{\tau} [f_i(\mathbf{x}, t) - f_i^{\text{eq}}(\mathbf{x}, t)] + \Delta t F_i(\mathbf{x}, t). \quad (2.48)$$

It is very important to remember that in the former part of the analysis in the present Section 2.2, the variables related to the micro- and macroscopic velocities, i.e.  $\tilde{\boldsymbol{\xi}}$ ,  $\tilde{\mathbf{u}}$  and  $\tilde{\boldsymbol{\xi}}_i$ , are all dimensionless variables scaled by the sound speed  $c_s$ . From now on, these variables will be rewritten in a dimensional form as was commonly done in the literature. The standard LBE becomes

$$f_i(\mathbf{x} + \boldsymbol{\xi}_i \Delta t, t + \Delta t) - f_i(\mathbf{x}, t) = -\frac{1}{\tau} [f_i(\mathbf{x}, t) - f_i^{\text{eq}}(\mathbf{x}, t)] + \Delta t F_i(\mathbf{x}, t), \quad (2.49)$$

Usually this equation is separated into two steps, the collision step

$$f_i^{\text{pc}}(\mathbf{x}, t) = f_i(\mathbf{x}, t) - \frac{1}{\tau} [f_i(\mathbf{x}, t) - f_i^{\text{eq}}(\mathbf{x}, t)] + \Delta t F_i(\mathbf{x}, t) \quad (2.50)$$

and the streaming step

$$f_i(\mathbf{x} + \boldsymbol{\xi}_i \Delta t, t + \Delta t) = f_i^{\text{pc}}(\mathbf{x}, t), \quad (2.51)$$

where the superscript " $\square^{\text{pc}}$ " denotes a post-collision term, and  $\boldsymbol{\xi}_i$  is one of the  $q$  lattice speeds. The equilibrium distribution function reads

$$f_i^{\text{eq}} = w_i \rho \left[ 1 + \frac{\boldsymbol{\xi}_i \cdot \mathbf{u}}{c_s^2} + \frac{(\mathbf{u} \cdot \boldsymbol{\xi}_i)^2}{2c_s^4} - \frac{\mathbf{u}^2}{2c_s^2} \right], \quad (2.52)$$

and the force term becomes

$$F_i = w_i \rho \mathbf{g} \cdot \left[ \frac{\boldsymbol{\xi}_i - \mathbf{u}}{c_s^2} + \frac{(\boldsymbol{\xi}_i \cdot \mathbf{u}) \boldsymbol{\xi}_i}{c_s^4} \right]. \quad (2.53)$$

Note that in the expressions of the equilibrium distribution function and the force term, the Hermite expansions are both truncated at the order  $N = 2$ . It will be proved in Section 2.5 that this truncation is adequate for retaining the hydrodynamic moments.

In addition, for the force term in Equation (2.53), its first several velocity moments can be easily computed as

$$\left\{ \begin{array}{l} \sum_i F_i = 0 \\ \sum_i \boldsymbol{\xi}_i F_i = \rho \mathbf{g}. \end{array} \right. \quad (2.54)$$

## 2.3 Lattice arrangement

The analysis in the previous Section 2.2 shows that the standard LBE is able to reproduce the hydrodynamic velocity moments of the original distribution function only when the lattice parameters, i.e. the discrete lattice speeds  $\xi_i$  and their corresponding weights  $w_i$ , are chosen in a way to make the Gauss-Hermite quadrature (2.24) accurate enough. In order to guarantee such accuracy, the weights corresponding to the discrete lattice speeds are required to satisfy Equation (A.8). Here, in this section, the parameters for the D2Q9 lattice, which is the lattice adopted in this thesis, are directly given. For more details on determining the weights for a given lattice, the reader is suggested to refer to [69, 158].

The D2Q9 lattice is named after a common rule of DdQq, where Dd stands for a  $d$ -dimensional system, and Qq means the number of the chosen discrete lattice speeds is  $q$ . Figure 2.1 schematically shows the configuration of D2Q9 lattice. The

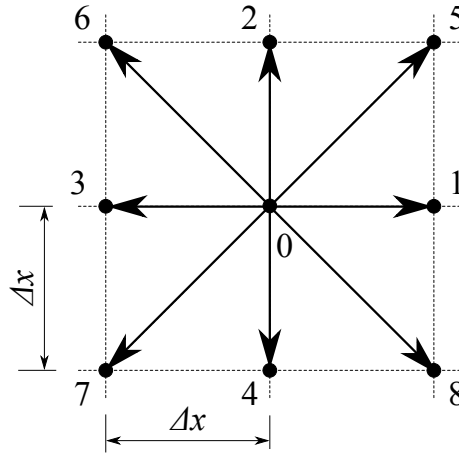


Figure 2.1 – D2Q9 lattice

nine discretized speed lie in the directions of the lattice linkages, i.e.

$$\xi_i = \begin{cases} (0, 0), & i = 0 \\ c \left( \cos \left[ \frac{(i-1)\pi}{2} \right], \sin \left[ \frac{(i-1)\pi}{2} \right] \right), & i = 1, \dots, 4 \\ \sqrt{2}c \left( \cos \left[ \frac{(2i-9)\pi}{4} \right], \sin \left[ \frac{(2i-9)\pi}{4} \right] \right), & i = 5, \dots, 8 \end{cases} \quad (2.55)$$

where  $i$  indicates a lattice direction, and  $c = \Delta x / \Delta t$  is a lattice constant representing the ratio of the lattice spacing  $\Delta x$  to the time step  $\Delta t$ . Note that the index  $i$  is set to be  $(i = 0, 1, \dots, 8)$ , which indicates a slight shift to  $(0, 1, \dots, q-1)$  from  $(1, 2, \dots, q)$  in Equations (2.40), (2.42) and (2.43). The term  $(\xi_i \Delta t)$  is the distance between two lattice nodes in the  $i$  direction.

The fluid density and flow velocity in the D2Q9 lattice are defined as the first two velocity moments of the distribution function, i.e.

$$\begin{cases} \rho = \sum_i f_i, \\ \mathbf{u} = \sum_i \boldsymbol{\xi}_i f_i. \end{cases} \quad (2.56)$$

The equilibrium distribution function for the SRT collision model reads

$$f_i^{\text{eq}} = w_i \rho \left[ 1 + \frac{\boldsymbol{\xi}_i \cdot \mathbf{u}}{c_s^2} + \frac{\mathbf{u}\mathbf{u} : (\boldsymbol{\xi}_i \boldsymbol{\xi}_i - c_s^2 \mathbf{I})}{2c_s^4} \right], \quad (2.57)$$

where the sound speed equals to  $c_s = \frac{c}{\sqrt{3}}$  according to [158], in which  $c = \Delta x / \Delta t = 1$  in our study. The weighting coefficient  $w_i$  is given as

$$w_i = \begin{cases} 4/9, & i = 0, \\ 1/9, & i = 1, 2, 3, 4, \\ 1/36, & i = 5, 6, 7, 8, \end{cases} \quad (2.58)$$

The velocity moments of the equilibrium distribution function are

$$\begin{cases} \sum_i f_i^{\text{eq}} = \rho, \\ \sum_i \boldsymbol{\xi}_i f_i^{\text{eq}} = \rho \mathbf{u}, \\ \sum_i \boldsymbol{\xi}_i \boldsymbol{\xi}_i f_i^{\text{eq}} = \rho \mathbf{u}\mathbf{u} + \rho c_s^2 \mathbf{I}. \end{cases} \quad (2.59)$$

In addition, the defined lattice speeds and the weights satisfy the following lattice symmetry

$$\left\{ \begin{aligned} \sum_i w_i &= 1, \\ \sum_i w_i e_{ij} &= 0, \\ \sum_i w_i e_{ij} e_{ik} &= c_s^2 \delta_{jk}, \\ \sum_i w_i e_{ij} e_{ik} e_{il} &= 0, \\ \sum_i w_i e_{ij} e_{ik} e_{il} e_{im} &= c_s^4 (\delta_{jk} \delta_{lm} + \delta_{jl} \delta_{km} + \delta_{jm} \delta_{kl}), \\ \sum_i w_i e_{ij} e_{ik} e_{il} e_{im} e_{in} &= 0. \end{aligned} \right. \quad (2.60)$$

## 2.4 Force model

A force model is crucial to the LBM because it takes into account the external forces in the fluid system and affects the accuracy of the numerical scheme. Following the aforementioned Hermite expansion procedure, the standard LBE with a force term is given in Equation (2.49), where the force term takes the form of Equation (2.53). Alternatively, He et al. [65] proposed to integrate the discrete Boltzmann equation (2.46) along the characteristic line  $\boldsymbol{\xi}$  over one time-step in order to derive the LBE with 2<sup>nd</sup>-order accuracy, which is expressed as

$$\begin{aligned}
 & f_i^{\text{orig}}(\mathbf{x} + \boldsymbol{\xi}_i \Delta t, t + \Delta t) - f_i^{\text{orig}}(\mathbf{x}, t) \\
 &= \frac{\Delta t}{2} \left\{ -\frac{1}{\tau \Delta t} \left[ f_i^{\text{orig}}(\mathbf{x}, t) - f_i^{\text{eq,orig}}(\mathbf{x}, t) \right] + F_i^{\text{orig}}(\mathbf{x}, t) \right\} \\
 &+ \frac{\Delta t}{2} \left\{ -\frac{1}{\tau \Delta t} \left[ f_i^{\text{orig}}(\mathbf{x} + \boldsymbol{\xi}_i \Delta t, t + \Delta t) - f_i^{\text{eq,orig}}(\mathbf{x} + \boldsymbol{\xi}_i \Delta t, t + \Delta t) \right] \right. \\
 &\left. + F_i^{\text{orig}}(\mathbf{x} + \boldsymbol{\xi}_i \Delta t, t + \Delta t) \right\}, \tag{2.61}
 \end{aligned}$$

where the right hand side of Equation (2.46) is integrated over one time-step using the trapezoidal rule that ensures the 2<sup>nd</sup>-order accuracy of this implicit lattice Boltzmann equation. By means of a change of variables [65, 34], an equivalent but explicit version of Equation (2.61) can be obtained as

$$\begin{aligned}
 & f_i(\mathbf{x} + \boldsymbol{\xi}_i \Delta t, t + \Delta t) - f_i(\mathbf{x}, t) \\
 &= -\frac{1}{\tau} [f_i(\mathbf{x}, t) - f_i^{\text{eq}}(\mathbf{x}, t)] + \Delta t \left( 1 - \frac{1}{2\tau} \right) F_i^{\text{orig}}(\mathbf{x}, t). \tag{2.62}
 \end{aligned}$$

It is important to note that in Equation (2.62), the definition of the distribution function  $f_i$  has changed from the original one in Equation (2.49). In this section, the new distribution function is kept being marked as  $f_i$ , while the original distribution function, as well as the original relaxation time, the original equilibrium distribution function in Equation (2.57) and the original force term in Equation (2.53), are denoted by the superscript "orig". The relation between  $f_i$  and  $f_i^{\text{orig}}$  is

$$f_i(\mathbf{x}, t) = \left( 1 + \frac{1}{2\tau} \right) f_i^{\text{orig}}(\mathbf{x}, t) - \frac{1}{2\tau} f_i^{\text{eq,orig}}(\mathbf{x}, t) - \frac{\Delta t}{2} F_i^{\text{orig}}(\mathbf{x}, t), \tag{2.63}$$

where  $\tau = \tau^{\text{orig}} + 0.5$  is the new dimensionless relaxation time. The first two velocity moments of the new distribution function are computed as follows based

on Equations (2.54), (2.56) and (2.59), i.e.

$$\begin{cases} \sum_i f_i = \rho \\ \sum_i \boldsymbol{\xi}_i f_i = \rho \mathbf{u} - \frac{\Delta t}{2} \rho \mathbf{g}. \end{cases} \quad (2.64)$$

Guo et al. [62] also obtained the same equations via a posteriori matching in order to eliminate the errors related to the body force term.

Following this procedure, the LBE with different force terms can be expressed in a more general form by introducing a coefficient  $\chi$  as

$$\begin{aligned} & f_i(\mathbf{x} + \boldsymbol{\xi}_i \Delta t, t + \Delta t) - f_i(\mathbf{x}, t) \\ &= -\frac{1}{\tau} [f_i(\mathbf{x}, t) - f_i^{\text{eq}}(\mathbf{x}, t)] + \Delta t \left(1 - \frac{\chi}{\tau}\right) F_i^{\text{orig}}(\mathbf{x}, t). \end{aligned} \quad (2.65)$$

where the distribution function is defined as

$$f_i(\mathbf{x}, t) = \left(1 + \frac{1}{2\tau}\right) f_i^{\text{orig}}(\mathbf{x}, t) - \frac{1}{2\tau} f_i^{\text{eq,orig}}(\mathbf{x}, t) - \chi \Delta t F_i^{\text{orig}}(\mathbf{x}, t). \quad (2.66)$$

The first two velocity moments of the newly defined distribution function  $f_i(\mathbf{x}, t)$  are calculated as

$$\begin{cases} \sum_i f_i = \rho \\ \sum_i \boldsymbol{\xi}_i f_i = \rho \mathbf{u} - \chi \Delta t \rho \mathbf{g}. \end{cases} \quad (2.67)$$

One may observe that adopting different values of  $\chi$  leads to different integration schemes for the force term:

- (I) Explicit scheme ( $\chi = 0$ ): This force model, as previously discussed in Section 2.2, was firstly proposed by Martys et al. [130]. It is observed that the time integration of the force term  $F_i^{\text{orig}}(\mathbf{x}, t)$  over one time-step is treated with a 1<sup>st</sup>-order explicit scheme. Since  $\chi = 0$ , the first two moments of  $f_i(\mathbf{x}, t)$  in Equation (2.67) are as the same as the ones of  $f_i^{\text{orig}}(\mathbf{x}, t)$ . Hence there is no need to take into account the body force effect when calculating the macroscopic velocity. However, by means of the Chapman-Enskog analysis, Guo et al. [62] showed that this explicit scheme introduces some errors in the presence of a time-varying non-uniform body force.
- (II) Semi-implicit scheme ( $\chi = 0.5$ ): This force model is previously shown as Equation (2.61) to (2.63), which is proposed by Guo et al. in [62]. As shown in Equation (2.61), the collision and force terms are both integrated in time

using a 2<sup>nd</sup>-order trapezoidal scheme. Guo et al. [62] showed that this model introduces the lowest errors among the existing force models.

- (III) Implicit scheme ( $\chi = 1$ ): The last case uses a fully implicit scheme for integrating the force term in time along the characteristic line, which is however 1<sup>st</sup>-order accurate in time and also needs the body force effect to be considered in the computation of macroscopic velocities.

For more comparisons of these force models, one can refer to our submitted paper in [113]. Here we shall only extract the following discussion of the choice of the force model in this study. In the present work, the semi-implicit force model (II) is adopted, because: (1) it can be systematically derived from the discrete Boltzmann equation with the help of the Hermite expansions; (2) a 2<sup>nd</sup>-order accuracy can be assured via a change of variables; (3) it introduces less errors than other force models, especially when the body force is not constant in space and time.

## 2.5 Multi-scale analysis

Before moving on to the numerical application of the LBM, it is necessary to verify that through calculating the distribution functions in the LBE, the corresponding macroscopic variables satisfy the N-S equations. The underlying philosophy can be found through a multi-scale Chapman-Enskog analysis. Such Chapman-Enskog analysis on the LBE has been illustrated in many published articles such as [24, 67], however it is difficult to include all the details in an article, which may add barriers for fully understanding the procedure. Besides, the Chapman-Enskog analysis with complete details on the LBE with Guo's force term [62] is rarely seen in the literature. In this section, the Chapman-Enskog multi-scale analysis will be employed for the LBE with Guo's force term [62] with all the necessary details and middle terms, among which the most important ones are marked in boxes.

### 2.5.1 Starting from the lattice Boltzmann equation

The starting point is the standard LBE with Guo's force term [62], i.e.

$$f_i(\mathbf{x} + \boldsymbol{\xi}_i \Delta t, t + \Delta t) - f_i(\mathbf{x}, t) = -\frac{1}{\tau} [f_i(\mathbf{x}, t) - f_i^{\text{eq}}(\mathbf{x}, t)] + \Delta t F_i(\mathbf{x}, t), \quad (2.68)$$

where the distribution function is defined in a way that the macroscopic fluid density and the flow velocity are calculated as

$$\begin{cases} \rho = \sum_i f_i, \\ \rho \mathbf{u}^* = \sum_i \boldsymbol{\xi}_i f_i + \frac{\Delta t}{2} \mathbf{F}, \end{cases} \quad (2.69)$$

in which the fluid velocity is newly marked as  $\mathbf{u}^*$  to be distinguished from Equation (2.56), and  $\mathbf{F} = \rho \mathbf{g}$  is the external body force. The coefficient of the force term in Equation (2.62) is absorbed into the force term, defined as

$$F_i = \left(1 - \frac{\Delta t}{2\tau}\right) w_i \left[ \frac{\mathbf{e}_i - \mathbf{u}^*}{c_s^2} + \frac{(\mathbf{e}_i \cdot \mathbf{u}^*) \mathbf{e}_i}{c_s^4} \right] \cdot \mathbf{F}. \quad (2.70)$$

The equilibrium distribution function in Guo's model [62] is given as

$$f_i^{\text{eq}} = w_i \rho \left[ 1 + \frac{\boldsymbol{\xi}_i \cdot \mathbf{u}^*}{c_s^2} + \frac{\mathbf{u}^* \mathbf{u}^* : (\boldsymbol{\xi}_i \boldsymbol{\xi}_i - c_s^2 \mathbf{I})}{2c_s^4} \right]. \quad (2.71)$$

Once again, one should keep in mind that the involved velocity term  $\mathbf{u}^*$  in Equation (2.71) is different from that in Equation (2.57), although the two equations are written in the same appearance. The leading velocity moments of the equilibrium distribution function are

$$\begin{cases} \sum_i f_i^{\text{eq}} = \rho, \\ \sum_i \boldsymbol{\xi}_i f_i^{\text{eq}} = \rho \mathbf{u}^*, \\ \sum_i \boldsymbol{\xi}_i \boldsymbol{\xi}_i f_i^{\text{eq}} = \rho \mathbf{u}^* \mathbf{u}^* + \rho c_s^2 \mathbf{I}. \end{cases} \quad (2.72)$$

## 2.5.2 Adopting Taylor expansion and multi-scale expansion

The very first step of the multi-scale analysis is applying a 2<sup>nd</sup>-order Taylor expansion around  $(\mathbf{x}, t)$  in Equation (2.68), which yields

$$\begin{aligned} \Delta t \frac{\partial f_i}{\partial t} + \boldsymbol{\xi}_i \Delta t \cdot \frac{\partial f_i}{\partial \mathbf{x}} + \frac{1}{2} \left[ \Delta t^2 \frac{\partial^2 f_i}{\partial t^2} + 2\Delta t (\boldsymbol{\xi}_i \Delta t) \cdot \frac{\partial^2 f_i}{\partial t \partial \mathbf{x}} + \Delta t^2 (\boldsymbol{\xi}_i \boldsymbol{\xi}_i) : \frac{\partial^2 f_i}{\partial \mathbf{x}^2} \right] \\ + \frac{1}{\tau} (f_i - f_i^{\text{eq}}) - \Delta t F_i = 0. \end{aligned} \quad (2.73)$$

Then, a series of multi-scale expansions is introduced here to analyze Equation (2.73), which are expressed as

$$f_i = f_i^{(0)} + \varepsilon f_i^{(1)} + \cdots, \quad (2.74)$$

$$\frac{\partial}{\partial t} = \varepsilon \frac{\partial}{\partial t_1} + \varepsilon^2 \frac{\partial}{\partial t_2} + \dots, \quad (2.75)$$

$$\frac{\partial}{\partial \mathbf{x}} = \varepsilon \frac{\partial}{\partial \mathbf{x}_1} + \dots, \quad (2.76)$$

$$F_i = \varepsilon F_i^{(1)} + \dots, \quad (2.77)$$

$$\mathbf{F} = \varepsilon \mathbf{F}^{(1)} + \dots, \quad (2.78)$$

where  $\varepsilon$  is a small positive parameter that leads to two smaller space scales and one smaller time scales, i.e.  $t_1 = \varepsilon t$ ,  $t_2 = \varepsilon^2 t$ , and  $\mathbf{x}_1 = \varepsilon \mathbf{x}$ .  $\mathbf{F}^{(1)}$  is the external force at the scale of  $\mathcal{O}(\varepsilon^1)$ , and  $F_i^{(1)}$  is the discrete force term at  $\mathcal{O}(\varepsilon^1)$  scale. It is important to note that these multi-scale expansions are not written in a complete form, for instance the time derivative at  $t_0$  time scale and the space derivative at  $\mathbf{x}_0$  space scale are not emphasized here. We will not dig deep into the underlying mechanism in this study. Instead, by knowing that the expansions (2.74-2.78) is commonly used for illustrating the recovery of the N-S equations from the LBE, as being adopted in [24, 67], we shall accept these formulas and focus on the details of the following discussion on the recovery of the N-S equations.

Introducing the above multi-scale expansions to substitute the derivatives in Equation (2.73) and reserving only the terms up to the order of  $\mathcal{O}(\varepsilon^2)$ , the derivatives are expanded as

$$\frac{\partial f_i}{\partial t} = \varepsilon \frac{\partial f_i^{(0)}}{\partial t_1} + \varepsilon^2 \frac{\partial f_i^{(0)}}{\partial t_2} + \varepsilon^2 \frac{\partial f_i^{(1)}}{\partial t_2} + \mathcal{O}(\varepsilon^3), \quad (2.79)$$

$$\frac{\partial f_i}{\partial \mathbf{x}} = \varepsilon \frac{\partial f_i^{(0)}}{\partial \mathbf{x}_1} + \varepsilon^2 \frac{\partial f_i^{(1)}}{\partial \mathbf{x}_1} + \mathcal{O}(\varepsilon^3), \quad (2.80)$$

$$\frac{\partial^2 f_i}{\partial t^2} = \varepsilon^2 \frac{\partial^2 f_i^{(0)}}{\partial t_1^2} + \mathcal{O}(\varepsilon^3), \quad (2.81)$$

$$\frac{\partial^2 f_i}{\partial t \partial \mathbf{x}} = \varepsilon^2 \frac{\partial^2 f_i^{(0)}}{\partial t_1 \partial \mathbf{x}_1} + \mathcal{O}(\varepsilon^3), \quad (2.82)$$

$$\frac{\partial^2 f_i}{\partial \mathbf{x}^2} = \varepsilon^2 \frac{\partial^2 f_i^{(0)}}{\partial \mathbf{x}_1^2} + \mathcal{O}(\varepsilon^3). \quad (2.83)$$

Thus Equation (2.73) becomes:

$$\begin{aligned}
 & \frac{1}{\tau\Delta t} \left( f_i^{(0)} - f_i^{\text{eq}} + \varepsilon f_i^{(1)} + \varepsilon^2 f_i^{(2)} \right) - \varepsilon F_i^{(1)} + \varepsilon \frac{\partial f_i^{(0)}}{\partial t_1} + \varepsilon \boldsymbol{\xi}_i \cdot \frac{\partial f_i^{(0)}}{\partial \mathbf{x}_1} \\
 & + \varepsilon^2 \frac{\partial f_i^{(0)}}{\partial t_2} + \varepsilon^2 \frac{\partial f_i^{(1)}}{\partial t_1} + \varepsilon^2 \boldsymbol{\xi}_i \cdot \frac{\partial f_i^{(1)}}{\partial \mathbf{x}_1} \\
 & + \varepsilon^2 \frac{\Delta t}{2} \left( \frac{\partial^2 f_i^{(0)}}{\partial t_1^2} + 2\boldsymbol{\xi}_i \cdot \frac{\partial^2 f_i^{(0)}}{\partial t_1 \partial \mathbf{x}_1} + \boldsymbol{\xi}_i \boldsymbol{\xi}_i : \frac{\partial^2 f_i^{(0)}}{\partial \mathbf{x}_1^2} \right) + \mathcal{O}(\varepsilon^3) = 0.
 \end{aligned} \tag{2.84}$$

Neglecting the high order terms and comparing the two sides of the above equation, the equation at each scale reads

$$\boxed{\mathcal{O}(\varepsilon^0) : 0 = \frac{1}{\tau\Delta t} \left( f_i^{(0)} - f_i^{\text{eq}} \right)}, \tag{2.85}$$

$$\boxed{\mathcal{O}(\varepsilon^1) : 0 = \frac{1}{\tau\Delta t} f_i^{(1)} + D_1 f_i^{(0)} - F_i^{(1)}}, \tag{2.86}$$

$$\begin{aligned}
 \mathcal{O}(\varepsilon^2) : & -\frac{1}{\tau\Delta t} f_i^{(2)} = \frac{\partial f_i^{(0)}}{\partial t_2} + D_1 f_i^{(1)} \\
 & + \frac{\Delta t}{2} \left( \frac{\partial^2 f_i^{(0)}}{\partial t_1^2} + 2\boldsymbol{\xi}_i \cdot \frac{\partial^2 f_i^{(0)}}{\partial t_1 \partial \mathbf{x}_1} + \boldsymbol{\xi}_i \boldsymbol{\xi}_i : \frac{\partial^2 f_i^{(0)}}{\partial \mathbf{x}_1^2} \right),
 \end{aligned} \tag{2.87}$$

where the operator  $D_k$  is defined as  $D_k f = \frac{f}{\partial t_k} + \boldsymbol{\xi}_i \cdot \frac{f}{\mathbf{x}_k}$ . By calculating the time and space derivatives of the terms from Equation (2.86) at  $\mathcal{O}(\varepsilon^1)$ , which are

$$\frac{\partial^2 f_i^{(0)}}{\partial t_1^2} + \boldsymbol{\xi}_i \cdot \frac{\partial^2 f_i^{(0)}}{\partial t_1 \partial \mathbf{x}_1} = -\frac{1}{\tau\Delta t} \frac{\partial f_i^{(1)}}{\partial t_1} + \frac{\partial F_i^{(1)}}{\partial t_1}, \tag{2.88}$$

$$\frac{\partial^2 f_i^{(0)}}{\partial t_1 \partial \mathbf{x}_1} + \boldsymbol{\xi}_i \cdot \frac{\partial^2 f_i^{(0)}}{\partial \mathbf{x}_1^2} = -\frac{1}{\tau\Delta t} \frac{\partial f_i^{(1)}}{\partial \mathbf{x}_1} + \frac{\partial F_i^{(1)}}{\partial \mathbf{x}_1}, \tag{2.89}$$

the terms inside the parentheses in Equation (2.87) can be further simplified as

$$\frac{\partial^2 f_i^{(0)}}{\partial t_1^2} + 2\boldsymbol{\xi}_i \cdot \frac{\partial^2 f_i^{(0)}}{\partial t_1 \partial \mathbf{x}_1} + \boldsymbol{\xi}_i \boldsymbol{\xi}_i : \frac{\partial^2 f_i^{(0)}}{\partial \mathbf{x}_1^2} = -\frac{1}{\tau\Delta t} D_1 f_i^{(1)} + D_1 F_i^{(1)}. \tag{2.90}$$

Hence the balance of the coefficients at  $\mathcal{O}(\varepsilon^2)$  reads

$$\boxed{\mathcal{O}(\varepsilon^2) : -\frac{1}{\tau\Delta t} f_i^{(2)} = \frac{\partial f_i^{(0)}}{\partial t_2} + \left( 1 - \frac{1}{2\tau} \right) D_1 f_i^{(1)} + \frac{\Delta t}{2} D_1 F_i^{(1)}}. \tag{2.91}$$

### 2.5.3 Velocity moments of associated ingredients

Based on the equality of the coefficients at different scales, i.e. Equation (2.85), (2.86) and (2.91), the core procedure of the Chapman-Enskog analysis can be carried out by calculating the velocity moments on both sides of these equations. For the sake of simplicity and the clarity of this procedure, the velocity moments of all the ingredients at each scales are better to be specified in advance. The velocity moments concerned are the ones up to the 3<sup>rd</sup>-order of  $f^{(0)}$ ,  $F_i$  and  $F_i^{(1)}$ , as well as the ones up to the 2<sup>nd</sup>-order of  $f^{(1)}$ . Hereinafter, we note the 2<sup>nd</sup>-order moment of distribution functions as  $\mathbf{\Pi}$  and the 3<sup>rd</sup>-order moment as  $\mathbf{\Gamma}$ , i.e.  $\mathbf{\Pi} = \sum_i \xi_i \xi_i f_i$  and  $\mathbf{\Gamma} = \sum_i \xi_i \xi_i \xi_i f_i$ . Additional superscripts like " $\square^{(0)}$ " can be added to indicate the operations at the corresponding scales, for example  $\mathbf{\Gamma}^{(0)} = \sum_i \xi_i \xi_i \xi_i f_i^{(0)}$ .

It can be obviously obtained from Equation (2.85) that

$$f_i^{(0)} = f_i^{\text{eq}}. \quad (2.92)$$

Based on Equation (2.72), the distribution function  $f_i^{(0)}$  satisfies

$$\begin{cases} \sum_i f_i^{(0)} = \rho, \\ \sum_i \xi_i f_i^{(0)} = \rho \mathbf{u}^*, \\ \mathbf{\Pi}^{(0)} = \rho \mathbf{u}^* \mathbf{u}^* + \rho c_s^2 \mathbf{I}. \end{cases} \quad (2.93)$$

It is also known that the velocity moments of the distribution function can be computed by definition, as shown in Equation (2.69). Combining Equation (2.69), (2.93) and the truncated expansion  $f_i = f_i^{(0)} + \varepsilon f_i^{(1)} + \varepsilon^2 f_i^{(2)}$ , the several moments of  $f_i^{(1)}$  and  $f_i^{(2)}$  can be obtained after simple arithmetic operations, which are

$$\begin{cases} \sum_i f_i^{(1)} = 0 \\ \sum_i \xi_i f_i^{(1)} = -\frac{\Delta t}{2} \mathbf{F}, \end{cases} \quad (2.94)$$

and

$$\sum_i f_i^{(2)} = 0. \quad (2.95)$$

For the moment, the 3<sup>rd</sup>-order moment of  $f_i^{(0)}$  and the 2<sup>nd</sup>-order moment of  $f^{(1)}$  remain unclear, we will come to them later.

As for the force term  $F_i$ , it is obviously observed that its definition in Equation (2.70) matches the form of Equation (A.5), hence its velocity moments can be

easily obtained as

$$\left\{ \begin{array}{l} \sum_i F_i = 0, \\ \sum_i \xi_i F_i = \left(1 - \frac{1}{2\tau}\right) \mathbf{F}, \\ \sum_i \xi_i \xi_i F_i = \left(1 - \frac{1}{2\tau}\right) 2\mathbf{u}^* \mathbf{F}. \end{array} \right. \quad (2.96)$$

Similarly, based on the definition of the force term at  $\mathcal{O}(\varepsilon^1)$  scale in Equation (2.77), the following moments can be obtained,

$$\left\{ \begin{array}{l} \sum_i F_i^{(1)} = 0, \\ \sum_i \xi_i F_i^{(1)} = \left(1 - \frac{1}{2\tau}\right) \mathbf{F}^{(1)}, \\ \sum_i \xi_i \xi_i F_i^{(1)} = \left(1 - \frac{1}{2\tau}\right) 2\mathbf{u}^* \mathbf{F}^{(1)} \end{array} \right. \quad (2.97)$$

#### 2.5.4 Velocity moment of $\mathcal{O}(\varepsilon^1)$ and $\mathcal{O}(\varepsilon^2)$ terms

By adopting Equations (2.93-2.97), the velocity moments on both sides of Equation (2.86) and (2.91) can be specified.

(i) The 0<sup>th</sup>-order velocity moment of the  $\mathcal{O}(\varepsilon^1)$  Equation (2.86) is computed as

$$\boxed{\frac{\partial \rho}{\partial t_1} + \nabla_1 \cdot (\rho \mathbf{u}^*) = 0}, \quad (2.98)$$

where the operator  $\nabla$  represents the space derivative:  $\nabla = \frac{\partial}{\partial \mathbf{x}}$ , and the subscript number indicates the operation scale, for example  $\nabla_1 = \frac{\partial}{\partial \mathbf{x}_1}$ .

(ii) The 1<sup>st</sup>-order moment of the  $\mathcal{O}(\varepsilon^1)$  Equation (2.86) reads

$$\boxed{\frac{\partial (\rho \mathbf{u}^*)}{\partial t_1} + \nabla_1 \cdot \mathbf{\Pi}^{(0)} = \mathbf{F}^{(1)}}. \quad (2.99)$$

(iii) Similarly, The 0<sup>th</sup>-order velocity moment of the  $\mathcal{O}(\varepsilon^2)$  Equation (2.91) is

$$\boxed{\frac{\partial \rho}{\partial t_2} = 0}. \quad (2.100)$$

(iv) The 1<sup>st</sup>-order velocity moment of the  $\mathcal{O}(\varepsilon^2)$  Equation (2.91) is

$$\frac{\partial(\rho \mathbf{u}^*)}{\partial t_2} + \left(1 - \frac{1}{2\tau}\right) (\nabla_1 \cdot \mathbf{\Pi}^{(1)}) = -\Delta t \left(1 - \frac{1}{2\tau}\right) \nabla_1 \cdot (\mathbf{u}^* \mathbf{F}^{(1)}). \quad (2.101)$$

Note that the 2<sup>nd</sup>-order moment term  $\mathbf{\Pi}^{(1)}$  is still unclear for the moment. In the next paragraph,  $\mathbf{\Pi}^{(1)}$  will be specified.

### 2.5.5 Specifying $\mathbf{\Pi}^{(1)}$

From Equation (2.86),  $f_i^{(1)}$  can be expressed as

$$f_i^{(1)} = -\tau \Delta t \left( D_1 f_i^{(0)} - F_i^{(1)} \right). \quad (2.102)$$

Thus  $\mathbf{\Pi}^{(1)}$  becomes

$$\begin{aligned} \mathbf{\Pi}^{(1)} &= -\tau \Delta t \left[ \frac{\partial \mathbf{\Pi}^{(0)}}{\partial t_1} + \nabla_1 \cdot \mathbf{\Gamma}^{(0)} - \left(1 - \frac{1}{2\tau}\right) 2\mathbf{u}^* \mathbf{F}^{(1)} \right] \\ &= -\tau \Delta t \left[ \frac{\partial(\rho \mathbf{u}^* \mathbf{u}^*)}{\partial t_1} + c_s^2 \frac{\partial \rho}{\partial t_1} \mathbf{I} + \nabla_1 \cdot \mathbf{\Gamma}^{(0)} - \left(1 - \frac{1}{2\tau}\right) 2\mathbf{u}^* \mathbf{F}^{(1)} \right] \end{aligned} \quad (2.103)$$

where Equations (2.93) and (2.97) are adopted. The four terms in the square bracket above will be computed one by one, in a tensor form where  $l$ ,  $m$  and  $n$  are indexes.

- (i) Specifying  $\frac{\partial(\rho \mathbf{u}^* \mathbf{u}^*)}{\partial t_1}$ , i.e.  $\frac{\partial(\rho u_l^* u_m^*)}{\partial t_1}$ , needs much work. We shall start from rewriting Equation (2.98) and Equation (2.99) in a tensor form, which gives

$$\frac{\partial \rho}{\partial t_1} + \frac{\partial(\rho u_n^*)}{\partial x_{1n}} = 0 \quad (2.104)$$

and

$$\frac{\partial(\rho u_m^*)}{\partial t_1} + \frac{\partial}{\partial x_{1n}} (\rho u_m^* u_n^* + \rho c_s^2 \delta_{mn}) = F_m^{(1)}, \quad (2.105)$$

where  $\delta_{mn}$  is the Kronecker delta symbol. By noting that  $\frac{\partial(\rho u_m^*)}{\partial t_1} = \rho \frac{\partial u_m^*}{\partial t_1} + u_m^* \frac{\partial \rho}{\partial t_1}$  and using Equation (2.104), Equation (2.105) can be rewritten as

$$\rho \frac{\partial u_m^*}{\partial t_1} - u_m^* \frac{\partial(\rho u_n^*)}{\partial x_{1n}} + \frac{\partial}{\partial x_{1n}} (\rho u_m^* u_n^* + \rho c_s^2 \delta_{mn}) = F_m^{(1)}. \quad (2.106)$$

We also have

$$\frac{\partial(\rho u_l^* u_m^*)}{\partial t_1} = \rho u_l^* \frac{\partial u_m^*}{\partial t_1} + u_m^* \frac{\partial(\rho u_l^*)}{\partial t_1}. \quad (2.107)$$

The two components at the right-hand side can be found in Equations (2.105) and (2.106). A small trick is done here to match the first term in Equation (2.105) with the second component, by using another set of indexes to rewrite Equation (2.105) as

$$\frac{\partial(\rho u_l^*)}{\partial t_1} + \frac{\partial}{\partial x_{1n}}(\rho u_l^* u_n^* + \rho c_s^2 \delta_{ln}) = F_l^{(1)}. \quad (2.108)$$

Based on Equations (2.106) and Equation (2.108),  $\frac{\partial \rho u_l^* u_m^*}{\partial t_1}$  can be temporarily expressed as

$$\begin{aligned} \frac{\partial(\rho u_l^* u_m^*)}{\partial t_1} &= \rho u_l^* \frac{\partial u_m^*}{\partial t_1} + u_m^* \frac{\partial(\rho u_l^*)}{\partial t_1} \\ &= u_l^* F_m^{(1)} + u_m^* F_l^{(1)} \\ &+ u_l^* u_m^* \frac{\partial(\rho u_n^*)}{\partial x_{1n}} - u_l^* \frac{\partial(\rho u_m^* u_n^*)}{\partial x_{1n}} - u_m^* \frac{\partial(\rho u_l^* u_n^*)}{\partial x_{1n}} \\ &- c_s^2 \left( u_l^* \frac{\partial \rho}{\partial x_m} + u_m^* \frac{\partial \rho}{\partial x_l} \right). \end{aligned} \quad (2.109)$$

Furthermore, the three terms in the second line of the above equation can be further condensed as

$$u_l^* u_m^* \frac{\partial(\rho u_n^*)}{\partial x_{1n}} - u_l^* \frac{\partial(\rho u_m^* u_n^*)}{\partial x_{1n}} - u_m^* \frac{\partial(\rho u_l^* u_n^*)}{\partial x_{1n}} = - \frac{\partial(\rho u_l^* u_m^* u_n^*)}{\partial x_{1n}}. \quad (2.110)$$

Finally,

$$\boxed{\frac{\partial(\rho u_l^* u_m^*)}{\partial t_1} = u_l^* F_m^{(1)} + u_m^* F_l^{(1)} - c_s^2 \left( u_l^* \frac{\partial \rho}{\partial x_{1m}} + u_m^* \frac{\partial \rho}{\partial x_{1l}} \right) - \frac{\partial(\rho u_l^* u_m^* u_n^*)}{\partial x_{1n}}}. \quad (2.111)$$

(ii) The term  $c_s^2 \frac{\partial \rho}{\partial t_1} \mathbf{I}$  is written in tensor form as

$$\boxed{c_s^2 \delta_{lm} \frac{\partial \rho}{\partial t_1}}. \quad (2.112)$$

(iii) Using a tensor form,  $\mathbf{\Gamma}^{(0)}$  can be rewritten as

$$\Gamma_{lmn}^{(0)} = \rho c_s^2 (u_n^* \delta_{lm} + u_m^* \delta_{ln} + u_l^* \delta_{mn}) \quad (2.113)$$

with the help of Equation (2.71). Hence,  $\nabla_1 \cdot \mathbf{F}^{(0)}$  can be expressed as

$$\boxed{\frac{\partial \Gamma_{lmn}^{(0)}}{\partial x_{1n}} = c_s^2 \left[ \delta_{lm} \frac{\partial (\rho u_n^*)}{\partial x_{1n}} + \frac{\partial (\rho u_m^*)}{\partial x_{1l}} + \frac{\partial (\rho u_l^*)}{\partial x_{1m}} \right]}. \quad (2.114)$$

(iv) The last term  $\left[ - \left( 1 - \frac{1}{2\tau} \right) 2\mathbf{u}^* \mathbf{F}^{(1)} \right]$  is written in tensor form as

$$\boxed{- \left( 1 - \frac{1}{2\tau} \right) \left( u_l^* F_m^{(1)} + u_m^* F_l^{(1)} \right)}. \quad (2.115)$$

Combining the four boxed expressions (2.111), (2.112), (2.114) and (2.115), the unknown 2<sup>nd</sup>-order moment  $\mathbf{\Pi}^{(1)}$  can be expressed as

$$\begin{aligned} \Pi_{lm}^{(1)} &= -\tau \Delta t \left[ \left( c_s^2 \frac{\partial (\rho u_m^*)}{\partial x_{1l}} - c_s^2 u_m^* \frac{\partial \rho}{\partial x_l} \right) + \left( c_s^2 \frac{\partial (\rho u_l^*)}{\partial x_{1m}} - c_s^2 u_l^* \frac{\partial \rho}{\partial x_m} \right) \right. \\ &\quad \left. + \left( c_s^2 \delta_{lm} \frac{\partial \rho}{\partial t_1} + c_s^2 \delta_{lm} \frac{\partial (\rho u_n^*)}{\partial x_{1n}} \right) + \frac{1}{2\tau} \left( u_l^* F_m^{(1)} + u_m^* F_l^{(1)} \right) - \frac{\partial (\rho u_l^* u_m^* u_n^*)}{\partial x_n} \right] \\ &= -\tau \Delta t \left[ \rho c_s^2 \left( \frac{\partial u_l^*}{\partial x_m} + \frac{\partial u_m^*}{\partial x_l} \right) + \frac{1}{2\tau} \left( u_l^* F_m^{(1)} + u_m^* F_l^{(1)} \right) - \frac{\partial (\rho u_l^* u_m^* u_n^*)}{\partial x_n} \right], \end{aligned} \quad (2.116)$$

where Equation (2.104) is used in the simplification. The last term in the above square bracket, i.e.  $\left[ - \frac{\partial (\rho u_l^* u_m^* u_n^*)}{\partial x_{1n}} \right]$ , which is in the order of  $\mathcal{O}(\mathbf{u}^3)$ , can be neglected when the Mach number is relatively low.

Finally,  $\mathbf{\Pi}^{(1)}$  is approximated as

$$\boxed{\mathbf{\Pi}^{(1)} = -\tau \Delta t \rho c_s^2 \left[ \nabla_1 \mathbf{u}^* + (\nabla_1 \mathbf{u}^*)^T \right] - \Delta t \mathbf{u}^* \mathbf{F}^{(1)}}. \quad (2.117)$$

Bringing Equation (2.117) back into the 1<sup>st</sup>-order velocity moments of the  $\mathcal{O}(\varepsilon^2)$  coefficients, i.e. Equation (2.101), one can find out that the terms involving the body force on both sides are balanced, which yields

$$\boxed{\frac{\partial (\rho \mathbf{u}^*)}{\partial t_2} - \Delta t c_s^2 \left( \tau - \frac{1}{2} \right) \nabla_1 \cdot \left\{ \rho \left[ \nabla_1 \mathbf{u}^* + (\nabla_1 \mathbf{u}^*)^T \right] \right\}} = \mathbf{0}. \quad (2.118)$$

## 2.5.6 Recovering the Navier-Stokes equation

Till now, the 0<sup>th</sup>- and 1<sup>st</sup>-order moments of the coefficients at  $\mathcal{O}(\varepsilon^1)$  and  $\mathcal{O}(\varepsilon^2)$  level are obtained, which are given in Equations (2.98), (2.99), (2.100) and (2.118).

For convenience, they are gathered here as

$$\frac{\partial \rho}{\partial t_1} + \nabla_1 \cdot (\rho \mathbf{u}^*) = 0, \quad (2.119)$$

$$\frac{\partial (\rho \mathbf{u}^*)}{\partial t_1} + \nabla_1 \cdot \mathbf{\Pi}^{(0)} = \mathbf{F}^{(1)}, \quad (2.120)$$

$$\frac{\partial \rho}{\partial t_2} = 0, \quad (2.121)$$

$$\frac{\partial (\rho \mathbf{u}^*)}{\partial t_2} - \Delta t c_s^2 \left( \tau - \frac{1}{2} \right) \nabla_1 \cdot \left\{ \rho \left[ \nabla_1 \mathbf{u}^* + (\nabla_1 \mathbf{u}^*)^\top \right] \right\} = \mathbf{0}. \quad (2.122)$$

By imposing the multi-scale expansion in a reversed direction on Equations (2.119-2.122), the macroscopic equations at the original scale  $\mathbf{x}$  and  $t$  can be obtained. Adopting Equation (2.119) and Equation (2.121) yields

$$\frac{\partial \rho}{\partial t} + \nabla \cdot (\rho \mathbf{u}^*) = 0. \quad (2.123)$$

Using Equation (2.120) and Equation (2.122) yields

$$\begin{aligned} & \frac{\partial (\rho \mathbf{u}^*)}{\partial t} + \nabla \cdot (\rho \mathbf{u}^* \mathbf{u}^*) \\ &= -\nabla (\rho c_s^2) + \Delta t c_s^2 \left( \tau - \frac{1}{2} \right) \nabla \cdot \left\{ \rho \left[ \nabla \mathbf{u}^* + (\nabla \mathbf{u}^*)^\top \right] \right\} + \mathbf{F}. \end{aligned} \quad (2.124)$$

Comparing the above equation with the moment conservation equation of the weakly compressible fluid flow, i.e. Equation (2.4), one can find out that in the LBM, the fluid pressure is defined as

$$p = \rho c_s^2 \quad (2.125)$$

and the fluid viscosity is defined as

$$\nu = \Delta t c_s^2 \left( \tau - \frac{1}{2} \right). \quad (2.126)$$

As a summary, the N-S equations are recovered from the LB equation through the Chapman-Enskog analysis. It is worth noticing that this recovery neglects a  $\mathcal{O}(\mathbf{u}^3)$  order term in the momentum conservation equation, which indicates that the LBM actually simulates a weakly compressible flow at small Mach numbers to approximate an incompressible fluid [33]. It is also observed from the Chapman-Enskog analysis that the convection term and the pressure term in the momentum conservation come from the 2<sup>nd</sup>-order velocity moment of  $f_i^{(0)}$ , and the viscous term is contributed from the 2<sup>nd</sup>-order velocity moment of  $f_i^{(1)}$ .

## 2.6 Boundary conditions

From the aforementioned Chapman-Enskog analysis, the LB equation is proved to be 2<sup>nd</sup>-order accurate. However, the general accuracy of LBM does not only depend on the LB equation, but also on the treatment of the boundary conditions, since the distribution functions at the boundary are not calculated from the LBE. Hence the mechanism of the distribution function behavior at the boundaries will largely influence LBM's overall performance. Not like the boundary conditions in traditional CFD methods that directly involve the macroscopic variables, the conditions for particle distribution functions in LBM need special consideration. In this section, different types of boundary conditions used in the subsequent simulations are presented.

### 2.6.1 Bounce back boundary condition

A non-slip solid wall can be mimicked by a bounce back boundary condition. The particle distribution functions are assumed to bounce back without any loss in the opposite direction after they hit the non-slip boundary. Since the distribution function moves from one lattice node to its neighbor within one time-step, the exact timing of the bounce back and its mathematical expression vary depending on the location of the non-slip wall.

Figure 2.2 shows the case where the wall is located in the middle of two layers of lattice nodes. The three post-collision distribution functions, which depart at

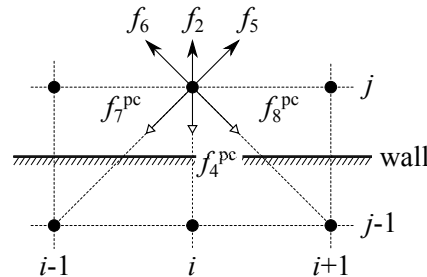


Figure 2.2 – Half-way bounce back boundary condition

time  $t$  from node  $(i, j)$  towards the wall, will reach the wall at time  $(t + 0.5\Delta t)$ . In the same way as for the collision procedure, the bounce back of the distribution function is assumed to take place instantaneously. Under this hypothesis, the bounced back post-collision distribution functions go back to node  $(i, j)$  at the end of the streaming process at time  $(t + \Delta t)$ . This operation is called the half-way bounce back. The missing distribution functions are computed as

$$f_2((i, j), t + \Delta t) = f_4^{\text{pc}}((i, j), t), \quad (2.127)$$

$$f_5((i, j), t + \Delta t) = f_7^{\text{pc}}((i, j), t), \quad (2.128)$$

$$f_6((i, j), t + \Delta t) = f_8^{\text{pc}}((i, j), t). \quad (2.129)$$

Otherwise, if the wall is represented by lattice nodes as shown in Figure 2.3, the unknown distribution functions of the boundary nodes at time  $(t + \Delta t)$  are obtained from the post-collision distribution functions which come from the neighboring inner layer of nodes at time  $t$  and reverse when colliding with the wall at time instant  $(t + \Delta t)$ . In this so-called full-way bounce back boundary condition,

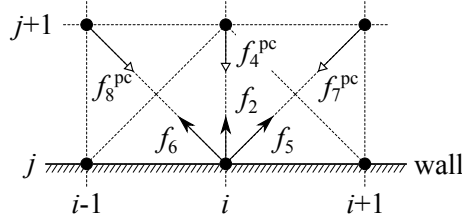


Figure 2.3 – Full-way bounce back boundary condition

the unknown distribution functions are calculated as

$$f_2((i, j), t + \Delta t) = f_4^{\text{pc}}((i, j + 1), t), \quad (2.130)$$

$$f_5((i, j), t + \Delta t) = f_7^{\text{pc}}((i + 1, j + 1), t), \quad (2.131)$$

$$f_6((i, j), t + \Delta t) = f_8^{\text{pc}}((i - 1, j + 1), t). \quad (2.132)$$

It is noted here that in the standard bounce back model, a collision rule which is similar to that of the full-way bounce back is employed in the fluid node closest to the wall, instead of the boundary node. To be distinguished from the standard bounce back, the full-way bounce back model presented here is also called the modified bounce back model [72, 61].

The bounce back boundary condition enjoys much popularity due to its easy implementation and high efficiency, thus it is recommended to apply bounce back condition on straight walls if possible. For a more general case where the wall is not located as in Figures 2.2 and 2.3, or even for curved walls, one can find other appropriate boundary conditions, including the nodal bounce back boundary condition [61] and the interpolation schemes based on bounce back [43, 133, 19], etc.

## 2.6.2 Specular boundary condition

The specular boundary condition [117] is developed for free-slip boundaries. When a distribution function hit the free-slip wall, its vertical velocity component is assumed to bounce back in the opposite direction, while its tangential velocity

remains unchanged. Similarly with the bounce back conditions, different wall positions should be treated individually. In the case shown in Figure 2.4, the free-slip boundary lies in the middle between two node layers. Hence the distribution func-

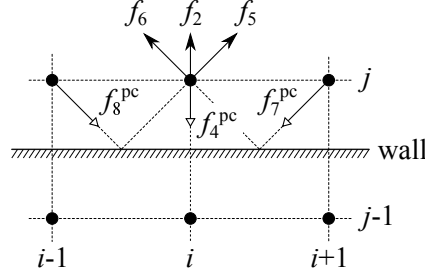


Figure 2.4 – Half-way specular boundary condition

tions with horizontal components, which are  $f_7^{\text{pc}}$  and  $f_8^{\text{pc}}$ , will shift to a neighbor node after one time step. The distribution function with only a vertical component,  $f_4^{\text{pc}}$ , moves similarly as for the half-way bounce back boundary condition. Thus the unknown distribution functions of node  $(i, j)$  are obtained as

$$f_2((i, j), t + \Delta t) = f_4^{\text{pc}}((i, j), t), \quad (2.133)$$

$$f_5((i, j), t + \Delta t) = f_8^{\text{pc}}((i-1, j), t), \quad (2.134)$$

$$f_6((i, j), t + \Delta t) = f_7^{\text{pc}}((i+1, j), t). \quad (2.135)$$

Specially, the specular boundary condition is identical to the symmetric boundary condition. Taking the case in Figure 2.4 as an example and regarding the wall as a symmetry axis, the fluid on both sides of the symmetry axis should be moving in an opposite way, for instance

$$f_2((i, j), t) = f_4((i, j-1), t), \quad (2.136)$$

$$f_5^{\text{pc}}((i, j), t) = f_8^{\text{pc}}((i, j-1), t), \quad (2.137)$$

and so on. Following a standard streaming process, one can easily obtain the same equations as for specular boundaries.

### 2.6.3 Zou-He boundary condition

The Zou-He boundary condition [72] is a pressure and velocity boundary condition designed for moving boundaries. Taking the lid-driven cavity test case as an example, the Zou-He boundary condition can be used for simulating the moving lid. See Figure 2.5, the upper lid is moving horizontally with a speed of  $(u, v)$ . For a boundary node at the lid, the  $f_1, f_2, f_3, f_5$  and  $f_6$  can be obtained from standard LBE, while  $f_4, f_7$  and  $f_8$  are unknown. From the definition of the distribution

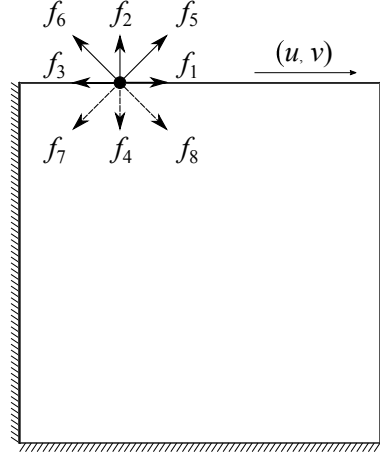


Figure 2.5 – Zou-He boundary condition

function, the fluid density and momentum can be expressed as

$$\rho = f_0 + f_1 + f_2 + f_3 + f_4 + f_5 + f_6 + f_7 + f_8, \quad (2.138)$$

$$\rho u = f_1 + f_5 + f_8 - f_3 - f_6 - f_7, \quad (2.139)$$

$$\rho v = f_2 + f_5 + f_6 - f_4 - f_7 - f_8, \quad (2.140)$$

where  $\rho$  is also an unknown variable, so another equation is needed to close the system. He et al. [72] consider a bounce back mechanism of the non-equilibrium distribution function

$$f_4 - f_4^{\text{eq}} = f_2 - f_2^{\text{eq}}, \quad (2.141)$$

where the equilibrium part,  $f_2^{\text{eq}}$  and  $f_4^{\text{eq}}$ , can be calculated from Equation (2.57). Combining the Equations (2.138-2.141) yields

$$\rho = \frac{1}{1+v} [f_0 + f_1 + f_3 + 2(f_2 + f_5 + f_6)], \quad (2.142)$$

$$f_4 = f_2 - \frac{2}{3}\rho u, \quad (2.143)$$

$$f_7 = f_5 + \frac{1}{2}(f_1 - f_3) - \frac{1}{6}\rho v - \frac{1}{2}\rho u, \quad (2.144)$$

$$f_8 = f_6 + \frac{1}{2}(f_3 - f_1) - \frac{1}{6}\rho v + \frac{1}{2}\rho u. \quad (2.145)$$

Similarly, Zou-He boundary condition for east, west or south wall can be easily obtained.

## 2.6.4 Periodic boundary condition

The periodic boundary is a common boundary type, for example the inlet and outlet boundaries of a Poiseuille flow driven by a constant volume force  $F$ , as shown

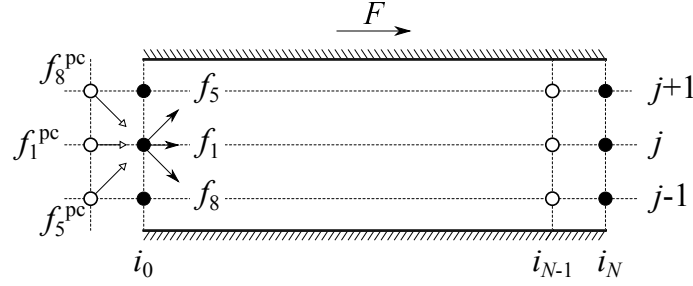


Figure 2.6 – Periodic boundary condition

in Figure 2.6. By definition, the fluid flowing out will enter the inlet again. Hence the nodes at the inlet can read upstream information from the outlet boundary, and the nodes at the outlet can read downstream information from the inlet. Taking the node  $(i_0, j)$  at the inlet as an example, its unknown distribution functions can be obtained as

$$f_1((i_0, j), t + \Delta t) = f_1^{\text{pc}}((i_{N-1}, j), t), \quad (2.146)$$

$$f_5((i_0, j), t + \Delta t) = f_5^{\text{pc}}((i_{N-1}, j - 1), t), \quad (2.147)$$

$$f_8((i_0, j), t + \Delta t) = f_8^{\text{pc}}((i_{N-1}, j + 1), t). \quad (2.148)$$

### 2.6.5 Free-surface boundary condition

In the present study, the free-surface flow is simulated by a single-phase model, where the free-surface is actually a boundary of the liquid domain. The adopted boundary condition for the free-surface will be illustrated in Chapter 4.

## 2.7 Rescaling factors

In the practical implementation, it is suggested to use dimensionless variables in the LBM code. For an arbitrary variable  $\phi$ , its value in the physical scale is noted as  $\phi^{\text{phy}}$ , and its value in the lattice scale is noted as  $\phi^{\text{lat}}$ . The rescaling factor is  $C_\phi$ , which indicates the ratio of the physical value  $\phi^{\text{phy}}$  to the lattice value  $\phi^{\text{lat}}$ , i.e.  $C_\phi = \frac{\phi^{\text{phy}}}{\phi^{\text{lat}}}$ . When initializing a simulation, the rescaling factors of the length, time and density need to be specified at first, i.e.  $C_x$ ,  $C_t$  and  $C_\rho$ .  $C_x$  equals  $C_x = \frac{L}{N} = \delta x$  for a given lattice resolution  $N$  in one characteristic length  $L$ .  $C_t$  is the time-step, i.e.  $C_t = \Delta t$ . Then the rescaling coefficients for velocity, viscosity,

acceleration and pressure can be determined as

$$\left\{ \begin{array}{l} C_u = \frac{C_x}{C_t}, \\ C_\nu = \frac{C_x^2}{C_t}, \\ C_g = \frac{C_x}{C_t^2}, \\ C_p = C_\rho C_u C_x \end{array} \right. \quad (2.149)$$

In the post-processing process, the physical variable value can be computed from the corresponding lattice value and the rescaling factor as

$$\phi^{\text{phy}} = C_\phi \phi^{\text{lat}}. \quad (2.150)$$

## 2.8 Algorithm

The LBM algorithm is summarized as follows, where the external force term is calculated by Guo's force model.

---

**Algorithm:** SRT-LBM

---

**Initialization:** Determine  $C_x$ ,  $C_t$  and  $C_\rho$  and initialize  $f_i(\mathbf{x}, t^0)$ ,  $\rho(\mathbf{x}, t^0)$ ,  $\mathbf{u}^*(\mathbf{x}, t^0)$  and  $\mathbf{F}(\mathbf{x}, t^0)$

---

**Routine:**

Require:  $f_i(\mathbf{x}, t^n)$ ,  $\rho(\mathbf{x}, t^n)$ ,  $\mathbf{u}^*(\mathbf{x}, t^n)$  and  $\mathbf{F}(\mathbf{x}, t^n)$  from the previous time-step

1. Compute  $f_i^{\text{eq}}(\mathbf{x}, t^n)$  with Equation (2.71) and  $F_i(\mathbf{x}, t^n)$  with Equation (2.70),
2. Carry out the SRT collision process in Equation (2.50),
3. Carry out the streaming process in Equation (2.51), for obtaining  $f_i(\mathbf{x}, t^{n+1})$ ,
4. Adapt the missing distribution functions from proper boundary conditions,
5. Compute  $\rho(\mathbf{x}, t^{n+1})$  and  $\mathbf{u}^*(\mathbf{x}, t^{n+1})$  by the definition (2.69), calculate the pressure by definition (2.125), and adapt  $\mathbf{F}(\mathbf{x}, t^{n+1})$ ,
6. Goto 1. for the next time-step.

---

**Post-processing:** Output the values of the physical variables by Equation (2.150).

---

# Chapter 3

## Regularized lattice Boltzmann method

The adopted regularized lattice Boltzmann method (RLBM) [189] is studied, improved and validated in this chapter. Through a theoretical analysis based on the Hermite expansion and the Chapman-Enskog analysis, it is proved that the RLBM eliminates the undesired non-hydrodynamic components in the distribution function, and subsequently improves the stability of LBM. In addition, the starting order of the regularization in the reference [189] is corrected for the adopted force model, which is verified by a force-driven Poiseuille flow test-case. Based on this corrected procedure, the Taylor-Green vortex and the lid-driven cavity test-cases are studied, through which the performance of RLBM is analyzed in terms of convergence, accuracy, CPU time and the ability of stabilizing the LBM scheme.

La méthode adoptée de Boltzmann sur réseau régularisé (RLBM) [189] est étudiée; améliorée et validée dans ce chapitre. On montre, par une analyse théorique basée sur un développement en série de Hermite et l'analyse de Chapman-Enskog, que la RLBM peut éliminer les composants non-hydrodynamiques indésirables dans les fonctions de distribution et améliorer la stabilité de la LBM. De plus, l'ordre auquel la régularisation commence est adapté pour le modèle de force adopté, ce qui est validé par un cas test d'écoulements de Poiseuille. Ensuite, les cas-tests des tourbillons de Taylor-Green et de la cavité entraînée sont étudiés avec la méthode RLBM, proposée. Les performances de la RLBM sont analysées en termes de convergence, de précision, de temps CPU et de capacité de stabilisation.

## Contents

---

<b>3.1</b>	<b>Instability analysis from the viewpoint of regularization</b>	<b>55</b>
3.1.1	Non-hydrodynamic information contained in the LBE . . . . .	55
3.1.2	Hermite regularization of the non-equilibrium distribution function . . . . .	58
<b>3.2</b>	<b>Algorithm</b> . . . . .	<b>61</b>
<b>3.3</b>	<b>Convergency analysis of the RLBM</b> . . . . .	<b>62</b>
<b>3.4</b>	<b>Numerical validation on the lid-driven cavity</b> . . . . .	<b>64</b>
3.4.1	Regularization-based boundary condition . . . . .	65
3.4.2	Numerical results . . . . .	69

---

## 3.1 Instability analysis from the viewpoint of regularization

In the domain of fluid dynamics, the LBM serves as a numerical solver of the governing equations for fluid flows, hence it has always been interesting and necessary to make clear the potential sources that might cause numerical instabilities. Different existing instability analyses have been reviewed in Section 1.3.1. Here, in this section, the instability analysis for LBM is carried out from the viewpoint of the regularization, based on the theoretical supports of Chapter 2.

### 3.1.1 Non-hydrodynamic information contained in the LBE

When the word *instability* is mentioned in this study, we mean the instability that appears at the N-S level. It is well known that the N-S equation contains the smallest amount of information compared with LBE and CBE, see Section 1.3.1. The information loss from the CBE to N-S, as can be found in Chapter 2 for all the details, is summarized as follows.

#### From Boltzmann level to lattice level

The continuous Boltzmann equation reads

$$\frac{\partial f}{\partial t} + \boldsymbol{\xi} \cdot \nabla f = -\frac{1}{\tau \Delta t} (f - f^{\text{eq}}) + F, \quad (3.1)$$

where  $F = -\mathbf{g} \cdot \nabla_{\boldsymbol{\xi}} f$  is the force term. The distribution function  $f$ , the equilibrium distribution function  $f^{\text{eq}}$  and the force  $F$  can be substituted by full Hermite expansions without any loss, which gives

$$\left\{ \begin{array}{l} f = \omega \sum_{n=0}^{\infty} \frac{1}{n!} \mathbf{a}^{(n)} : \mathcal{H}^{(n)}, \\ f^{\text{eq}} = \omega \sum_{n=0}^{\infty} \frac{1}{n!} \mathbf{a}_{\text{eq}}^{(n)} : \mathcal{H}^{(n)}, \\ F = \omega \sum_{n=0}^{\infty} \frac{1}{n!} \mathbf{a}_F^{(n)} : \mathcal{H}^{(n)}. \end{array} \right. \quad (3.2)$$

Then, it is proposed by the LB theory to replace the full Hermite expansions

with the truncated ones, i.e.

$$\left\{ \begin{array}{l} f \approx f^N = \omega \sum_{n=0}^N \frac{1}{n!} \mathbf{a}^{(n)} : \mathcal{H}^{(n)}, \\ f^{\text{eq}} \approx f^{\text{eq},N} = \omega \sum_{n=0}^N \frac{1}{n!} \mathbf{a}_{\text{eq}}^{(n)} : \mathcal{H}^{(n)}, \\ F \approx F^N = \omega \sum_{n=0}^N \frac{1}{n!} \mathbf{a}_F^{(n)} : \mathcal{H}^{(n)}. \end{array} \right. \quad (3.3)$$

A common operation is to truncate the expansions at  $N = 2$ . The reason of doing so is that the hydrodynamic moments of the original distribution function in the velocity space stay unchanged after the truncation, thanks to the Hermite polynomials. By making use of the Gauss-Hermite quadrature, the hydrodynamic moments can be accurately reproduced based on only several distribution functions with discrete velocities, i.e.  $f^N(\mathbf{x}, \boldsymbol{\xi}_i, t)$ . Note that the variables in the CBE (3.1), such as  $f(\mathbf{x}, \boldsymbol{\xi}, t)$ ,  $f^{\text{eq}}(\mathbf{x}, \boldsymbol{\xi}, t)$  and  $F(\mathbf{x}, \boldsymbol{\xi}, t)$ , are functions of  $\mathbf{x}$ ,  $\boldsymbol{\xi}$  and  $t$ , which indicates that the CBE (3.1) is valid at every point in the phase-space of  $(\mathbf{x}, \boldsymbol{\xi}, t)$ . Therefore, by setting  $\boldsymbol{\xi} = \boldsymbol{\xi}_i$  in Equation (3.1), one has

$$\left. \frac{\partial f}{\partial t} \right|_{\boldsymbol{\xi}=\boldsymbol{\xi}_i} + \boldsymbol{\xi}_i \cdot \left. \frac{\partial f}{\partial \mathbf{x}} \right|_{\boldsymbol{\xi}=\boldsymbol{\xi}_i} = -\frac{1}{\tau \Delta t} [f(\mathbf{x}, \boldsymbol{\xi}_i, t) - f^{\text{eq}}(\mathbf{x}, \boldsymbol{\xi}_i, t)] + F(\mathbf{x}, \boldsymbol{\xi}_i, t). \quad (3.4)$$

Due to the independence of the variables  $\mathbf{x}$ ,  $\boldsymbol{\xi}$  and  $t$ , it is possible to rewrite the derivatives as

$$\left. \frac{\partial f}{\partial t} \right|_{\boldsymbol{\xi}=\boldsymbol{\xi}_i} = \frac{\partial f(\mathbf{x}, \boldsymbol{\xi}_i, t)}{\partial t} \quad \text{and} \quad \left. \frac{\partial f}{\partial \mathbf{x}} \right|_{\boldsymbol{\xi}=\boldsymbol{\xi}_i} = \frac{\partial f(\mathbf{x}, \boldsymbol{\xi}_i, t)}{\partial \mathbf{x}}, \quad (3.5)$$

which allows one to obtain the Boltzmann equation on a discrete velocity space as

$$\begin{aligned} & \frac{\partial f^N(\mathbf{x}, \boldsymbol{\xi}_i, t)}{\partial t} + \boldsymbol{\xi}_i \cdot \nabla f^N(\mathbf{x}, \boldsymbol{\xi}_i, t) \\ &= -\frac{1}{\tau \Delta t} [f^N(\mathbf{x}, \boldsymbol{\xi}_i, t) - f^{\text{eq},N}(\mathbf{x}, \boldsymbol{\xi}_i, t)] + F^N(\mathbf{x}, \boldsymbol{\xi}_i, t). \end{aligned} \quad (3.6)$$

At last, by introducing the following definitions,

$$f_i \equiv \frac{w_i f^N(\mathbf{x}, \boldsymbol{\xi}_i, t)}{\omega(\boldsymbol{\xi}_i)}, \quad f_i^{\text{eq}} \equiv \frac{w_i f^{\text{eq},N}(\mathbf{x}, \boldsymbol{\xi}_i, t)}{\omega(\boldsymbol{\xi}_i)} \quad \text{and} \quad F_i \equiv \frac{w_i F^N(\mathbf{x}, \boldsymbol{\xi}_i, t)}{\omega(\boldsymbol{\xi}_i)}, \quad (3.7)$$

the Boltzmann equation at the lattice level is obtained as

$$\frac{\partial f_i}{\partial t} + \boldsymbol{\xi}_i \cdot \nabla f_i = -\frac{1}{\tau \Delta t} (f_i - f_i^{\text{eq}}) + F_i. \quad (3.8)$$

Notice that the variables, i.e.  $f_i(\mathbf{x}, t)$ ,  $f_i^{\text{eq}}(\mathbf{x}, t)$  and  $F_i(\mathbf{x}, t)$  are defined at the lattice level. In the practice, a 1<sup>st</sup>-order up-wind approximation is adopted for the left-hand side terms, which gives

$$f_i(\mathbf{x} + \boldsymbol{\xi}_i \Delta t, t + \Delta t) - f_i(\mathbf{x}, t) = -\frac{1}{\tau} [f_i(\mathbf{x}, t) - f_i^{\text{eq}}(\mathbf{x}, t)] + \Delta t F_i(\mathbf{x}, t). \quad (3.9)$$

It is now concluded that the information loss in the LBE (3.9), compared with the CBE (3.1), is due to the truncation in the Hermite expansion, and the up-wind approximation.

### From lattice level to N-S level

The rest part of the journey from the Boltzmann level to the N-S level starts from the LBE (3.9) and is guided by the multi-scale Chapman-Enskog analysis as previously presented in Section 2.5. The Chapman-Enskog analysis expands the distribution function as a summation of components on small scales that are characterized by a small parameter  $\varepsilon$ , which gives

$$f_i = f_i^{(0)} + \varepsilon f_i^{(1)} + \dots. \quad (3.10)$$

Following the mathematical derivations illustrated in Section 2.5, one may observe that the high order components, i.e.  $f^{(n \geq 3)}$ , are neglected in the above expansion. Yet this truncation is still not explicitly expressed in the N-S equation. In fact, the N-S equation can be recovered through the Chapman-Enskog analysis, as long as the following velocity moments are held, i.e.

$$\left\{ \begin{array}{l} \sum_i f_i^{(0)} = \rho, \\ \sum_i \boldsymbol{\xi}_i f_i^{(0)} = \rho \mathbf{u}^*, \\ \boldsymbol{\Pi}^{(0)} = \rho \mathbf{u}^* \mathbf{u}^* + \rho c_s^2 \mathbf{I}, \end{array} \right. \quad (3.11)$$

$$\left\{ \begin{array}{l} \sum_i f_i^{(1)} = 0, \\ \sum_i \boldsymbol{\xi}_i f_i^{(1)} = -\frac{\Delta t}{2} \mathbf{F}, \\ \boldsymbol{\Pi}^{(1)} = -\tau \Delta t \rho c_s^2 \left[ \nabla_1 \mathbf{u} + (\nabla_1 \mathbf{u})^T \right] - \Delta t \mathbf{u}^* \mathbf{F}^{(1)}, \end{array} \right. \quad (3.12)$$

and

$$\sum_i f_i^{(2)} = 0, \quad (3.13)$$

where  $\mathbf{u}^*$  is the fluid velocity, and  $\mathbf{F}^{(1)}$  is the  $\mathcal{O}(\varepsilon^1)$  component of the force  $\mathbf{F}$ . Shortly speaking, the N-S equations are only related to the first several velocity moments of the distribution function components of orders up to  $\mathcal{O}(\varepsilon^2)$ . In other words, as concluded by Zhang et al. [189], the distribution function in LBE (3.9) may contain high order components that are not useful for recovering the N-S equations but might destabilize the numerical simulation of LBM.

### 3.1.2 Hermite regularization of the non-equilibrium distribution function

#### Discussion about the starting order of the regularization

Introducing the concept of the Hilbert space as used in [189], the truncated Hermite expansion (3.3) regularizes the corresponding functions into a sub-space  $\mathbb{H}^N$  spanned by the first  $N$  leading Hermite basis terms, namely in this case, into  $\mathbb{H}^2$ . Noticing that in the LBM algorithm (see Section 2.8), the equilibrium distribution function and the force term are both computed from the macroscopic variables through

$$f_i^{\text{eq}} = w_i \rho \left[ 1 + \frac{\boldsymbol{\xi}_i \cdot \mathbf{u}^*}{c_s^2} + \frac{\mathbf{u}^* \mathbf{u}^* : (\boldsymbol{\xi}_i \boldsymbol{\xi}_i - c_s^2 \mathbf{I})}{2c_s^4} \right]. \quad (3.14)$$

and

$$F_i = \left( 1 - \frac{\Delta t}{2\tau} \right) w_i \left[ \frac{\mathbf{e}_i - \mathbf{u}^*}{c_s^2} + \frac{(\mathbf{e}_i \cdot \mathbf{u}^*) \mathbf{e}_i}{c_s^4} \right] \cdot \mathbf{F}, \quad (3.15)$$

which guarantees that  $f_i^{\text{eq}}$  and  $F_i$  are naturally inside the  $\mathbb{H}^2$  space. However, the distribution function  $f_i$  may somehow get some undesired non-hydrodynamic information during the calculation, for instance from the treatment of boundary conditions. Hence the purpose of adopting the regularization is to regularize the distribution function  $f_i$  into the  $\mathbb{H}^2$  space.

Splitting the distribution function  $f_i$  into an equilibrium part  $f_i^{\text{eq}}$  and a non-equilibrium part  $f_i^{\text{neq}}$ , one can extract the non-equilibrium part as

$$f_i^{\text{neq}} = f_i - f_i^{\text{eq}}, \quad (3.16)$$

where  $f_i^{\text{neq}}$  is the part that contains undesired high order components.

Following the idea proposed in [189], after each streaming step, one replaces  $f_i^{\text{neq}}$  by  $f_i^{\text{neq},N}$ , which is a Hermite truncation series truncated at order  $N = 2$

$$f_i^{\text{neq},N} = \omega \sum_{n=0}^N \frac{1}{n!} \mathbf{a}_{\text{neq},N}^{(n)} : \mathcal{H}^{(n)}, \quad (3.17)$$

where the  $n^{\text{th}}$ -order ( $n \leq N$ ) expansion coefficient is computed as

$$\mathbf{a}_{\text{neq},N}^{(n)} = \mathbf{a}_{\text{neq}}^{(n)} = \sum_i f_i^{\text{neq},N} \mathcal{H}_i^{(n)} = \sum_i (f_i - f_i^{\text{eq}}) \mathcal{H}_i^{(n)} \quad (3.18)$$

with the associated Hermite polynomials as

$$\begin{cases} \mathcal{H}^{(0)} = 1, \\ \mathcal{H}^{(1)} = \frac{1}{c_s} \boldsymbol{\xi}_i, \\ \mathcal{H}^{(2)} = \frac{1}{c_s^2} \boldsymbol{\xi}_i \boldsymbol{\xi}_i - \mathbf{I}. \end{cases} \quad (3.19)$$

It is important to note here that, it is suggested by Zhang et al. [189] to start the construction of  $f_i^{\text{neq},N}$  directly from the 2<sup>nd</sup>-order term, since the 0<sup>th</sup>-order and 1<sup>st</sup>-order terms are equal to zero by definition. However, this is true only with the explicit force model ( $\chi = 0$ , see Item (I) in Section 2.4). With the semi-implicit force model ( $\chi = 0.5$ , see Item (II) in Section 2.4) that is adopted in this study, only the 0<sup>th</sup>-order expansion coefficient of  $f_i^{\text{neq},N}$  is equal to zero, i.e.  $\mathbf{a}_{\text{neq}}^{(0)} = 0$  but  $\mathbf{a}_{\text{neq}}^{(1)} \neq 0$ . This is due to the existence of the force term  $F_i$  in the definition (2.63) of  $f_i$ . As a consequence, the construction of  $f_i^{\text{neq},N}$  must start from the 1<sup>st</sup>-order term. In the present work, we choose to construct  $f_i^{\text{neq},N}$  up to the same order as  $f_i^{\text{eq}}$ , i.e.  $N = 2$ , which gives

$$\begin{aligned} f_i^{\text{neq},N=2} &= w_i \left( \mathbf{a}_{\text{neq}}^{(1)} \cdot \mathcal{H}^{(1)} + \frac{1}{2} \mathbf{a}_{\text{neq}}^{(2)} : \mathcal{H}^{(2)} \right) \\ &= w_i \left\{ \left[ \sum_j (f_j - f_j^{\text{eq}}) \frac{\mathbf{e}_j}{c_s} \right] \cdot \frac{\mathbf{e}_i}{c_s} \right. \\ &\quad \left. + \frac{1}{2} \left[ \sum_j (f_j - f_j^{\text{eq}}) \left( \frac{1}{c_s^2} \mathbf{e}_j \mathbf{e}_j - \mathbf{I} \right) \right] : \left( \frac{1}{c_s^2} \boldsymbol{\xi}_i \boldsymbol{\xi}_i - \mathbf{I} \right) \right\}, \end{aligned} \quad (3.20)$$

where  $j$  is another lattice index.

### Validation: Poiseuille flow driven by a body force

A test case of 2D Poiseuille flow is carried out here to verify the importance of including the 1<sup>st</sup>-order term in the regularization procedure as discussed in the previous section. Figure 3.1 illustrates the configuration of the test-case. A channel between two infinite non-slip plates is full of calm fluid, and a constant body force  $\mathbf{F}$  is imposed inside the channel to drive the flow. The body force is simulated by the semi-implicit force model [62] ( $\chi = 0.5$ , see Item (II) in Section

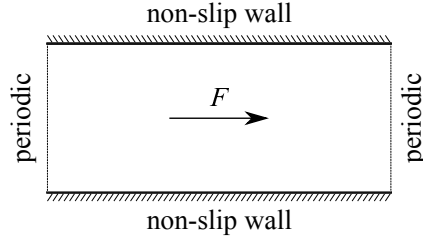


Figure 3.1 – Configuration of the 2D Poiseuille flow test-case. A constant body force  $\mathbf{F}$  is imposed inside the channel between two non-slip solid plates. Periodic boundary condition is applied at the left and right boundaries of the computation domain.

2.4). The modified bounce-back boundary condition (see Section 2.6.1) is adopted at the upper and bottom boundaries of the computation domain in order to ensure the non-slip condition, and the periodic boundary condition (see Section 2.6.4) is applied at the left and right boundaries. The analytical solution of the horizontal fluid velocity along a vertical line across the channel is given as

$$\mathbf{u}(y) = \frac{\mathbf{g}}{2\nu}y(H - y), \quad (3.21)$$

where  $H$  is the channel width,  $\nu$  is the viscosity, and  $\mathbf{g}$  is the acceleration induced by the body force  $\mathbf{F}$ .  $y$  denotes the  $y$ -coordinate with  $y = 0$  at the bottom plate and  $y = H$  at the upper plate. The Reynolds number is defined as

$$Re = \frac{u_{\max}H}{\nu}, \quad (3.22)$$

where the maximum velocity is  $u_{\max} = \frac{gH^2}{8\nu}$ , which appears at the horizontal centerline of the channel.

Two kinds of regularization procedure of the non-equilibrium distribution functions are adopted. The first one starts from the 2<sup>nd</sup>-order term, as suggested in [189]. The other one starts from the 1<sup>st</sup>-order term, i.e. Equation (3.20). The values of some necessary parameters for the calculation are listed in Table 3.1.

Table 3.1 – Some necessary parameters for the 2D Poiseuille flow test-case.

$N_x$	$N_y$	$C_x$	$C_t$	$\tau$	$g$	$Re$	$Ma$
5	41	1.0	0.02	0.6697	0.01	10	0.0245

Figure 3.2 shows the numerical results of the two regularization schemes, and the analytical solution as well. In this comparison, it can be clearly observed that the regularization including both the 1<sup>st</sup>-order and the 2<sup>nd</sup>-order terms gives a numerical result superimposed to the analytical solution. Whereas the result

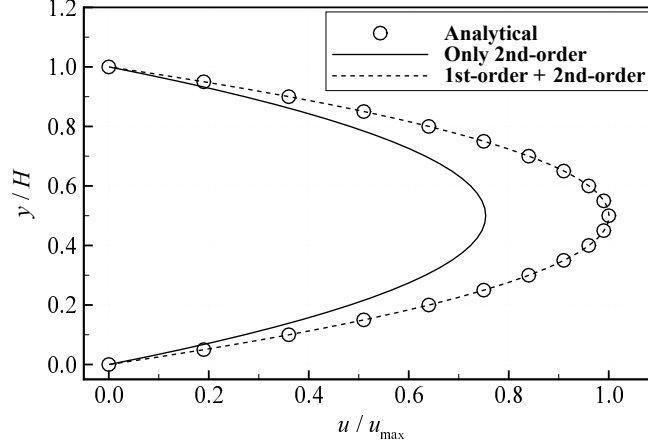


Figure 3.2 – Numerical results and the analytical solution of the horizontal velocity along the vertical centerline for the 2D Poiseuille flow test-case.

obtained from the regularization starting directly from the 2<sup>nd</sup>-order term appears much different from the analytical solution, due to the fact that the body force effect has not been taken into account in the reconstruction of  $f_i^{\text{neq}, N=2}$ . This numerical example verifies the theoretical demonstration in the previous section, confirming that it is necessary to start the Hermite regularization from the 1<sup>st</sup>-order term when using the semi-implicit scheme for the force term.

## 3.2 Algorithm

Following the common practice, the LBE with a regularized distribution function can be separated into a collision step and a streaming step as

$$\text{Collision : } f_i^{\text{pc}}(\mathbf{x}, t) = f_i^{\text{eq}}(\mathbf{x}, t) + \left(1 - \frac{1}{\tau}\right) f_i^{\text{neq}, N=2}(\mathbf{x}, t) + \Delta t F_i(\mathbf{x}, t), \quad (3.23)$$

$$\text{Streaming : } f_i(\mathbf{x} + \mathbf{e}_i \Delta t, t + \Delta t) = f_i^{\text{pc}}(\mathbf{x}, t). \quad (3.24)$$

Accordingly, the present RLBM algorithm can be summarized as follows,

---

### Algorithm: RLBM

---

**Require:**  $f_i(\mathbf{x}, t^n)$ ,  $\rho(\mathbf{x}, t^n)$ ,  $\mathbf{u}^*(\mathbf{x}, t^n)$  and  $\mathbf{F}(\mathbf{x}, t^n)$  from the previous time-step

1. Compute  $f_i^{\text{eq}}(\mathbf{x}, t^n)$  with Equation (3.14) and  $F_i(\mathbf{x}, t^n)$  with Equation (3.15),
2. Extract  $f_i^{\text{neq}}(\mathbf{x}, t^n)$  by Equation (3.16),
3. Calculate  $\mathbf{a}_{\text{neq}}^{(n)}$  from Equation (3.18),
4. Obtain  $f_i^{\text{neq}, N=2}$  using Equation (3.20),

5. Carry out the RSRT collision step in Equation (3.23),
  6. Carry out the streaming step in Equation (3.24),
  7. Adapt the missing distribution functions from proper boundary conditions,
  8. Compute  $\rho(\mathbf{x}, t^{n+1})$ ,  $\mathbf{u}^*(\mathbf{x}, t^{n+1})$  by the definition in Equation (2.69),
  9. Goto Step.1 for the next time-step.
- 

### 3.3 Convergency analysis of the RLBM

#### Taylor-Green vortex

In this section, a Taylor-Green vortex test-case is studied in order to verify numerically that the adopted regularization procedure does not affect the convergence order of the LBM. As shown in Figure 3.3, the Taylor-Green vortex flow in a square domain  $[0, L] \times [0, L]$  with periodic boundary conditions is considered.

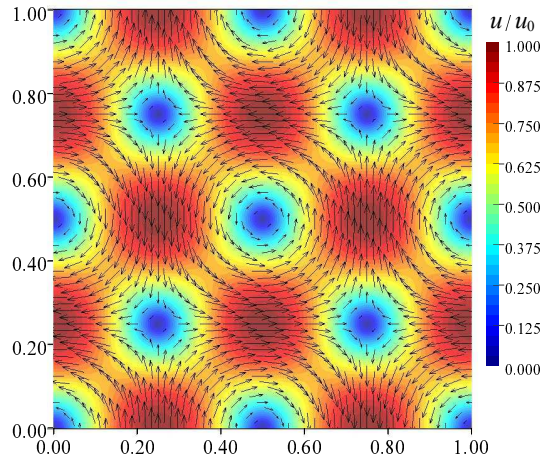


Figure 3.3 – The initial state of the Taylor-Green vortex test-case at  $t = 0$ . The color in the contour represents the relative velocity magnitude. The oriented arrow indicates the relative velocity.

The analytical solution of the flow field is given as

$$\begin{cases} v_x(x, y, t) = -U_0 \cos(kx) \sin(ky) e^{-2k^2 \nu t}, \\ v_y(x, y, t) = U_0 \sin(kx) \cos(ky) e^{-2k^2 \nu t}, \\ p(x, y, t) = p_0 - \frac{\rho_0 U_0^2}{4} [\cos(2kx) + \cos(2ky)] e^{-4k^2 \nu t}, \end{cases} \quad (3.25)$$

where  $v_x$  and  $v_y$  respectively denote the velocity components in the  $x$ - and  $y$ -directions, and  $p = \rho c_s^2$  is the pressure. The coefficient  $k$  is computed as  $k = \frac{2\pi}{L}$ .  $U_0$  and  $p_0$  are the characteristic velocity and pressure.  $\nu = \frac{U_0 L}{Re}$  is the kinematic

viscosity, where the Reynolds number is chosen as  $Re = 100$  in this test-case. The total calculation time is set as  $T = \frac{L}{U_0}$ . Figure 3.4 shows that the present numerical results agree well with the analytical solution.

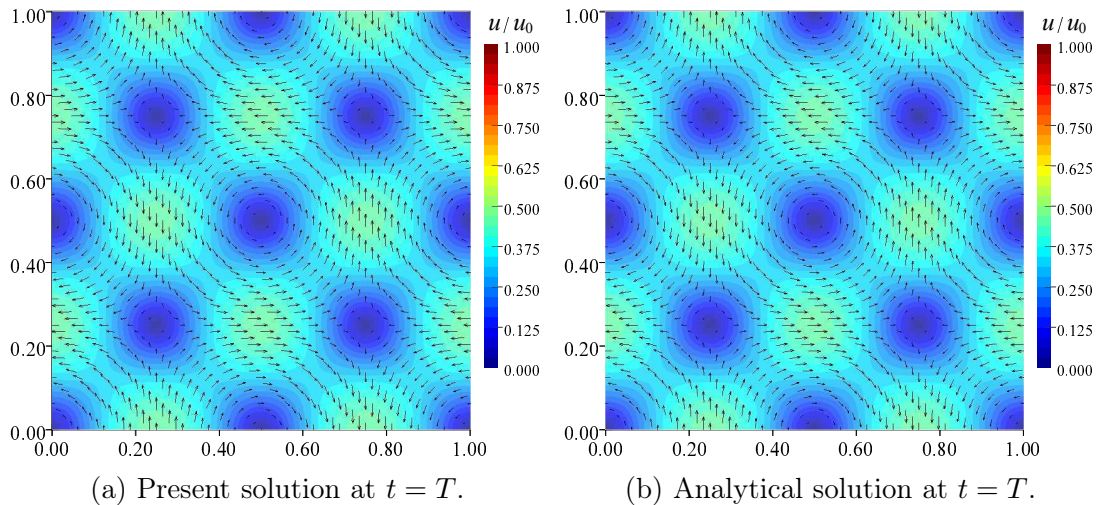


Figure 3.4 – Comparison of the relative velocity fields of the Taylor-Green vortex test-case at time  $t = T$ . The left subfigure shows the present RLBM solution with a  $513 \times 513$  lattice, and the right one shows the analytical solution.

### Convergence study

To evaluate the convergence order, the errors of the velocity fields are measured for four lattice resolutions, which are  $N_x \times N_y = 65 \times 65$ ,  $129 \times 129$ ,  $257 \times 257$  and  $513 \times 513$ , with  $N_x$  and  $N_y$  denoting respectively the number of discretization points in the  $x$ - and  $y$ -directions. For all the four lattice resolutions, the dimensionless relaxation time is fixed at  $\tau = 0.596$ . The error is evaluated as

$$Error = \sqrt{\frac{1}{N_x N_y} \sum_j \frac{\|v_j^{\text{num}} - v_j^{\text{ana}}\|^2}{U_0^2}}, \quad (3.26)$$

where  $v_j^{\text{num}} = v^{\text{num}}(x_j, T)$  and  $v_j^{\text{ana}} = v^{\text{ana}}(x_j, T)$  denote the numerical and analytical velocity vectors at the  $j^{\text{th}}$ -node at the final instant  $t = T$ . The numerical results are obtained with both the SRT-LBM and the RLBM for comparison.

Table 3.3 lists the numerical errors for different mesh resolutions and the CPU times ( $t^{\text{CPU}}$ ) consumed by the SRT-LBM and RLBM, in which the listed CPU times are all relative to the first result obtained for the  $65 \times 65$  SRT-LBM calculation. One can clearly find out that the RLBM gives a slightly smaller error than the SRT-LBM, although the RLBM is computationally more demanding than the SRT-LBM.

Table 3.3 – Numerical errors obtained for the Taylor-Green vortex test-case at  $Re = 100$  with  $\tau = 0.596$ . The listed CPU times are relative to that of the  $65 \times 65$  SRT-LBM result.

Mesh size	$Error_{\text{SRT-LBM}}$	$Error_{\text{RLBM}}$	$t_{\text{SRT-LBM}}^{\text{CPU}}$	$t_{\text{RLBM}}^{\text{CPU}}$
$65 \times 65$	$3.1473 \times 10^{-4}$	$2.9025 \times 10^{-4}$	1.0	1.5
$129 \times 129$	$7.8366 \times 10^{-5}$	$7.1902 \times 10^{-5}$	13.4	21.4
$257 \times 257$	$2.0171 \times 10^{-5}$	$1.8588 \times 10^{-5}$	253.8	394.2
$513 \times 513$	$4.9317 \times 10^{-6}$	$4.5245 \times 10^{-6}$	3618.2	5812.1

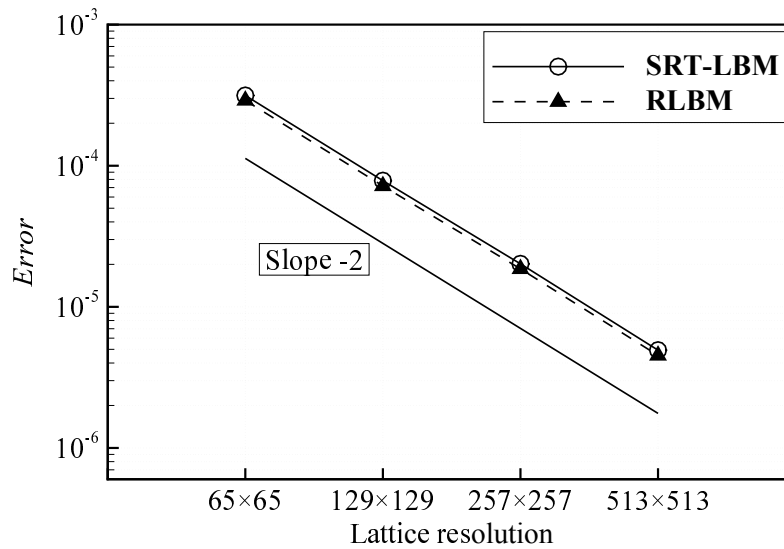


Figure 3.5 – Convergence order of the SRT-LBM and RLBM on the Taylor-Green vortex test-case.

Based on the data listed in Table 3.3, Figure 3.5 shows the convergence order of the SRT-LBM and RLBM. It is observed that both the SRT-LBM and the RLBM exhibit 2<sup>nd</sup>-order convergence, which means that the regularization procedure does not degrade the convergence order of the LBM.

### 3.4 Numerical validation on the lid-driven cavity

In order to further assess the ability of the adopted RLBM, and to validate the theoretical analysis in the previous sections that the regularization procedure filters out the undesired high-order non-equilibrium terms which are surplus for the recovery of the N-S equation and may introduce instability in the calculation, the benchmark test-case of the lid-driven cavity flow is studied.

Figure 3.6 illustrates the basic set-up of the simulation. A square cavity  $L \times L$  is filled with fluid, which is initially set to have zero velocity and a uniform density

$\rho_0$ . The upper lid is moving with a constant horizontal velocity  $U_{\text{lid}}$ . Both the fixed

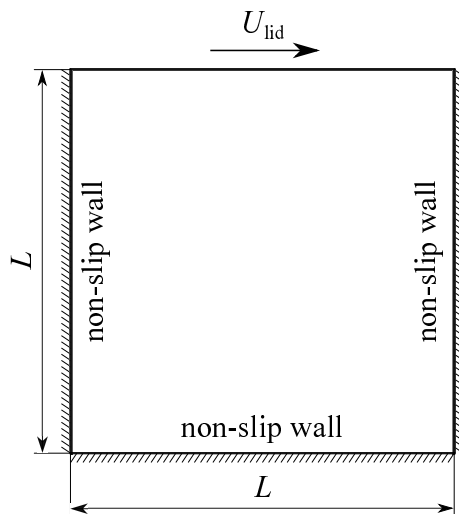


Figure 3.6 – Configuration of the lid-driven cavity flow test-case.

walls and the moving lid have non-slip surfaces. The Reynolds number is defined as

$$Re = \frac{U_{\text{lid}}L}{\nu}, \quad (3.27)$$

where  $\nu$  is the kinetic viscosity.

### 3.4.1 Regularization-based boundary condition

**The equilibrium part** In this calculation, a boundary condition for straight boundaries [102] which reconstructs the distribution functions based on the velocity gradient is adopted. This boundary condition splits the distribution function into an equilibrium part and a non-equilibrium part and treats them separately.

Two macroscopic variables, the density and the velocity, are needed for computing the equilibrium distribution function. The boundary velocities are given by the configuration, i.e.  $(0, 0)$  for the fixed walls and  $(U_{\text{lid}}, 0)$  for the moving lid. The density can be calculated from

$$\rho = \rho_{\text{I}} + \rho_{\text{II}} + \rho_{\text{III}}, \quad (3.28)$$

$$\rho u_{\mathbf{n}} = \rho_{\text{I}} - \rho_{\text{II}}, \quad (3.29)$$

where  $u_{\mathbf{n}}$  is the boundary velocity in the perpendicular direction.  $\rho_{\text{III}}$  is the summation of the distribution functions parallel to the boundary, including  $f_0$ .  $\rho_{\text{I}}$  is the summation of the distribution functions pointing to the exterior of the computation domain, which can be obtained from the streaming process, while  $\rho_{\text{II}}$  is the summation of the distribution functions pointing to the interior of the domain,

which are unknown. The above equations yield

$$\rho = \frac{1}{1 + u_n} (\rho_{\text{III}} + 2\rho_I). \quad (3.30)$$

Taking a node at the lid as an example,

$$\begin{cases} \rho_I = f_2 + f_5 + f_6, \\ \rho_{\text{II}} = f_4 + f_7 + f_8, \\ \rho_{\text{III}} = f_0 + f_1 + f_3, \\ u_n = 0, \end{cases} \quad (3.31)$$

hence the density of the lid node is

$$\rho = f_0 + f_1 + f_3 + 2(f_2 + f_5 + f_6). \quad (3.32)$$

Then the equilibrium distribution function can be computed from the definition in Equation (3.14).

**The non-equilibrium part** Latt et al. [102] proposed to compute the non-equilibrium distribution function  $f_i^{\text{neq}}$  from the velocity gradient, based on the Chapman-Enskog analysis as previously presented in Section 2.5. In the following demonstration, it should be noticed that all the components contributed by the force term that originally contained in the distribution function equal to zero in the lid-driven cavity cases, therefore the terms associated with the force disappear.

From Equations (2.85) and (2.86),  $f_i^{\text{neq}}$  can be expressed as  $f_i^{\text{neq}} \approx \varepsilon f_i^{(1)}$ , where

$$f_i^{(1)} = -\tau \Delta t w_i D_1 \left[ \rho + \frac{\boldsymbol{\xi}_i \cdot \rho \mathbf{u}^*}{c_s^2} + \frac{(\boldsymbol{\xi}_i \boldsymbol{\xi}_i - c_s^2 \mathbf{I}) : \rho \mathbf{u}^* \mathbf{u}^*}{2c_s^4} \right]. \quad (3.33)$$

Noting that the operator  $D_1$  contains two derivatives, for example  $D_1 f_i = \frac{\partial f_i}{\partial t_1} + \boldsymbol{\xi}_i \cdot \frac{\partial f_i}{\partial \mathbf{x}_1}$ , the full expression of the above equation consists of six terms, i.e.

$$\begin{aligned} f_i^{(1)} = -\tau \Delta t w_i \left\{ \frac{\partial \rho}{\partial t_1} + \frac{\boldsymbol{\xi}_i}{c_s^2} \cdot \frac{\partial \rho \mathbf{u}^*}{\partial t_1} + \frac{1}{2c_s^4} (\boldsymbol{\xi}_i \boldsymbol{\xi}_i - c_s^2 \mathbf{I}) : \frac{\partial (\rho \mathbf{u}^* \mathbf{u}^*)}{\partial t_1} \right. \\ \left. + \boldsymbol{\xi}_i \cdot \frac{\partial \rho}{\partial t_1} + \frac{1}{c_s^2} (\boldsymbol{\xi}_i \cdot \nabla_1) (\boldsymbol{\xi}_i \cdot \rho \mathbf{u}^*) + \frac{1}{2c_s^4} (\boldsymbol{\xi}_i \cdot \nabla_1) [(\boldsymbol{\xi}_i \boldsymbol{\xi}_i - c_s^2 \mathbf{I}) : \rho \mathbf{u}^* \mathbf{u}^*] \right\}. \end{aligned} \quad (3.34)$$

Among the six terms in the brace, the term  $\frac{1}{2c_s^4} (\boldsymbol{\xi}_i \boldsymbol{\xi}_i - c_s^2 \mathbf{I}) : \frac{\partial (\rho \mathbf{u}^* \mathbf{u}^*)}{\partial t_1}$  is

simplified as follows. The time derivative term is firstly written as

$$\frac{\partial(\rho \mathbf{u}^* \mathbf{u}^*)}{\partial t_1} = \mathbf{u}^* \frac{\partial(\rho \mathbf{u}^*)}{\partial t_1} + \frac{\partial(\rho \mathbf{u}^*)}{\partial t_1} \mathbf{u}^* - \frac{\partial \rho}{\partial t_1} \mathbf{u}^* \mathbf{u}^*. \quad (3.35)$$

With the help of Equation (2.98), the last term becomes  $-\frac{\partial \rho}{\partial t_1} \mathbf{u}^* \mathbf{u}^* = \nabla_1 \cdot (\rho \mathbf{u}^*) \mathbf{u}^* \mathbf{u}^*$ , which turns out to be a high-order term  $\mathcal{O}(\mathbf{u}^3)$  and can be neglected at low Mach numbers. Bringing Equation (3.35) back, and using the symmetric nature of the tensor  $(\boldsymbol{\xi}_i \boldsymbol{\xi}_i - c_s^2 \mathbf{I})$  yields

$$\frac{1}{2c_s^4} (\boldsymbol{\xi}_i \boldsymbol{\xi}_i - c_s^2 \mathbf{I}) : \frac{\partial(\rho \mathbf{u}^* \mathbf{u}^*)}{\partial t_1} = \frac{1}{c_s^4} (\boldsymbol{\xi}_i \boldsymbol{\xi}_i - c_s^2 \mathbf{I}) : \frac{\partial(\rho \mathbf{u}^*)}{\partial t_1} \mathbf{u}^*. \quad (3.36)$$

Using Equation (2.99) and neglecting the resulting  $\mathcal{O}(\mathbf{u}^3)$  term yields

$$\frac{1}{2c_s^4} (\boldsymbol{\xi}_i \boldsymbol{\xi}_i - c_s^2 \mathbf{I}) : \frac{\partial(\rho \mathbf{u}^* \mathbf{u}^*)}{\partial t_1} = -\frac{1}{c_s^2} (\boldsymbol{\xi}_i \boldsymbol{\xi}_i - c_s^2 \mathbf{I}) : (\nabla_1 \rho) \mathbf{u}^*. \quad (3.37)$$

By inserting Equation (3.37), (2.98) and (2.99) into Equation (3.34),  $f_i^{(1)}$  equals

$$\begin{aligned} f_i^{(1)} = & -\tau \Delta t w_i \left[ \underline{-\nabla_1 \cdot (\rho \mathbf{u}^*)} - \frac{\boldsymbol{\xi}_i \cdot \nabla_1 : \rho \mathbf{u}^* \mathbf{u}^*}{c_s^2} \right] \\ & - \tau \Delta t w_i \left[ \underline{-\boldsymbol{\xi}_i \cdot \nabla_1 \rho} - \frac{(\boldsymbol{\xi}_i \boldsymbol{\xi}_i - c_s^2 \mathbf{I}) : (\nabla_1 \rho) \mathbf{u}^*}{c_s^2} \right] \\ & - \tau \Delta t w_i \left[ \underline{\boldsymbol{\xi}_i \cdot \nabla_1 \rho} + \frac{\boldsymbol{\xi}_i \boldsymbol{\xi}_i : \nabla_1 (\rho \mathbf{u}^*)}{c_s^2} + \frac{1}{2c_s^4} \boldsymbol{\xi}_i \cdot \nabla_1 ((\boldsymbol{\xi}_i \boldsymbol{\xi}_i - c_s^2 \mathbf{I}) : \rho \mathbf{u}^* \mathbf{u}^*) \right], \end{aligned} \quad (3.38)$$

where the underlined terms can be further simplified as

$$\begin{aligned} & -\nabla_1 \cdot (\rho \mathbf{u}^*) - \frac{(\boldsymbol{\xi}_i \boldsymbol{\xi}_i - c_s^2 \mathbf{I}) : (\nabla_1 \rho) \mathbf{u}^*}{c_s^2} + \frac{\boldsymbol{\xi}_i \boldsymbol{\xi}_i : \nabla_1 (\rho \mathbf{u}^*)}{c_s^2} \\ & = \frac{1}{c_s^2} (\boldsymbol{\xi}_i \boldsymbol{\xi}_i - c_s^2 \mathbf{I}) : [\nabla_1 (\rho \mathbf{u}^*) - (\nabla_1 \rho) \mathbf{u}^*] \\ & = \frac{\rho}{c_s^2} (\boldsymbol{\xi}_i \boldsymbol{\xi}_i - c_s^2 \mathbf{I}) : \nabla_1 \mathbf{u}^*. \end{aligned} \quad (3.39)$$

Finally the  $f_i^{(1)}$  is obtained as

$$\begin{aligned} f_i^{(1)} = & -\tau \Delta t w_i \left[ \frac{\rho}{c_s^2} (\boldsymbol{\xi}_i \boldsymbol{\xi}_i - c_s^2 \mathbf{I}) : \nabla_1 \mathbf{u}^* - \frac{\boldsymbol{\xi}_i \cdot \nabla_1 : \rho \mathbf{u}^* \mathbf{u}^*}{c_s^2} \right. \\ & \left. + \frac{1}{2c_s^4} \boldsymbol{\xi}_i \cdot \nabla_1 ((\boldsymbol{\xi}_i \boldsymbol{\xi}_i - c_s^2 \mathbf{I}) : \rho \mathbf{u}^* \mathbf{u}^*) \right] \end{aligned} \quad (3.40)$$

During the evaluation of the moment tensor  $\boldsymbol{\Pi}^{(1)}$ , only the first term contributes,

while the other two vanish. Hence Latt et al. suggest to approximate  $f_i^{(1)}$  as  $f_i^{(1)} = -\frac{\tau \Delta t w_i \rho}{c_s^2} (\boldsymbol{\xi}_i \boldsymbol{\xi}_i - c_s^2 \mathbf{I}) : \nabla_1 \mathbf{u}^*$ .

To validate this,  $\boldsymbol{\Pi}^{(1)}$  is checked.

$$\begin{aligned} \boldsymbol{\Pi}^{(1)} &= \sum_i (\mathbf{Q} + c_s^2 \mathbf{I}) f_i^{(1)} = \sum_i \mathbf{Q} f_i^{(1)} \\ &= -\frac{\tau \Delta t \rho}{c_s^2} \sum_i w_i \mathbf{Q} \mathbf{Q} : (\nabla_1 \mathbf{u}^*) \end{aligned} \quad (3.41)$$

where  $\mathbf{Q}$  is the abbreviation for  $\mathbf{Q} = \boldsymbol{\xi}_i \boldsymbol{\xi}_i - c_s^2 \mathbf{I}$ . Based on the property of the lattice basis as presented in Equation (2.60),  $\boldsymbol{\Pi}^{(1)}$  becomes

$$\boldsymbol{\Pi}^{(1)} = -\tau \Delta t \rho c_s^2 \left[ \nabla_1 \mathbf{u}^* + (\nabla_1 \mathbf{u}^*)^T \right], \quad (3.42)$$

which is identical to the original one in Equation (2.117). As the moment tensor  $\boldsymbol{\Pi}^{(1)}$  has remained the same, the suggested approximation is proved to be reasonable. Thus, the non-equilibrium distribution function is obtained as

$$f_i^{\text{neq}} \approx \varepsilon f_i^{(1)} = -\frac{\rho \tau \Delta t w_i}{c_s^2} (\boldsymbol{\xi}_i \boldsymbol{\xi}_i - c_s^2 \mathbf{I}) : \nabla \mathbf{u}^*. \quad (3.43)$$

**A regularization explanation of the boundary condition** Such evolution of the non-equilibrium distribution function substitute introduced in [102] is delicate and complex. Alternatively, following the regularization idea presented in Section 3.1.2, the same substitute can be obtained straightforwardly and succinctly. Without obstructing the recovery of the N-S equation, the non-equilibrium distribution function can be replaced by a substitute obtained from a regularization procedure up to the 2<sup>nd</sup>-order, as shown in Equation (3.17). For an explicit force model as used in [102], or a system without external forces as in this case, the first several Hermite expansion coefficients of  $f_i^{\text{neq}}$  are

$$\left\{ \begin{array}{l} a_{\text{neq}}^{(0)} = \varepsilon \sum_i f_i^{(1)} = 0, \\ \mathbf{a}_{\text{neq}}^{(1)} = \frac{\varepsilon}{c_s} \sum_i \boldsymbol{\xi}_i f_i^{(1)} = \mathbf{0}, \\ \mathbf{a}_{\text{neq}}^{(2)} = \frac{\varepsilon^2}{c_s^2} \boldsymbol{\Pi}^{(1)} - \mathbf{I} \varepsilon \sum_i f_i^{(1)} = \tau \Delta t \rho \left[ \nabla \mathbf{u}^* + (\nabla \mathbf{u}^*)^T \right]. \end{array} \right. \quad (3.44)$$

Hence the regularized non-equilibrium distribution function is computed as

$$\begin{aligned}
 f_i^{\text{neq}} &= w_i \left[ a_{\text{neq}}^{(0)} \mathcal{H}^{(0)} + \mathbf{a}_{\text{neq}}^{(1)} \cdot \mathcal{H}^{(1)} + \frac{1}{2} \mathbf{a}_{\text{neq}}^{(2)} : \mathcal{H}^{(2)} \right] \\
 &= \frac{\tau \Delta t \rho w_i}{2} \left[ \nabla \mathbf{u}^* + (\nabla \mathbf{u}^*)^T \right] : \mathcal{H}^{(2)} \\
 &= \frac{\tau \Delta t \rho w_i}{c_s^2} (\boldsymbol{\xi}_i \boldsymbol{\xi}_i - c_s^2 \mathbf{I}) : \nabla \mathbf{u}^*,
 \end{aligned} \tag{3.45}$$

where the last step is obtained from the symmetry of the tensor  $\mathcal{H}^{(2)}$ . The expression (3.45) is coincident with Equation (3.43), which additionally explains that this boundary treatment (I) takes into account the viscous effect, since the viscous term in the N-S equation is completely contributed from the term  $\mathbf{\Pi}^{(1)}$ , as can be seen in the Chapman-Enskog analysis in Section 2.5; (II) constructs the non-equilibrium distribution function on the  $\mathbb{H}^2$  space, and makes it more coherent with the RLBM scheme compared with the alternatively adoptable Zou-He boundary condition (see Section 2.6.3).

### 3.4.2 Numerical results

The numerical results at a Reynolds number of  $Re = 1000$  are obtained by the RLBM with lattice resolutions of  $65 \times 65$ ,  $129 \times 129$ ,  $257 \times 257$  and  $513 \times 513$ . For the four lattice resolutions, the dimensionless relaxation time is kept at  $\tau = 0.506$ . Some necessary parameters are listed in Table 3.4.

Table 3.4 – Some necessary parameters for the lid-driven cavity flow test-case.

Lattice resolution	$C_x$	$C_t$	$\tau$	$Re$	$Ma$
$65 \times 65$	$1.00 \times 10^0$	$1.0000 \times 10^0$	0.506	1000	$5.413 \times 10^{-2}$
$129 \times 129$	$5.00 \times 10^{-1}$	$2.5000 \times 10^{-1}$	0.506	1000	$2.706 \times 10^{-2}$
$257 \times 257$	$2.50 \times 10^{-1}$	$6.2500 \times 10^{-2}$	0.506	1000	$1.353 \times 10^{-2}$
$513 \times 513$	$1.25 \times 10^{-1}$	$1.5625 \times 10^{-2}$	0.506	1000	$6.766 \times 10^{-3}$

Besides, the results obtained by the widely used multi-relaxation-time (MRT) LBM are used for comparison. The MRT collision model [99] is a widely known collision model, which projects the distribution functions onto a moment space by a transformation matrix, and enforces the collision model on the resulting moments with different artificial relaxation times. The readers can refer to Appendix B for more details of the implementation of the MRT-LBM. The calculation parameters for the MRT-LBM are of the same values as listed in Table 3.4.

It is important to note here that the MRT collision model is actually a precursor to the SRT collision model, as reviewed in Section 1.2.1. The LBM is originally developed with an MRT collision model, before SRT collision model became more popular due to its great simplicity. However, since the SRT-LBM has numerical instability problems in some situations, the MRT-LBM came back to the stage, because it allows one to freely choose relaxation rates for different modes of distribution functions and thus offers a possibility to reduce non-hydrodynamic noises. Such freedom of freely choosing relaxation parameters makes MRT-LBM a more general form of LBM scheme. To give an example, it is well known that when all the nine relaxation parameters for D2Q9 lattice are fixed at  $1/\tau$ , where this  $\tau$  is related to the fluid viscosity, the MRT-LBM degenerates to the SRT-LBM [99]. It is also pointed out in [56] that when the free relaxation parameters, i.e. the parameters other than those for conserved modes or viscous modes, are chosen to be  $-1$ , the MRT-LBM is coincident with the regularized LBM.

To be frank, the rule for optimizing the multiple relaxation parameters is not very clear to us. Throughout the thesis, we chose to use the parameter set in [55, 123] for the MRT-LBM calculations, and we refer to this *ad hoc* configuration of MRT-LBM when we analyze numerical results.

### Velocity profiles along the centerlines

Botella and Peyret [18] provide a solution to the benchmark using the high-order spectral (HOS) method, which is a more accurate result than the classic reference by Ghia et al. [47]. In this section, the present results are compared with the results from [18]. To give a visual impression, the horizontal velocity profile on the vertical centerline and the vertical velocity profile on the horizontal centerline are shown in Figure 3.7. The presented results are obtained with a  $257 \times 257$  lattice. One can observe that the present results agree very well with the reference.

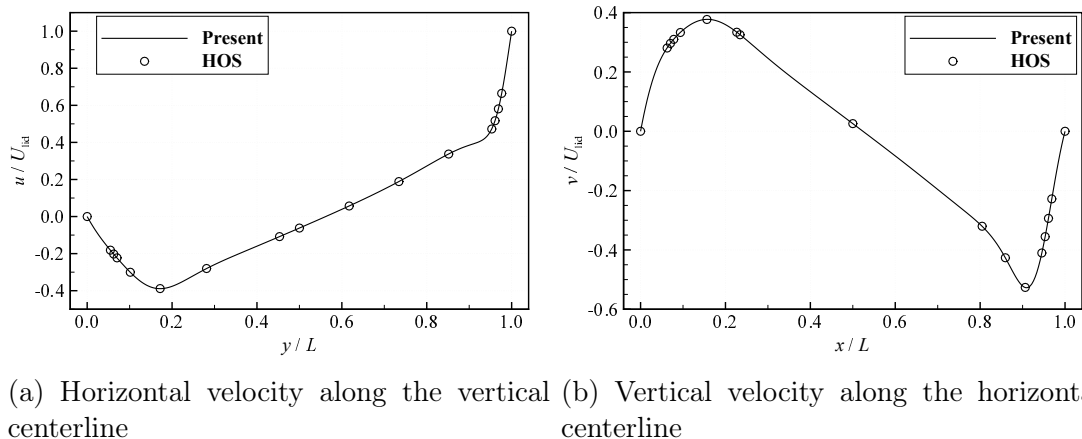


Figure 3.7 – Velocity components along the centerlines of the cavity at  $Re = 1000$ , obtained by the RLBM with a  $257 \times 257$  lattice.

### Accuracy and efficiency

Table 3.5 and 3.6 provide the data obtained with the  $257 \times 257$  lattice, and they also include the results obtained by the standard SRT-LBM and the MRT-LBM. The  $L^2$ -error of the velocity components is computed, with respect to the benchmark results from [18]. For example the  $L^2$ -error of the listed horizontal velocity components is

$$Error = \frac{\sqrt{\sum (u - u_{\text{Ref}})^2}}{\sqrt{\sum u_{\text{Ref}}^2}}. \quad (3.46)$$

From the comparison in Table 3.5 and 3.6, it can be clearly observed that the RLBM results are the closest to the reference data at nearly all the given positions, among the three schemes.

Table 3.5 – Horizontal velocity components obtained by RLBM, SRT-LBM, and MRT-LBM schemes at the positions given in [18] and their relative errors *Error*. The lattice resolution is  $257 \times 257$ .

$y/L$	$u_{\text{Ref}}/U_{\text{lid}}$	$u_{\text{RSRT}}/U_{\text{lid}}$	$u_{\text{SRT}}/U_{\text{lid}}$	$u_{\text{MRT}}/U_{\text{lid}}$
0.0000	0.0000000	0.0000000	0.0000000	0.0000000
0.0547	-0.1812881	-0.1815121	-0.1820047	-0.1795431
0.0625	-0.2023300	-0.2026170	-0.2031464	-0.2006022
0.0703	-0.2228955	-0.2232416	-0.2238035	-0.2210958
0.1016	-0.3004561	-0.3007684	-0.3010249	-0.2983061
0.1719	-0.3885691	-0.3889747	-0.3893449	-0.3871512
0.2813	-0.2803696	-0.2805875	-0.2805801	-0.2798501
0.4531	-0.1081999	-0.1082245	-0.1081470	-0.1079095
0.5000	-0.0620561	-0.0620681	-0.0620034	-0.0619087
0.6172	0.0570178	0.0570890	0.0571987	0.05684200
0.7344	0.1886747	0.1888557	0.1889682	0.1881098
0.8516	0.3372212	0.3375879	0.3378672	0.3359855
0.9531	0.4723329	0.4728675	0.4732317	0.4694680
0.9609	0.5169277	0.5176146	0.5179538	0.5139478
0.9688	0.5808359	0.5807513	0.5810100	0.5769885
0.9766	0.6644227	0.6641956	0.6644091	0.6607027
1.0000	1.0000000	1.0000000	1.0000000	1.0000000
<i>Error</i> (%)	–	0.0733860	0.1440734	0.4695529

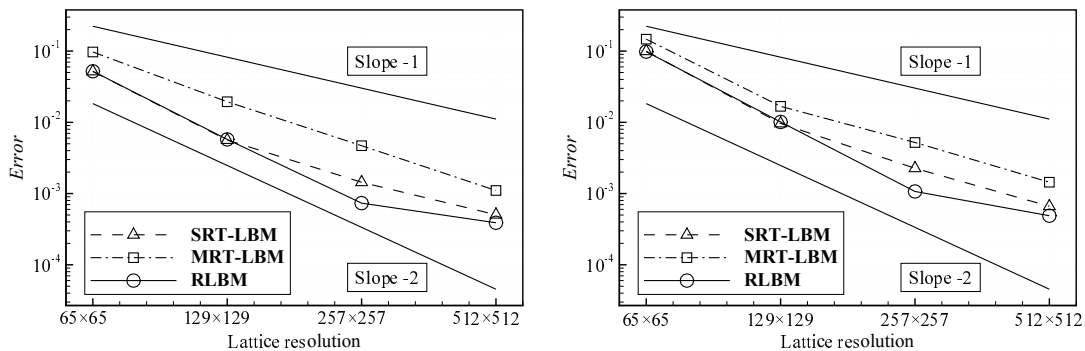
Table 3.6 – Vertical velocity components obtained by RLBM, SRT-LBM, and MRT-LBM schemes at the positions given in [18] and their relative errors *Error*. The lattice resolution is  $257 \times 257$ .

$x/L$	$v_{\text{Ref}}/U_{\text{lid}}$	$v_{\text{RSRT}}/U_{\text{lid}}$	$v_{\text{SRT}}/U_{\text{lid}}$	$v_{\text{MRT}}/U_{\text{lid}}$
0.0000	0.0000000	0.0000000	0.0000000	0.0000000
0.0625	0.2807056	0.2811274	0.2814148	0.2791190
0.0703	0.2962703	0.2967280	0.2971174	0.2946330
0.0781	0.3099097	0.3103925	0.3107283	0.3082328
0.0938	0.3330442	0.3334273	0.3338186	0.3311815
0.1563	0.3769189	0.3773262	0.3776694	0.3752602
0.2266	0.3339924	0.3342824	0.3344441	0.3329850
0.2344	0.3253592	0.3256191	0.3258275	0.3243955
0.5000	-0.0257995	-0.0257725	-0.0257910	-0.0257658
0.8047	-0.3202137	-0.3203897	-0.3205207	-0.3192220
0.8594	-0.4264545	-0.4267146	-0.4268297	-0.4256038
0.9063	-0.5264392	-0.5269581	-0.5275407	-0.5247051
0.9453	-0.4103754	-0.4106261	-0.4115131	-0.4076321
0.9531	-0.3553213	-0.3554337	-0.3561798	-0.3525346
0.9609	-0.2936869	-0.2736557	-0.2943594	-0.2909414
0.9688	-0.2279225	-0.2285921	-0.2291229	-0.2261418
1.0000	0.0000000	0.0000000	0.0000000	0.0000000
<i>Error</i> (%)	–	0.1070014	0.2263028	0.5209056

Moreover, the numerical errors of the 12 cases, i.e. with the three numerical schemes in the four lattice resolutions, are listed in Table 3.7, and Figure 3.8 is drawn based on the relative errors. From these error slopes, one can observe an

Table 3.7 –  $L^2$ -error of the velocity components on the centerlines, with the SRT-LBM, MRT-LBM and RLBM schemes, and their consumed CPU times. The listed CPU times are relative values compared with that of the  $65 \times 65$  SRT-LBM case.

Numerical scheme	Lattice resolution	$Error_u$	$Error_v$	$t^{CPU}$
SRT-LBM	$65 \times 65$	5.1765	9.9370	1.00
	$129 \times 129$	0.5637	0.9638	14.08
	$257 \times 257$	0.1441	0.2263	199.49
	$513 \times 513$	0.0505	0.0663	3008.21
MRT-LBM	$65 \times 65$	9.7068	14.6869	1.07
	$129 \times 129$	1.9448	1.6764	16.11
	$257 \times 257$	0.4696	0.5209	225.28
	$513 \times 513$	0.1103	0.1443	3456.85
RLBM	$65 \times 65$	5.2084	9.8242	1.27
	$129 \times 129$	0.5753	1.0117	18.93
	$209 \times 209$	0.1843	0.1979	199.46
	$257 \times 257$	0.0734	0.1070	266.12
	$513 \times 513$	0.0389	0.0487	4077.48



(a)  $L^2$ -error of the horizontal velocity components along the vertical centerline (b)  $L^2$ -error of the vertical velocity components along the horizontal centerline

Figure 3.8 –  $L^2$ -error of the velocity components along the centerlines. The results are obtained by the SRT-LBM, MRT-LBM and RLBM schemes.

overall convergence between 1<sup>st</sup>-order and 2<sup>nd</sup>-order for the three schemes. The convergence speed has a decay when the lattice resolution gets larger, which may be due to the existence of the difference between the converged LBM results and the HOS result, since the relative error is already of less than 1% for the RLBM

between the two. Considering the numerical errors of the velocity components, the SRT-LBM and the RLBM show a better accuracy than the MRT-LBM with the same lattice resolution, and the RLBM is slightly more accurate than the SRT-LBM. The consistency of the adopted boundary condition and the RLBM may contribute to this advantage.

It is more practically meaningful to consider the CPU time to accuracy ratio when discussing numerical accuracy. In Table 3.7, the listed CPU times are relative values compared with that for the  $65 \times 65$  SRT-LBM case. The CPU times in Table 3.7 indicate that the RLBM is more time-consuming than the other two schemes. However, if we compare the RLBM results with a  $209 \times 209$  lattice, which cost almost the same CPU time for one time-step than the  $257 \times 257$  SRT-LBM, the two schemes show an equivalent accuracy, thus a comparable CPU time to accuracy ratio. In this context, the relatively larger time demanding nature of the RLBM is acceptable, and it offers better accuracy with the same lattice resolution.

### Pressure field

As pointed out in Section 3.1.2, the RLBM is thought to be numerically more stable than the original SRT-LBM, as it filters out the undesired high-order non-equilibrium modes. In the lid-driven cavity flow test-case, the discontinuous velocity at the upper corners makes it difficult to predict the flow field in their neighborhood. Figure 3.9 shows the pressure fields obtained with the SRT-LBM, MRT-LBM and RLBM with four different lattice resolutions. In the SRT-LBM results, one can clearly observe some chessboard-liked pressure fluctuations introduced from the singularity at the upper corners. With the lattice resolution augmenting, this fluctuation weakens in terms of magnitude, but is still visible. As for the MRT-LBM and RLBM, the pressure fields are much smoother. The RLBM succeeds in filtering out the pressure fluctuations, as expected. The MRT-LBM is indeed helpful in stabilizing the pressure field, but considering the efficiency analysis in the previous section, the RLBM scheme seems more suitable for this test-case.

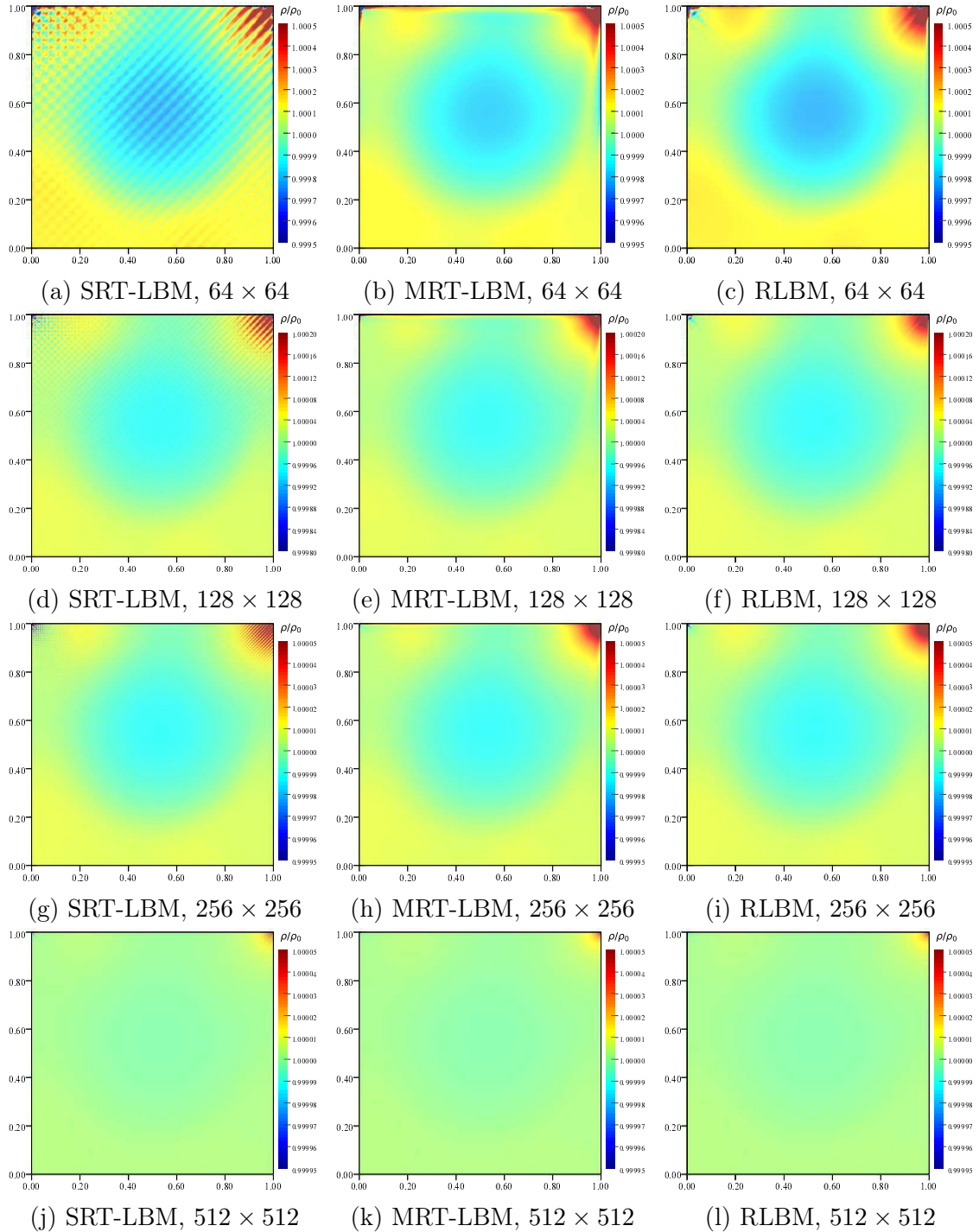


Figure 3.9 – Pressure fields of the SRT-LBM, MRT-LBM and RLBM results.

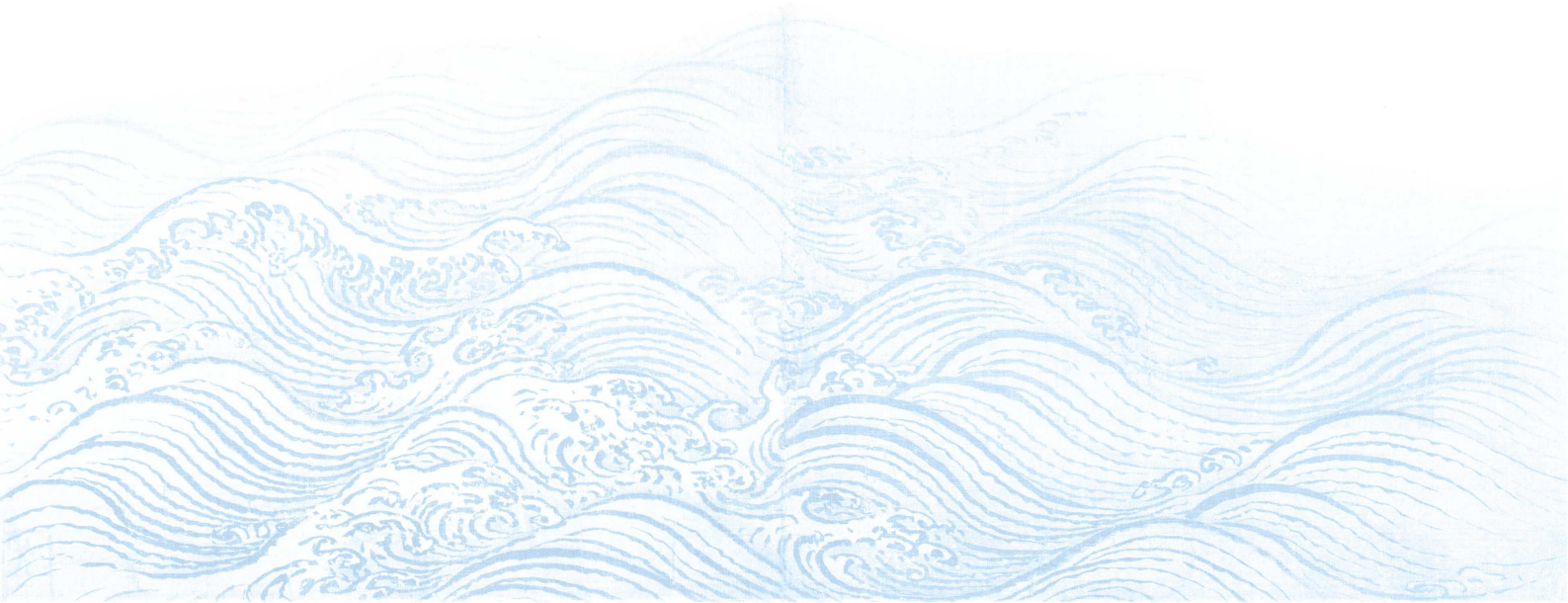


# Chapter 4

## Free-surface model

Following the original idea in [94], the adopted single-phase free-surface model is elaborated thoroughly in this chapter, including the free-surface representation, the flag evolution, the mass conservation and the treatment of boundary condition. By implementing the free-surface model in the RLBM, two validation test-cases are carried out, i.e. the viscous standing wave and the dambreak flow. In the last part, the free-surface model is modified to provide a countermeasure against the dilemma of the original model in certain situations. The new model is validated in the dambreak test-case.

Le modèle de surface libre monophasé adopté est détaillé dans ce chapitre suivant l'idée originale dans [94], en termes de représentation de la surface libre, d'évolution de la fonction indicatrice, de conservation de la masse et de traitement des conditions aux limites. Deux cas tests, la vague visqueuse stationnaire et un écoulement de dambreak, sont étudiés pour valider ce modèle de surface libre dans la RLBM. Dans la dernière partie, le modèle de surface libre est modifié pour traiter le dilemme du modèle original dans certaines situations. Le nouveau modèle est validé sur le cas test du dambreak.



## Contents

---

<b>4.1</b>	<b>Free-surface representation</b>	<b>79</b>
<b>4.2</b>	<b>Flag evolution</b>	<b>80</b>
<b>4.3</b>	<b>Mass conservation</b>	<b>82</b>
4.3.1	Mass evolution during the streaming process	83
4.3.2	Mass evolution due to the flag change	84
<b>4.4</b>	<b>Reconstruction of the distribution functions at the free-surface</b>	<b>86</b>
<b>4.5</b>	<b>Algorithm</b>	<b>88</b>
<b>4.6</b>	<b>Validations</b>	<b>89</b>
4.6.1	Viscous standing wave	89
4.6.2	Dambreak flow	93
<b>4.7</b>	<b>An improved free-surface LB model</b>	<b>103</b>
4.7.1	Dilemmas of the original free-surface LB model	103
4.7.2	A new distribution method for the distribution functions at the free-surface	104
4.7.3	Algorithm	106
4.7.4	Validation	106

---

## 4.1 Free-surface representation

The adopted single-phase free-surface model uses a volume-of-fluid (VOF) approach to represent the free-surface. Figure 4.1 shows the mesh generation for a free-surface flow case. A background mesh is projected on the computation do-

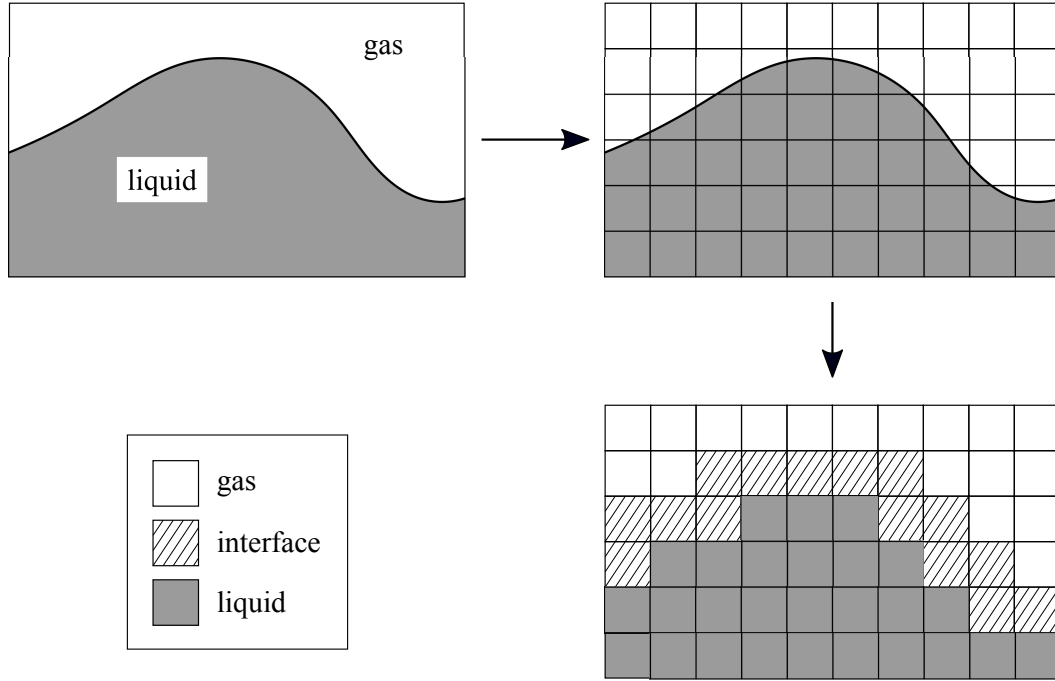


Figure 4.1 – Mesh generation for free-surface flows

main. The cells, where the free-surface profile passes, are called interface cells. The rest of the discretized cells which contain only the liquid or the gas are respectively liquid cells and gas cells. These three categories of cells are characterized by the volume fraction  $\alpha$ , which indicates the volume proportion of the liquid component in one unit control volume. The volume fraction value can vary from 0 to 1, where  $\alpha = 1$  for liquid cells,  $0 < \alpha < 1$  for interface cells, and  $\alpha = 0$  for gas cells. Based on the volume fraction, the mass of the liquid component within an individual cell can be computed as

$$M = \alpha \rho V_0, \quad (4.1)$$

where  $\rho$  is the liquid density, and  $V_0$  is the fixed cell volume which can be set as unit. It is very important to point out that there should be always a layer of interface cells lying between the liquid cells and the gas cells, i.e. the direct attachment of a fluid cell and a gas cell is forbidden.

The Cartesian nature of the background mesh coincides with the requirement of the lattice representation of the LBM. Here, a cell-centered lattice is adopted, where the lattice nodes are located in the center of the cells. In addition to the distribution functions, the cell information, i.e. the cell flag, the volume fraction

and the cell mass, are also stored in the lattice nodes.

## 4.2 Flag evolution

The fluid flow causes mass fluxes between the lattice cells. As a result, the volume fraction changes at every time step, and the cell flag may have to change accordingly. Thus, the criterion for the volume fraction that will trigger flag changes should be built up. In this model, two types of transformation are defined. If an interface cell gets enough mass during one time-step  $\Delta t$  and its resulting volume fraction temporarily passes 1, then this cell will be reinitialized as a liquid cell at the new time-step. For simplicity, we call this cell a filled interface cell. Figure 4.2 shows this transformation. One may notice that this flag change leads to a direct contact of a liquid cell and a gas cell, which should be avoided. Hence the neighboring gas cells will turn into interface cells to guarantee a continuous interface layer. Similarly, the other transformation procedure is shown in Figure 4.3. If the

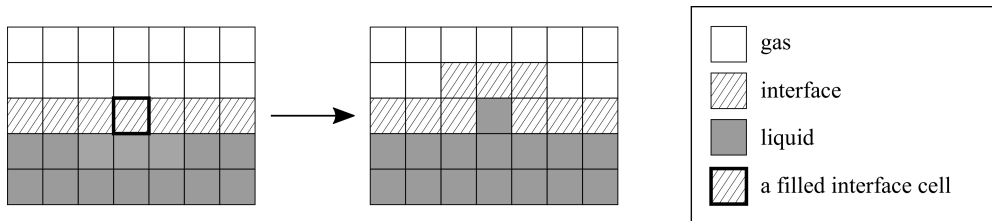


Figure 4.2 – When an interface cell turns into a liquid cell, its neighboring gas cells will become interface cells

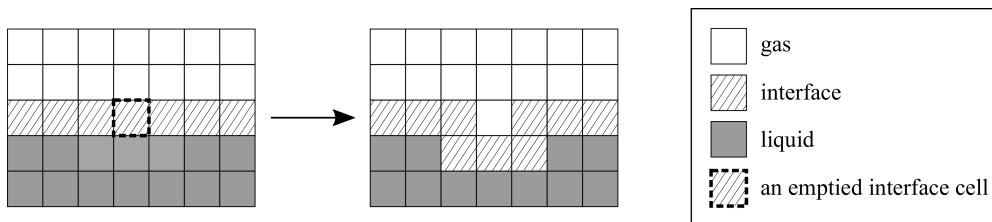


Figure 4.3 – When an interface cell turns into a gas cell, its neighboring liquid cells will become interface cells

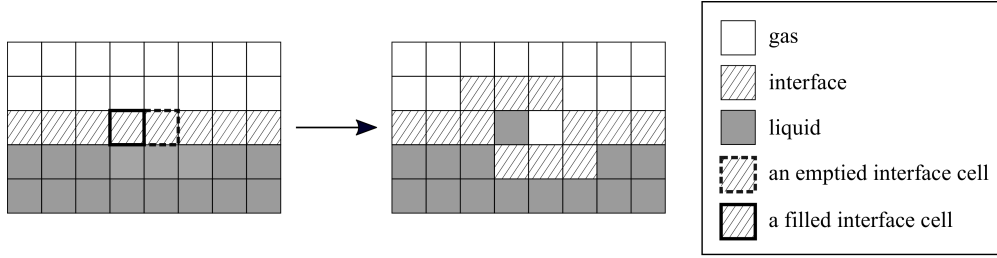
volume fraction of an interface cell temporarily drops down to 0 due to negative mass flux, this cell, which is named an emptied interface cell here, will become a gas cell. As an accompanying reactivity, its neighboring liquid cells will turn into interface cells.

The mentioned criteria for the two types of flag change, namely  $\alpha > 1$  for filled interface cells and  $\alpha < 0$  for emptied interface cells, are a little bit extreme, because cells that marginally satisfy these conditions will trigger flag changes in itself and its neighbors, and also the accompanying mass exchanges. Based on this

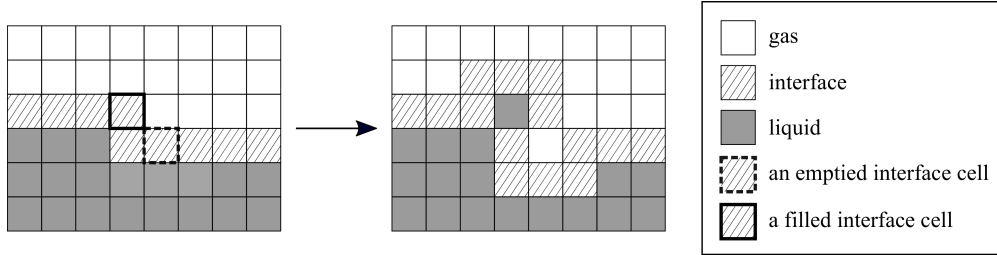
consideration, a small margin is added in this study, which means an interface cell with a volume fraction  $\alpha > 1 + \beta$  is identified as a filled interface cell, and with  $\alpha < -\beta$  as an emptied cell. The small positive value  $\beta$  is set to be  $\beta = 0.001$  in the simulations presented in this thesis.

Apart from these basic rules of interface movement, we shall also highlight four key points that should be carefully treated.

- (I) Firstly, all the flag changes during one time-step must be completed simultaneously. Due to the sequence nature of code implementation, the interface cells are treated one by one. If the flag change is a real-time process, the final state of the flag array after one time step will be highly depending on the treating order. In order to avoid this uncertainty, when determining which cell should change its flag at time  $t$ , the searching process must be based on the same flag array of time  $t$ . The cells who will experience a flag change are recorded in a waiting-to-change list, and their flags are changed at the same time, after all the cells are examined.
- (II) Secondly, filled interface cells and emptied interface cells cannot be adjoining, see Figure 4.4. A filled interface cell and an adjacent emptied interface cell will lead to an interrupted free-surface profile and a direct contact between a liquid cell and a gas cell, which disobeys the basic rules of free-surface representation as aforementioned in Section 4.1. This phenomenon is not expected to occur, because it indicates a too violent mass flux, but it may happen numerically in practice. Although this problem might be solved if a refined lattice or a smaller time step is adopted, we still desire a robust numerical model that won't be interrupted by this accidental error. In this context, a compromising solution is provided here, that the flag change is operated to only one cell between the two adjacent filled and emptied interface cells. The criterion is based on the volume fractions of the two involved cells. If the volume fraction of the filled interface cell is relatively farther from 0.5 than that of the emptied interface cell, the flag change is imposed to the filled interface cell, while the emptied cell remains unchanged as an interface cell, and vice versa.
- (III) Thirdly, if isolated interface cells are found inside the liquid or gas domain, they are forced to turn into a liquid or a gas cell, respectively.
- (IV) Lastly, the newly formed interface cells due to the flag change in their filled interface cell neighbors need to be reinitialized. Their density and velocity



(a) A filled interface cell and an emptied interface cell are neighbours in the  $x$ - or the  $y$ -direction.



(b) A filled interface cell and an emptied interface cell are neighbors in the diagonal direction.

Figure 4.4 – If a filled interface cell and an emptied interface cell are neighbors, the resulting free-surface profile will be discontinuous, and a direct contact of liquid cells and gas cells may occur, which should be prevented.

are interpolated from the surrounding liquid and interface cells as

$$\left\{ \begin{array}{l} \rho(\mathbf{x}, t) = \frac{\sum_i \rho(\mathbf{x} + \boldsymbol{\xi}_i \Delta t, t)}{\sum_i 1}, \forall flag(\mathbf{x} + \boldsymbol{\xi}_i \Delta t, t) \neq \text{gas}, \\ \mathbf{u}(\mathbf{x}, t) = \frac{\sum_i \mathbf{u}(\mathbf{x} + \boldsymbol{\xi}_i \Delta t, t)}{\sum_i 1}, \forall flag(\mathbf{x} + \boldsymbol{\xi}_i \Delta t, t) \neq \text{gas}. \end{array} \right. \quad (4.2)$$

Then the distribution function is initialized with the equilibrium distribution function calculated from interpolated macroscopic parameters in Equation (4.2).

### 4.3 Mass conservation

The mass conservation is very important for the adopted free-surface model, because frequent cell reinitializations are carried out during the calculation, which are accompanied with complex mass exchange with surrounding cells. The cell mass is adapted two times in one time-step. The first one is a global operation for all the lattice cells which takes place during the streaming process, while the second one is a regional manipulation after the flag change, which is imposed to the cells that are involved in the flag change. In the present model, the mass evolution

method is developed in a way that the total mass of the fluid system is conserved by definition, which can be concluded from the following analysis.

### 4.3.1 Mass evolution during the streaming process

The definition (2.69) indicates that the distribution function  $f_i(\mathbf{x}, t)$  represents a proportion of fluid at position  $\mathbf{x}$  that propagates in the  $i$  direction. Hence the streaming process of the distribution functions brings mass advection between lattice cells. In the present model, the mass of one cell is modified from its value at time  $t$  by adding the temporal summation of the mass increment in all the lattice directions, which can be expressed as

$$M(\mathbf{x}, t + \Delta t) = M(\mathbf{x}, t) + \sum_i \Delta M_i(\mathbf{x}, t). \quad (4.3)$$

$\Delta M_i$  is the net mass increment in direction  $i$ , which is computed as

$$\Delta M_i(\mathbf{x}, t) = C_i [f_{\bar{i}}^{\text{pc}}(\mathbf{x} + \boldsymbol{\xi}_i \Delta t, t) - f_i^{\text{pc}}(\mathbf{x}, t)], \quad (4.4)$$

where  $\bar{i}$  indicates the opposite direction of  $i$ , and  $C_i$  is a coefficient related to the cell flags and the volume fractions of the cells at  $\mathbf{x}$  and  $\mathbf{x} + \boldsymbol{\xi}_i \Delta t$ . The value of the coefficient  $C_i$  is given in Table 4.1.

Table 4.1 – Value of the coefficient  $C_i$  in the mass evolution equation (4.3).

$flag(\mathbf{x})$	$flag(\mathbf{x} + \boldsymbol{\xi}_i \Delta t)$	$C_i$
gas	gas	0
	interface	0
interface	gas	0
	interface	$\frac{1}{2} [\alpha(\mathbf{x}) + \alpha(\mathbf{x} + \boldsymbol{\xi}_i \Delta t)]$
	liquid	1
liquid	interface	1
	liquid	1

The coefficient  $C_i$  is assigned based on three considerations.

- (I) Since the gas is not considered in this model, the coefficient  $C_i$  is zero for any gas cell and its neighbors.
- (II) Concerning the mass exchange between two interface cells, the coefficient is set to be  $C_i = \frac{1}{2} [\alpha(\mathbf{x}) + \alpha(\mathbf{x} + \boldsymbol{\xi}_i \Delta t)]$ . This is designed in a way that

the mass fluxes across the cell interface from both sides are balanced, where the local volume fraction at the cell interface is interpolated from a linear approximation, as shown in Figure 4.5.

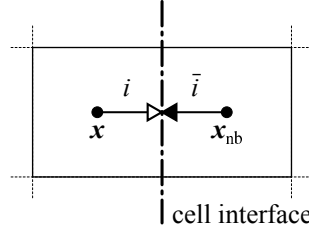


Figure 4.5 – Mass exchange between two adjacent interface cells. The mass fluxes across the cell interface are balanced.

- (III) If a liquid cell is associated in the mass exchange, the coefficient  $C_i$  should always equals 1 due to the constraint of  $\alpha = 1$  in the liquid domain. It is argued [94] that such assignment is reasonable since the interface of a liquid cell and an interface cell is also fully occupied by liquid.

By selecting the coefficient  $C_i$  as mentioned above, Equation (4.4) satisfies a kind of symmetry from a global viewpoint, because for two adjacent cells, the amount of mass loss in one cell is always equal to the mass gained in others. In this way, the total mass of the system is conserved by construction.

### 4.3.2 Mass evolution due to the flag change

The mass change also takes place when the cell flag changes. Figure 4.6 shows an example of a filled interface cell. The volume fraction of a filled interface cell is

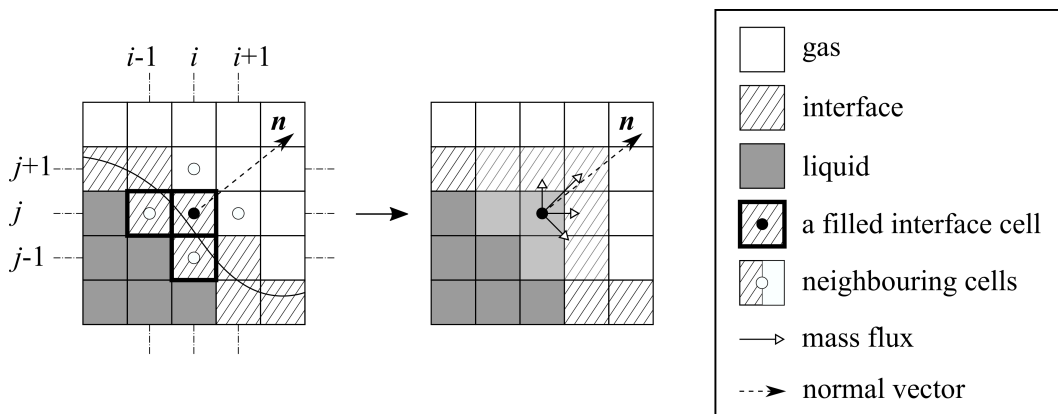


Figure 4.6 – When a filled interface cell at position  $\mathbf{x}$  turns into a liquid cell, the excess cell mass is distributed to the neighboring interface cells at position  $\mathbf{x} + \boldsymbol{\xi}_i \Delta t$  that satisfy  $\mathbf{n} \cdot \boldsymbol{\xi}_i > 0$ . The distribution is based on a weighting coefficient related to the interface normal vector  $\mathbf{n}$ .

originally such that  $\alpha > 1 + \beta$  before the flag change, while it is fixed at 1 in the newly formed liquid cell after the flag change. Hence a sudden drop in the cell mass appears, i.e.  $\Delta M_{\text{ex}} = (\alpha - 1) \rho V_0$ , where  $\Delta M_{\text{ex}}$  denotes the excess mass that is distributed to the neighboring interface cells for the sake of mass conservation.

In the present model, the distribution is based on a weighting function associated with the normal vector at the interface, which leads the excess mass to be transferred in the interface motion direction. It is important to note here that by saying *in the interface motion direction*, we mean the trend of distributing larger percentage of the excess mass along the normal vector direction, since the normal vector as being calculated in the following formula is not exactly the real interface motion direction, i.e.

$$\mathbf{n}(i, j) = \frac{\nabla \alpha}{\|\nabla \alpha\|}, \quad (4.5)$$

where

$$\nabla \alpha \approx \left( \frac{\alpha(i+1, j) - \alpha(i-1, j)}{2\Delta x}, \frac{\alpha(i, j+1) - \alpha(i, j-1)}{2\Delta x} \right). \quad (4.6)$$

Marking the position of the filled interface cell as  $\mathbf{x}$ , the interface cell at position  $\mathbf{x} + \boldsymbol{\xi}_i \Delta t$  and time  $t + \Delta t$  will receive a cell mass of

$$\Delta M_{\text{receive}}(\mathbf{x} + \boldsymbol{\xi}_i \Delta t) = \frac{w_i^M}{\sum_i \omega_i} \Delta M_{\text{ex}}(\mathbf{x}), \quad (4.7)$$

where the weighting coefficient  $w_i^M$  is calculated as

$$w_i^M = \begin{cases} \mathbf{n} \cdot \boldsymbol{\xi}_i \forall \mathbf{n} \cdot \boldsymbol{\xi}_i > 0, \\ 0 \forall \mathbf{n} \cdot \boldsymbol{\xi}_i \leq 0. \end{cases} \quad (4.8)$$

Similarly, for emptied interface cells, the excess mass is  $\Delta M_{\text{ex}} = -\alpha \rho V_0$ , and the weighting coefficient for distributing the excess mass is computed as

$$w_i^M = \begin{cases} -\mathbf{n} \cdot \boldsymbol{\xi}_i \forall \mathbf{n} \cdot \boldsymbol{\xi}_i < 0, \\ 0 \forall \mathbf{n} \cdot \boldsymbol{\xi}_i \geq 0. \end{cases} \quad (4.9)$$

These distributions of excess cell mass are both designed to ensure a perfect balance of the cell mass loss and the cell mass gain.

In addition, if single isolated interface cells exist as described in the (III) situation in Section 4.2, the excess mass due to the enforced flag change in the isolated cells are equally distributed to all the interface cells.

$$\Delta M_{\text{receive}} = \frac{\Delta M_{\text{ex}}}{N_{\text{I}}}, \quad (4.10)$$

where  $N_I$  is the number of interface cells, and  $\Delta M_{\text{ex}} = \rho(\alpha - 1)V_0$  for the isolated cells in the liquid domain, and  $\Delta M_{\text{ex}} = \rho\alpha V_0$  for the isolated cells in the gas domain.

## 4.4 Reconstruction of the distribution functions at the free-surface

As the gas motion is not considered, the distribution functions at the free-surface that ought to be streamed from the gas side are missing. The present model reconstructs the missing distribution functions based on the dynamic free-surface boundary condition that the gas pressure imposed on the interface is balanced by the hydrodynamic force from the liquid domain.

The reconstruction procedure [94] is given as

$$f_i^{\text{pc}}(\mathbf{x} - \boldsymbol{\xi}_i \Delta t, t) = f_i^{\text{eq}} + f_{\bar{i}}^{\text{eq}} - f_{\bar{i}}^{\text{pc}}(\mathbf{x}, t), \quad (4.11)$$

where the subscript  $i$  indicates a direction pointing to an interface cell from a neighboring gas cell, and  $\bar{i}$  indicates the opposite direction of  $i$ . The equilibrium distribution functions involved are calculated from the gas density  $\rho_G$  and the interface velocity  $\mathbf{u}_I$ , where the gas density is proportional to the gas pressure as  $\rho_G = \frac{1}{c_s^2} p_G$  under the ideal gas assumption with  $c_s$  being the sound speed. The resulting distribution function is stored in the involved gas cell, and it is transmitted to the interface cell in a standard streaming process, so a post-collision mark pc is added to it.

It is worth noticing that half of the distribution functions at the interface should be reconstructed, no matter whether the resourcing post-collision distribution functions come from gas cells or not. As shown in Figure 4.7, the distribution function in the direction  $i$  that satisfies  $\mathbf{n} \cdot \mathbf{e}_i \leq 0$  are reconstructed by Equation (4.11). The underlying mechanism can be found in the calculation of the hydrodynamic force exerted at the interface. Let us mark the interface cell as  $\mathbf{x}$ , then the hydrodynamic force per unit area exerted on the interface can be computed from the velocity moment of all the distribution functions that pass through the

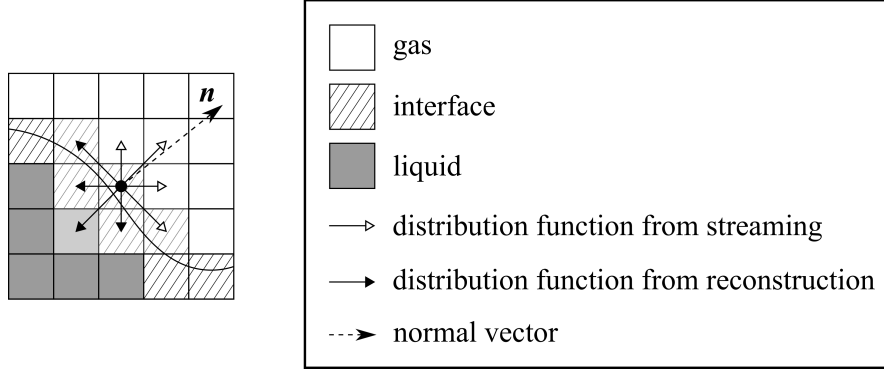


Figure 4.7 – At the interface, distribution functions in the direction  $i$  that satisfies  $\mathbf{n} \cdot \mathbf{e}_i \leq 0$  are reconstructed.

interface, which can be expressed [94] as

$$\begin{aligned}
 \mathbf{F} &= \mathbf{n} \cdot \left[ \sum_{i, \mathbf{n} \cdot \boldsymbol{\xi}_i > 0} f_i^{\text{pc}}(\mathbf{x}, t) (\mathbf{e}_i - \mathbf{u}) (\mathbf{e}_i - \mathbf{u}) \right. \\
 &\quad \left. + \sum_{i, \mathbf{n} \cdot \boldsymbol{\xi}_i \leq 0} f_i^{\text{pc}}(\mathbf{x} - \boldsymbol{\xi}_i \Delta t, t) (\mathbf{e}_i - \mathbf{u}) (\mathbf{e}_i - \mathbf{u}) \right] \\
 &= \mathbf{n} \cdot \sum_{i, \mathbf{n} \cdot \boldsymbol{\xi}_i \leq 0} (f_i^{\text{eq}} + f_i^{\text{eq}}) (\mathbf{e}_i - \mathbf{u}) (\mathbf{e}_i - \mathbf{u}) \\
 &= \mathbf{n} \cdot \sum_i f_i^{\text{eq}} (\mathbf{e}_i - \mathbf{u}) (\mathbf{e}_i - \mathbf{u}).
 \end{aligned} \tag{4.12}$$

By recalling the expression of the velocity moments of the equilibrium distribution function in Equation (2.93), the dynamic force finally equals

$$\begin{aligned}
 \mathbf{F} &= \mathbf{n} \cdot \left[ \sum_i f_i^{\text{eq}} \boldsymbol{\xi}_i \boldsymbol{\xi}_i - 2\mathbf{u} \sum_i f_i^{\text{eq}} + \mathbf{u}\mathbf{u} \sum_i f_i^{\text{eq}} \right] \\
 &= \mathbf{n} \cdot (\rho_G \mathbf{u}\mathbf{u} + p_G \mathbf{I} - 2\rho_G \mathbf{u}\mathbf{u} + \rho_G \mathbf{u}\mathbf{u}) \\
 &= \mathbf{n} \cdot p_G \mathbf{I}.
 \end{aligned} \tag{4.13}$$

From the above derivation, one can find out that the hydronamic force per unit area and the gas pressure are balanced when half of the distribution functions at the interface are reconstructed by Equation (4.11). The reconstruction in [94] is originally designed for simulating metal foaming phenomenon, where the gas pressure  $p_G$  varies in time. Here in the marine engineering applications, the pressure in the open air can be regarded as constant, so the gas pressure is set to be  $p_G = \rho_L c_s^2$ , where  $\rho_L$  is the liquid density.

**Discussion on the dynamic free-surface boundary condition** The adopted reconstruction method is shown to guarantee the pressure continuity across the

free-surface. However, to what extent the real physical boundary condition at the free-surface is satisfied remains to be specified.

The dynamic free-surface boundary condition describes the continuity of stresses across the free-surface [31]. For Newtonian fluids, the stress field at the free-surface can be expressed as

$$\mathbf{t} = \mathbb{T} \cdot \mathbf{n} = (-p^* + \zeta \text{tr} \mathbb{D}) \mathbf{n} + 2\mu \mathbb{D} \cdot \mathbf{n}, \quad (4.14)$$

where  $p^* = p - p_G$  is the relative pressure and  $\mathbb{T}$  is the stress tensor of a Newtonian fluid as

$$\mathbb{T} = (-p^* + \zeta \text{tr} \mathbb{D}) \mathbb{1} + 2\mu \mathbb{D}, \quad (4.15)$$

with  $\mathbb{D}$  being the rate of strain tensor as

$$\mathbb{D} = \frac{1}{2} \left[ \nabla \mathbf{u} + (\nabla \mathbf{u})^T \right]. \quad (4.16)$$

If the surface tension is negligible, as in this case, the stress vector at the free-surface should be zero, i.e.  $\mathbf{t} = \mathbf{0}$  [31]. Projecting this expression onto the normal and tangential direction at the free-surface, the zero normal stress and zero tangential shear stress can be expressed as

$$p^* = \zeta \nabla \cdot \mathbf{u} + 2\mu \mathbf{n} \cdot \frac{\partial \mathbf{u}}{\partial \mathbf{n}}, \quad (4.17)$$

$$\boldsymbol{\tau} \cdot \mathbb{D} \cdot \mathbf{n} = 0. \quad (4.18)$$

By comparing the dynamic boundary condition that the adopted reconstruction method satisfies, i.e. Equation (4.13), and the physical one, i.e. Equation (4.17) and (4.18), one can observe that the adopted reconstruction method (4.11) only considers the normal stress continuity without any viscous effects. Considering that the viscosity is usually neglected near the free-surface in marine engineering problems, the current reconstruction method is acceptable.

## 4.5 Algorithm

With all the operations expounded in the previous sections, a robust free-surface model is developed. The implementation of the free-surface model in the RLBM (FS-RLBM) is summarized as

---

**Algorithm:** FS-RLBM

---

**Require:**  $f_i(\mathbf{x}, t^n)$ ,  $\rho(\mathbf{x}, t^n)$ ,  $\mathbf{u}(\mathbf{x}, t^n)$ ,  $\mathbf{F}(\mathbf{x}, t^n)$ ,  $\alpha(\mathbf{x}, t^n)$ ,  $m(\mathbf{x}, t^n)$  and *flag* array from the previous time-step

1. For liquid and interface cells, implement the collision and streaming procedure (i.e. from Step.1 to Step.6 in the RLBM algorithm shown in Section 3.2),
  2. For interface cells, compute the missing distribution functions by Equation (4.11),
  3. For liquid and interface cells, calculate  $\rho(\mathbf{x}, t^{n+1})$ ,  $\mathbf{u}(\mathbf{x}, t^{n+1})$  by Equation (2.69),
  4. For liquid and interface cells, adapt  $m(\mathbf{x}, t^{n+1})$  by Equation (4.3) and compute  $\alpha(\mathbf{x}, t^{n+1})$ ,
  5. Copy the *flag* array at  $t^n$  to an array *flag\**,
  6. For interface cells, check  $\alpha(\mathbf{x}, t^{n+1})$  with the criterion in Section 4.2 based on the *flag*, and the temporary *flag*( $\mathbf{x}, t^{n+1}$ ) is stored in *flag\** array,
  7. Check if filled interface cells and emptied interface cells are adjacent and if isolated interface cell exists, and determine the *flag\** array,
  8. Modify *flag*( $\mathbf{x}, t^{n+1}$ ) by copying data from *flag\** array,
  9. Initialize the newly formed interface cells by Equation (4.2),
  10. For the cells involved in the flag change, modify  $m(\mathbf{x}, t^{n+1})$  by Equation (4.7) and adapt  $\alpha(\mathbf{x}, t^{n+1})$ ,
  11. Goto Step.1 for the next time-step.
- 

## 4.6 Validations

### 4.6.1 Viscous standing wave

In this problem, a periodic standing wave of wavelength  $\lambda = 2.0\text{m}$  and wave steepness  $\varepsilon = 0.05$  is considered. The wave steepness is the ratio of the wave height  $2A$  to the wavelength  $\lambda$ , i.e.  $\varepsilon = 2A/\lambda$  where  $A$  is the wave amplitude. It is pointed out in [31, 116] that the potential theory gives an approximate solution to this problem, and the velocity potential reads

$$\varphi(x, y, t) = -\frac{Ag \cosh[k(y + H)]}{\omega \cosh(kH)} \cos(kx) \cos(\omega t), \quad (4.19)$$

where  $g$  is the gravity acceleration,  $k = 2\pi/\lambda$  is the wave number,  $H$  is the water depth of calm water, and consequently  $\omega = \sqrt{gk \tanh(kH)}$  is the angular frequency, and  $T = 2\pi/\omega$  is the wave period. One can observe that Equation (4.19) not only is periodic in the  $x$ -direction, but also satisfies symmetry at  $x = \frac{i\lambda}{2}, \forall i \in \mathbb{Z}$ . Hence the computation domain is chosen to be of width  $L = \lambda/2$  with symmetric boundary conditions used on the two vertical walls, as shown in Figure 4.8.

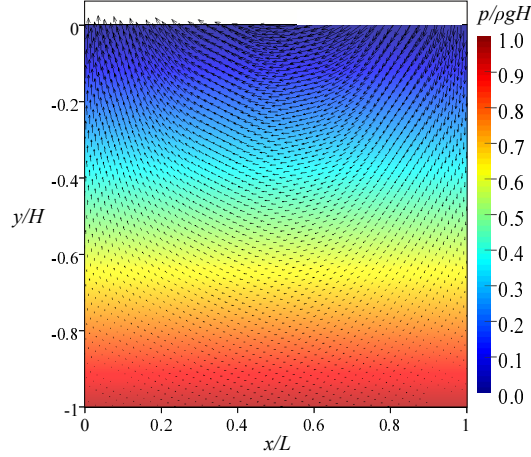


Figure 4.8 – Initial state of the viscous standing wave problem.

At time  $t = 0$ , the free surface profile is a horizontal line at  $y = 0$ , and the pressure field is assumed to be hydrostatic. Besides, the velocity field is initialized as the gradient of the velocity potential  $\nabla\varphi_0$ , where  $\varphi_0 = \varphi(x, y, 0)$ . From simple computation, one can calculate that the maximum velocity appears at  $t = 0$ , which is  $u_{\max} = \frac{Agk}{\omega}$ . Consequently, the Reynolds number is defined as  $Re = \frac{\lambda u_{\max}}{\nu}$ .

If the fluid is inviscid, the total kinetic energy of the system is conserved in time, and the Reynolds number is infinite. However, for a viscous case as discussed here, the Reynolds number is of finite value, and the kinetic energy dissipates due to the viscous effect. For the viscous standing wave at Reynolds number  $Re = 100$ , the snapshots of the flow field at some typical time instants are shown in Figure 4.9, where the results are obtained from the present RLBM scheme with a lattice resolution of 80 in one wave height.

Generally speaking, the RLBM scheme works well with the adopted free-surface model and provides reasonable results. However, small horizontal velocities are observed in the area close to the free-surface at  $t = 0.25T$  and  $t = 0.75T$  when the velocity in the fluid domain is supposed to be zero, and the free-surface is not perfectly horizontal at  $t = 0.50T$  and  $t = 1.00T$ . One of the reasons is that a slight difference of the time period exists between the numerical and the analytical solutions, and another reason may lie in the discrete nature of the interface

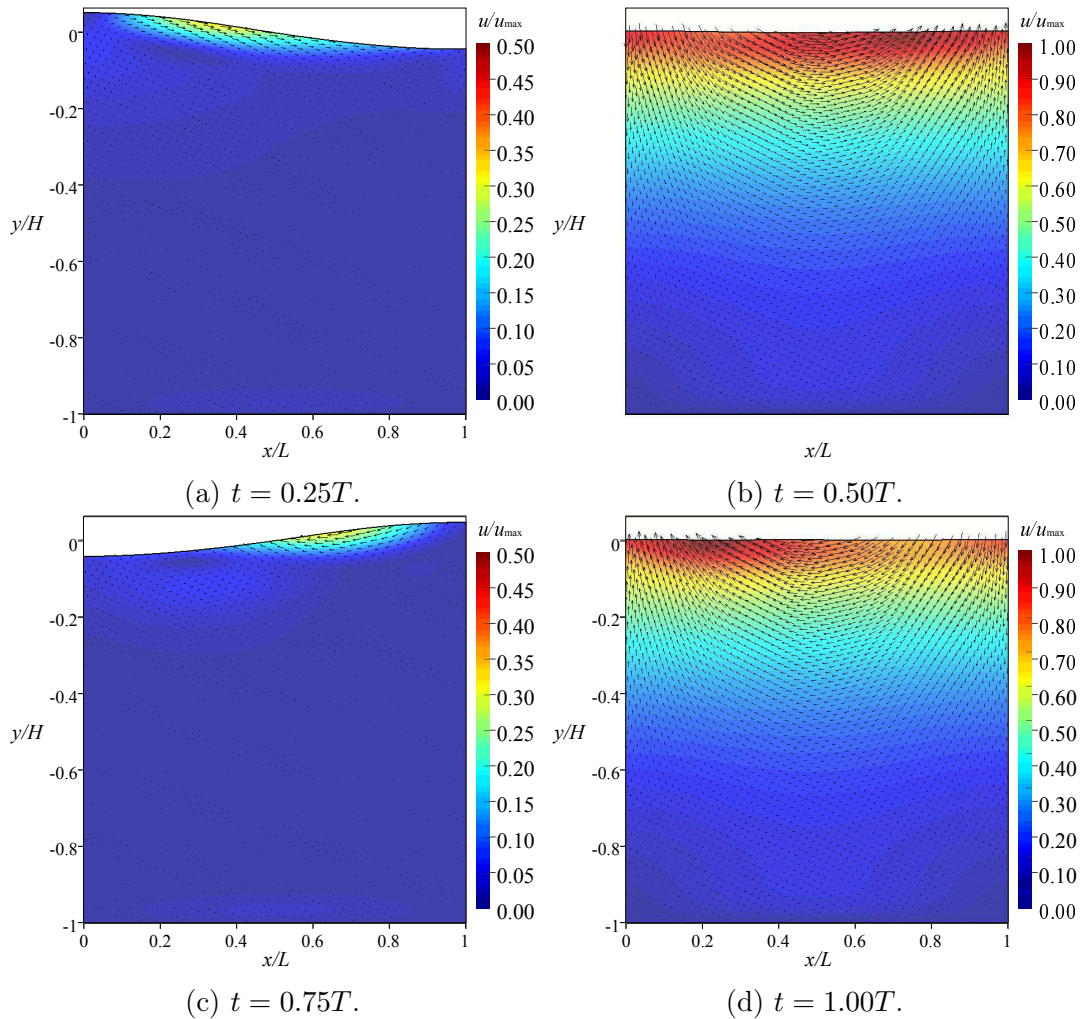


Figure 4.9 – Snapshots of the viscous standing wave flow at  $Re = 100$ , where the color indicates the relative velocity magnitude  $u/u_{\max}$ . The results are obtained from the present RLBM scheme with a lattice resolution of  $2A/\Delta x = 80$ .

evolution mechanism of the adopted free-surface model which might introduce small perturbations from the staircase-like interface layer.

For a more precise validation, we extract the evolution of the total kinetic energy of the system in Figure 4.10, where the analytical solution of the kinetic energy damping is given in [31, 116] as

$$E_t = \frac{\lambda A^2 g}{8} e^{-4\nu k^2 t} [1 + \cos(2\omega t)]. \quad (4.20)$$

As one can observe, for the adopted four lattice resolutions ( $2A/\Delta x = 20, 40, 60$  and  $80$ ), the results converge as the grid is refined. The numerical results have a time period very close to the analytical solution, whereas the damping rate of the kinetic energy is a little higher than in the analytical prediction. It is necessary to note that the analytical solution, which is obtained from the linear theory, has its own error at the wave steepness  $\varepsilon = 0.05$ . This error would be reduced for smaller

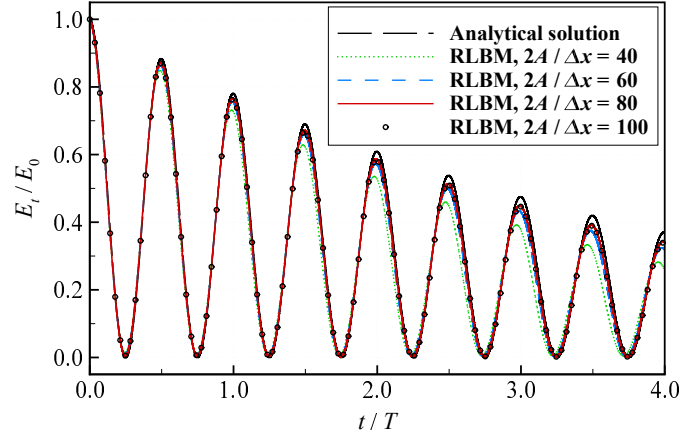


Figure 4.10 – Decay of the total kinetic energy in the viscous standing wave problem.

amplitude waves. However, in order to get converged numerical results with an adequate lattice resolution, the calculation would become extremely costly, therefore we stop at the present wave steepness for the moment. In addition, the relative kinetic energy value is close to 0 at  $t = 0.25T$  and  $t = 0.75T$ , which suggests that the aforementioned velocity errors near the surface are acceptable. Moreover, the numerical results of the SRT-LBM and RLBM schemes are compared to each other, where the same lattice resolution  $2A/\Delta x = 80$  is adopted.

Figure 4.11a and 4.11b show the time evolution of the total kinetic energy and the water depth at the left ( $x = 0$ ) and the right ( $x = L$ ) boundaries of the computation domain. These two results are nearly coincident, which indicates that the regularization procedure brings no extra numerical dissipation for free-surface flows at small Reynolds numbers.

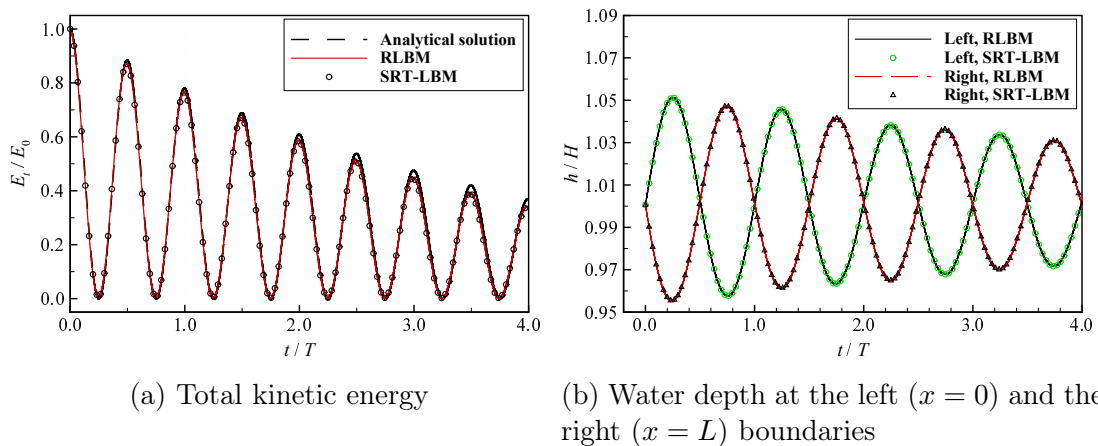


Figure 4.11 – Time evolution of the total kinetic energy of the system and the water depth at both the left ( $x = 0$ ) and the right ( $x = L$ ) boundaries of the computation domain, based on the results obtained with SRT-LBM and RLBM with a lattice resolution of  $2A/\Delta x = 80$ .

### 4.6.2 Dambreak flow

The dambreak flow is a much more violent situation. Figure 4.12 gives the initial configuration of the simulation, which is of the same size as in the experiment conducted by Lobovsky et al. [122]. A 600mm ( $L$ )  $\times$  300mm ( $H$ ) water column is

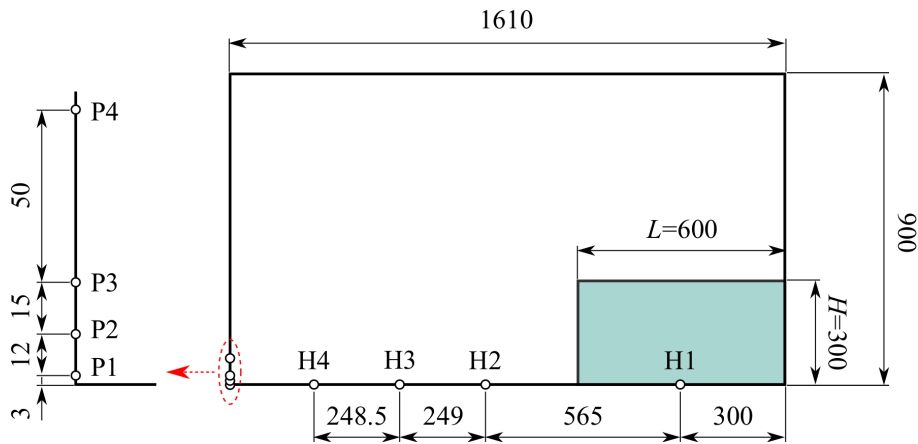


Figure 4.12 – Initial configuration of the dambreak problem (the unit length is 1mm)

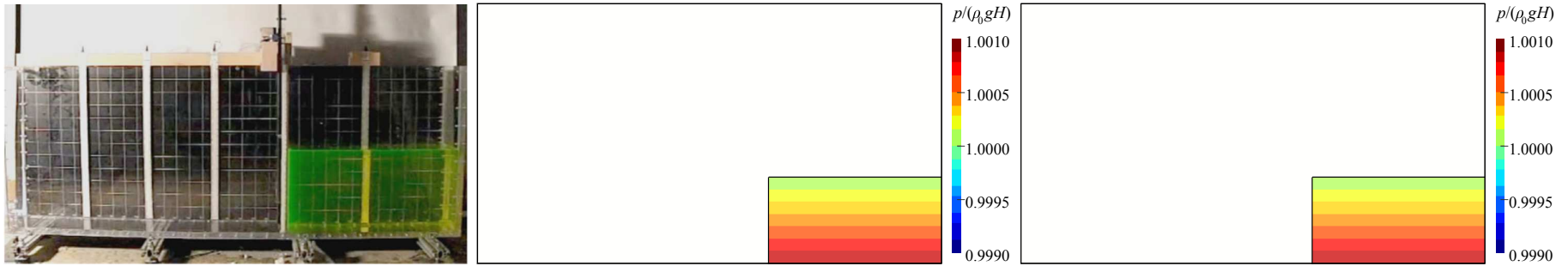
reserved to the right side in a 1610mm  $\times$  900mm water tank. The water column collapses due to gravity and impacts on the left vertical wall. Four pressure sensors are distributed vertically on the left wall to record the impact pressure signals, which are fixed at the heights 3mm, 15mm, 30mm and 80mm and respectively marked as P1, P2, P3 and P4. Apart from the impact pressures, the free-surface shape is also of great interest. In the experiment [122], the free-surface shape is depicted by the water front position and the water level at several chosen locations, which are positioned downstream from the right wall at 300mm, 865mm, 1114mm and 1362.5mm and hereafter labeled as H1, H2, H3 and H4. Here we examine the same variables. We must mention that there are two major differences between the numerical and the experimental configurations. The first one is that the water tank in the simulation is a sealed one, whereas it has an open roof in the experiment. The sealed tank will limit the water jet within a finite height and makes it fall back earlier than in the experiment. This falling back behavior occurs late in time, outside the period that we are interested in, hence the open boundary is not considered in the simulation for now. The second one is that the dambreak flow in the experiment is triggered by fast releasing a vertical wall which initially hold the water column, while in the numerical simulation the flow automatically begins when the clock starts to tick.

### Free-surface profile and the pressure field

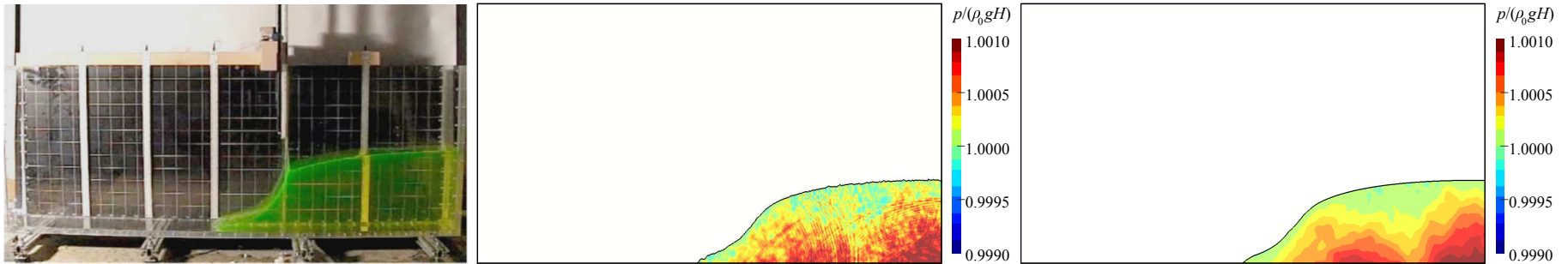
In the present work, the water column is discretized by a  $600 \times 300$  lattice and initialized as hydrostatic. The discrete time step is  $\Delta t = 1 \times 10^{-5}$ s. The gravity acceleration is  $g = -9.81\text{m/s}^2$ . The equivalent Reynolds number of this first simulation is  $Re = Au/\nu = 2.0 \times 10^4$  and the Froude number is  $Fr = u/\sqrt{gH} = 2$ , where the characteristic velocity  $u$  is the predicted water front speed  $\sqrt{2gH}$ , and the characteristic length  $A$  is chosen to be the same as in the experiment which is the distance between the water column and the left wall. Since the viscous effect is not dominant, a half-way specular reflecting boundary condition (see Section 2.6.2) is adopted to mimic free-slip solid walls.

Figure 4.13 shows a time series of free-surface profiles obtained by the SRT-LBM and RLBM schemes, in comparison with the ones from the experiment [122]. Right after the experiment begins, one can observe in Figure 4.13b that some fluid is lifted up near the upper-left corner of the water column by the releasing gate, whereas the numerical free-surface remains smooth because of the absence of a numerical moving gate. At  $t = 449.9\text{ms}$  the water front reaches the left wall (see Figure 4.13e), then the leading water climbs upwards by inertia (see Figure 4.13f) and falls back due to gravity (see Figure 4.13g-4.13h). The falling water and the spreading current form an air bubble and a water jet (see Figure 4.13i).

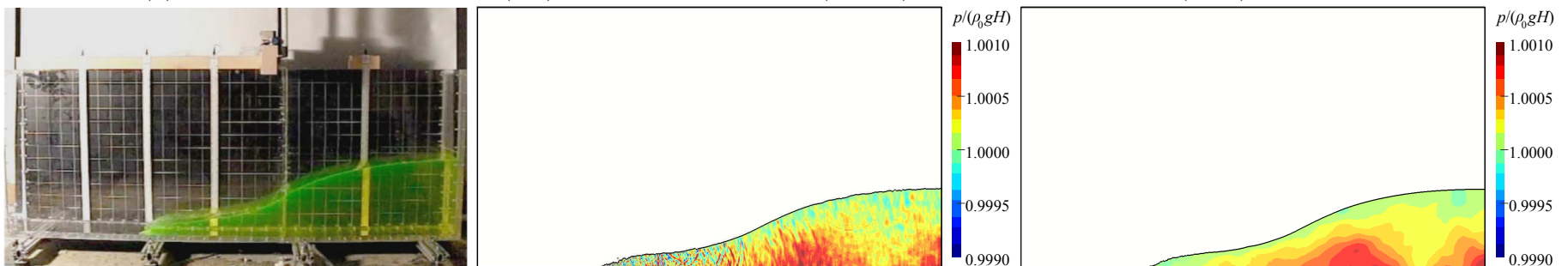
In general, both the SRT-LBM and RLBM schemes succeed to reproduce the dambreak flow. However in the SRT-LBM results, small perturbations are observed on the free-surface throughout the whole process, especially at the top of the water column and near the water front. Correspondingly, some abrupt pressure signals are introduced into the pressure field from these perturbations. These pressure signals ripple on the main pressure field, propagate inwards from the free-surface and reflect on the water tank boundaries, which can clearly be seen in Figure 4.13d, 4.13g and 4.13h. The resulting fluctuating pressure field results from the instability of the SRT-LBM scheme with a relaxation time too close to 0.5 which is unavoidable in order to reach high Reynolds numbers. This phenomenon was previously discussed for the lid-driven cavity flow test-case in Section 3.4. What makes it even worse in this case, in the adopted free-surface model, so that the interface movement highly depends on the volume fraction change, which is calculated from the exchanges of density between the lattice cells. Since the density is proportional to the pressure in the LB method, these abrupt pressure values will lead to unexpected volume fractions and finally result in the perturbations on the interface profile. On the contrary, the RLBM scheme provides smooth free-surface shape and pressure field, even when the water impacts on the left wall.



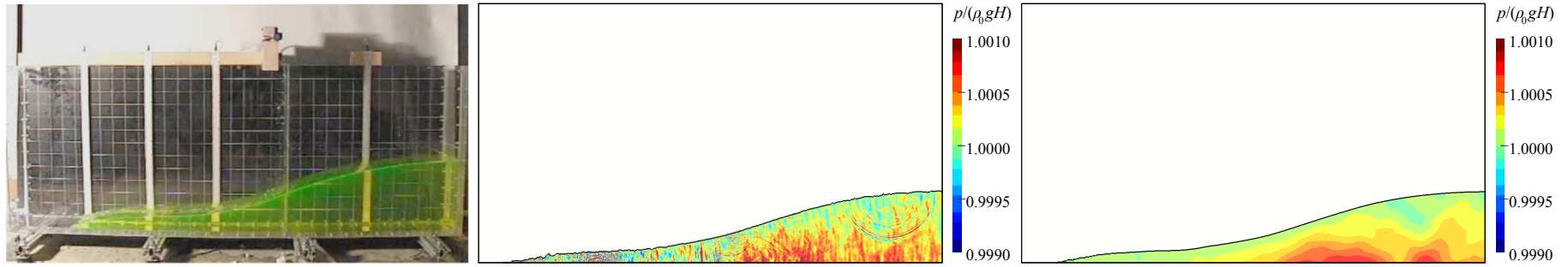
(a) Results from the experiment (left), the SRT-LBM scheme (middle) and the RLBM scheme (right) at  $t = 0.0\text{ms}$ .



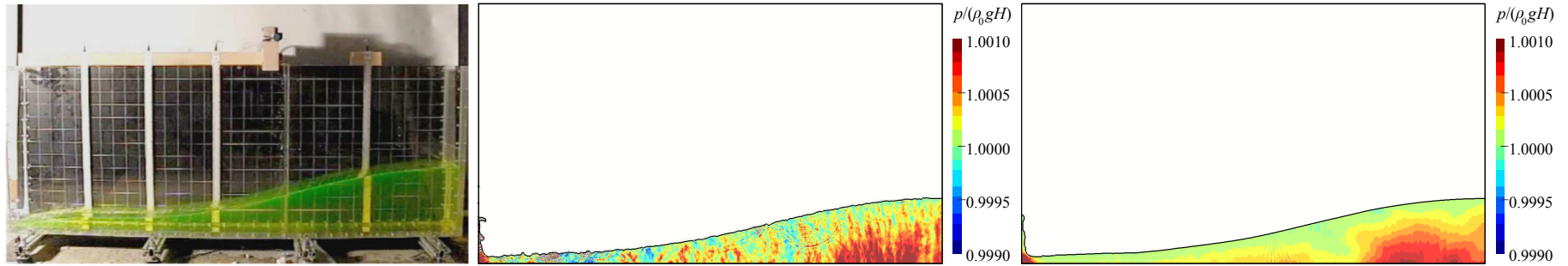
(b) Results from the experiment (left), the SRT-LBM scheme (middle) and the RLBM scheme (right) at  $t = 159.9\text{ms}$ .



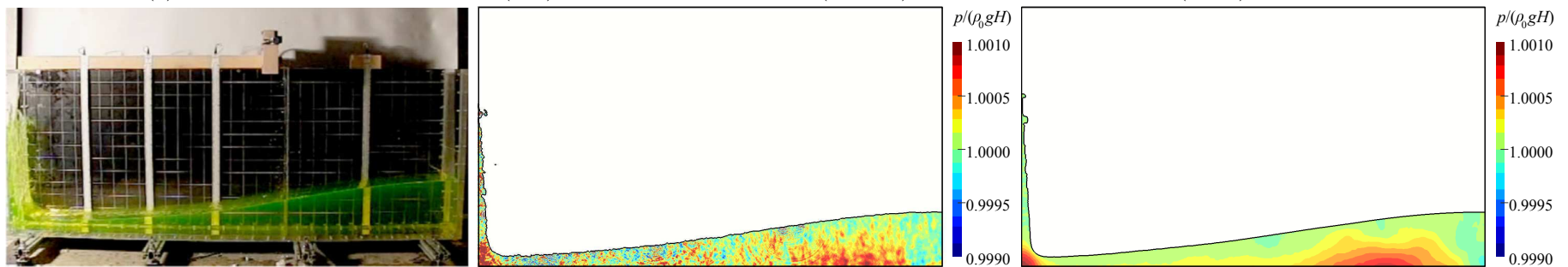
(c) Results from the experiment (left), the SRT-LBM scheme (middle) and the RLBM scheme (right) at  $t = 276.6\text{ms}$ .



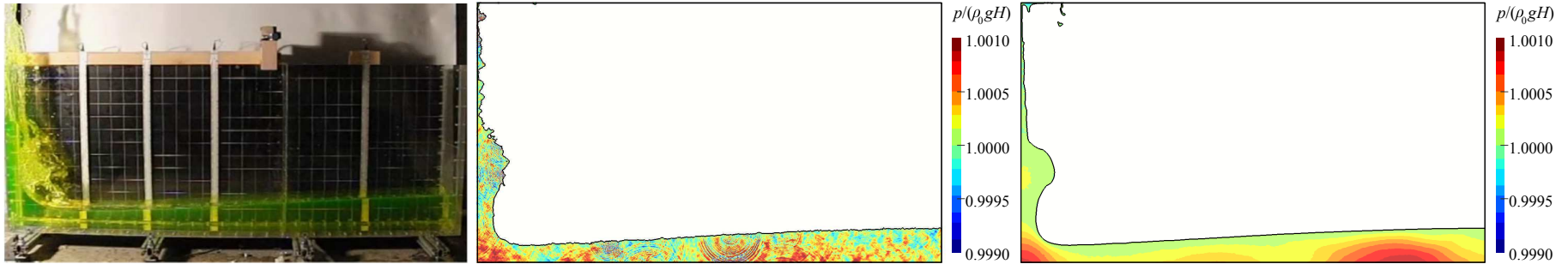
(d) Results from the experiment (left), the SRT-LBM scheme (middle) and the RLBM scheme (right) at  $t = 373.3\text{ms}$ .



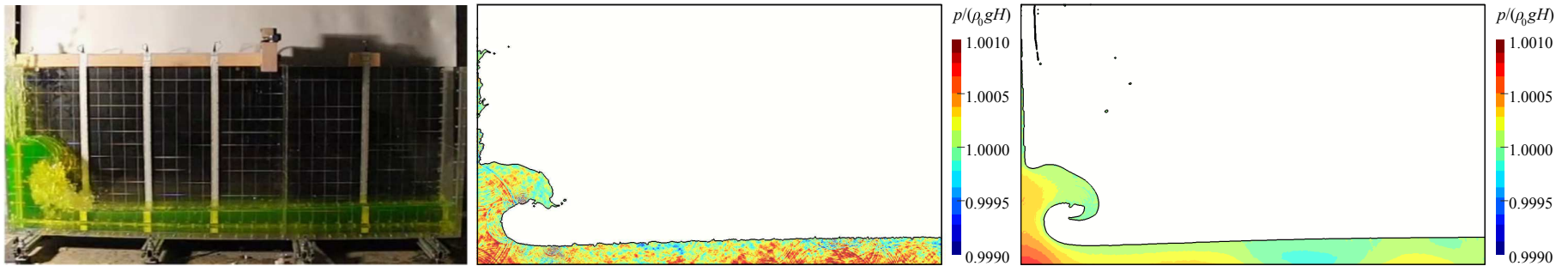
(e) Results from the experiment (left), the SRT-LBM scheme (middle) and the RLBM scheme (right) at  $t = 449.9\text{ms}$ .



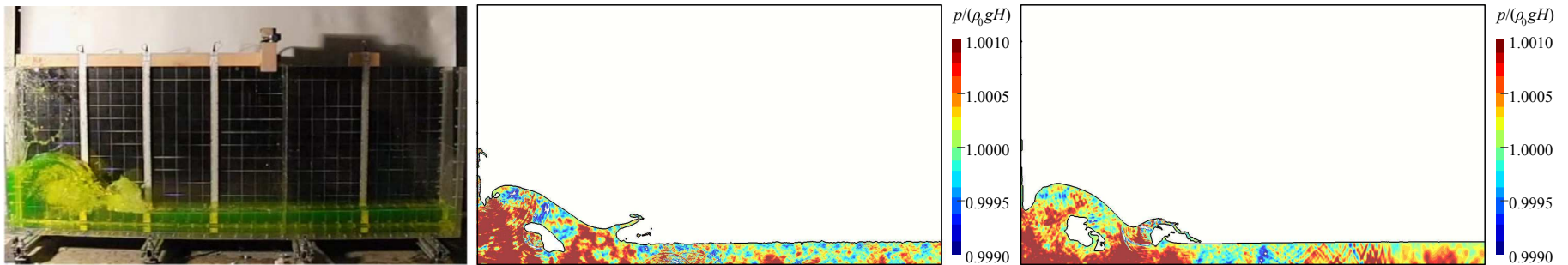
(f) Results from the experiment (left), the SRT-LBM scheme (middle) and the RLBM scheme (right) at  $t = 573.3\text{ms}$ .



(g) Results from the experiment (left), the SRT-LBM scheme (middle) and the RLBM scheme (right) at  $t = 862.3\text{ms}$ .



(h) Results from the experiment (left), the SRT-LBM scheme (middle) and the RLBM scheme (right) at  $t = 1023.3\text{ms}$ .



(i) Results from the experiment (left), the SRT-LBM scheme (middle) and the RLBM scheme (right) at  $t = 1166.6\text{ms}$ .

Figure 4.13 – Snapshots of free-surface profiles and pressure fields at time 0.0, 159.9, 276.6, 373.3, 449.9, 573.3, 862.3, 1023.3, 1166.6ms. The experimental results (left), the SRT-LBM results (middle) and the RLBM results (right) are shown.

### Water front position and the water levels

The evolution of the water front position is shown in Figure 4.14, and the time history of the water levels at the given locations [122] is shown in Figure 4.15.

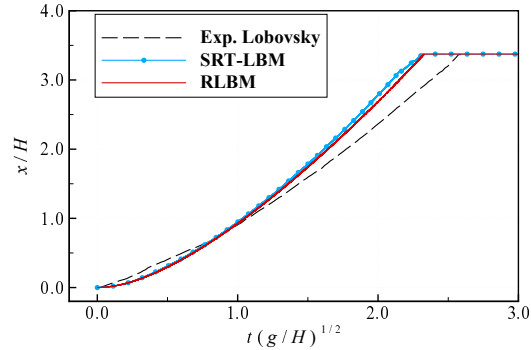


Figure 4.14 – Evolution of the water front position.

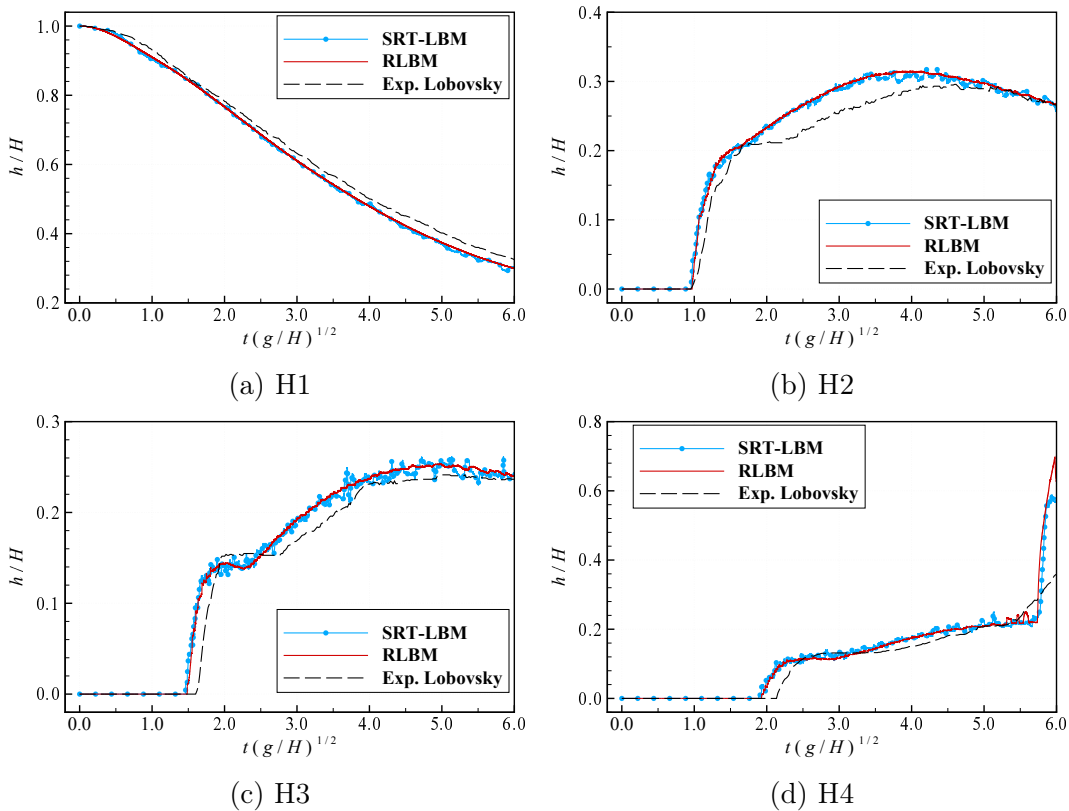


Figure 4.15 – Evolution of the water levels at H1, H2, H3 and H4 positions.

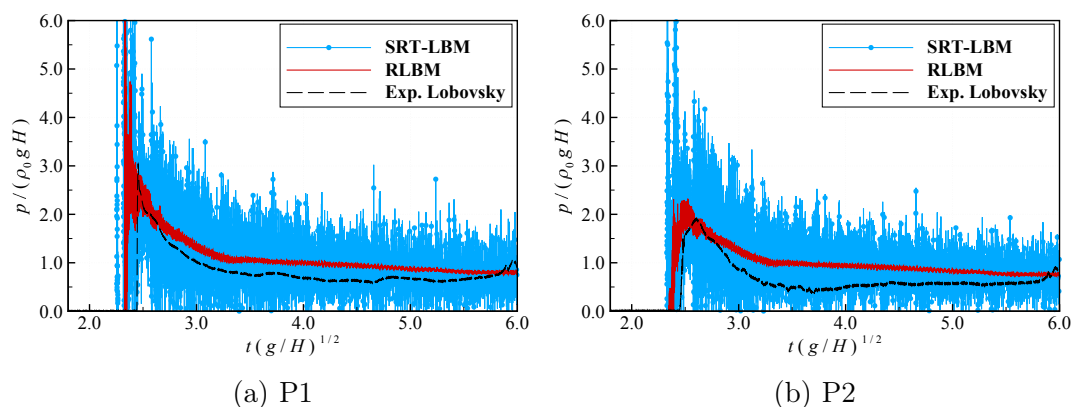
It is observed that the simulated water front moves faster than the experimental one. The same phenomenon can be observed in the water level evolution in Figure 4.15: in the numerical results the water level at H1 position drops faster than in the experiment, and the water level rises earlier at H3 and H4. Two facts may contribute to this time difference. The first one is the effect of gate motion, namely

in the experiment, a boundary layer is developed near the lifted gate, which will hold the water front for a while and thus make it slower than the numerical results. The other reason may be the use of free-slip boundary condition in the simulation. In this aspect, the study of Marrone et al. [128] provides some evidences, where both free-slip boundary and non-slip boundary conditions are tested in terms of the arriving time when the water front hits the wall. Their results confirmed that the water impact did occur earlier in the free-slip case than in the non-slip cases, even when the Reynolds number for the non-slip case is as large as  $Re = 10000$ . This indicates that adopting the non-slip boundary condition may be closer to the physics nature, but it requires accurately discretizing the boundary layer and thus needs a very fine mesh close to the boundary, which is considered to be expensive for a simulation. Besides, the SPH results in [128] also showed that the time difference of the water impact is reduced when the Reynolds number is increasing for the non-slip case. Based on this consideration, we think that the present practice of applying the free-slip boundary condition is acceptable.

In addition, the smooth RLBM curve indicates a smooth free-surface evolution, while the high-frequency vibration on the SRT-LBM curve corresponds to a disturbed free-surface, as already discussed for the snapshots in Figure 4.13.

### Pressure signal

The pressure signals recorded at P1, P2, P3 and P4 are plotted in Figure 4.16, where the numerical curves are based on raw pressure data without any filtering operation. As discussed in the previous analysis, the numerical water front has a larger speed than the experimental one due to the free-slip numerical tank assumption, hence the first peaks of the numerical pressure signals appear earlier than the experimental ones for the same reason. It is also observed from the snapshots in Figure 4.13 that a smooth free-surface profile and pressure field are obtained by the RLBM while the smoothness cannot be maintained by the SRT-LBM. This is confirmed in Figure 4.16 with more details. The first peaks of the SRT-LBM



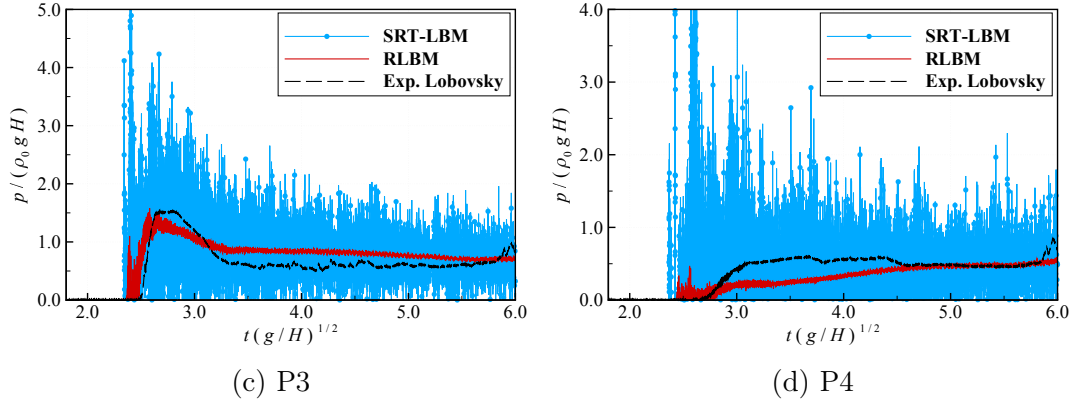


Figure 4.16 – Evolution of the pressure signals at P1, P2, P3 and P4 positions.

pressure goes up to extremely high values at the four pressure sensors, whereas the RLBM pressure peaks are similar with the experimental ones. Furthermore, the SRT-LBM pressure is oscillating wildly, while this severe fluctuation is remarkably reduced by the RLBM scheme. From this comparison, the regularization in the RLBM scheme is verified to be able to largely improve the numerical stability of the LB method in high Reynolds number applications.

### Reynolds number dependency study

The previously presented numerical results are obtained at a Reynolds number of  $Re = 2.0 \times 10^4$ , but the Reynolds number in the experiment [122] is as high as  $Re = 3.8 \times 10^6$ . Hence it is necessary to understand the role of the Reynolds number in the simulations. In this context, several other simulations are carried out using the same lattice, whose Reynolds number respectively equals  $1.0 \times 10^4$ ,  $4.0 \times 10^4$  and  $8.0 \times 10^4$ . Their water front position and water level evolutions are shown in Figure 4.17 and 4.18. The RLBM result does not change much when the Reynolds number is increased by one order of magnitude, which indicates that even Reynolds number  $1.0 \times 10^4$  is large enough for the simulation, meaning that

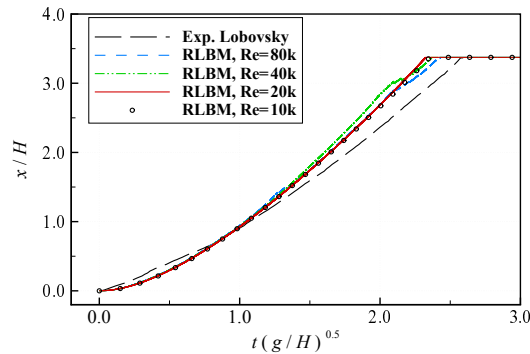


Figure 4.17 – Evolution of the water front position obtained with the RLBM at  $Re = 1.0 \times 10^4$ ,  $2.0 \times 10^4$ ,  $4.0 \times 10^4$  and  $8.0 \times 10^4$ .

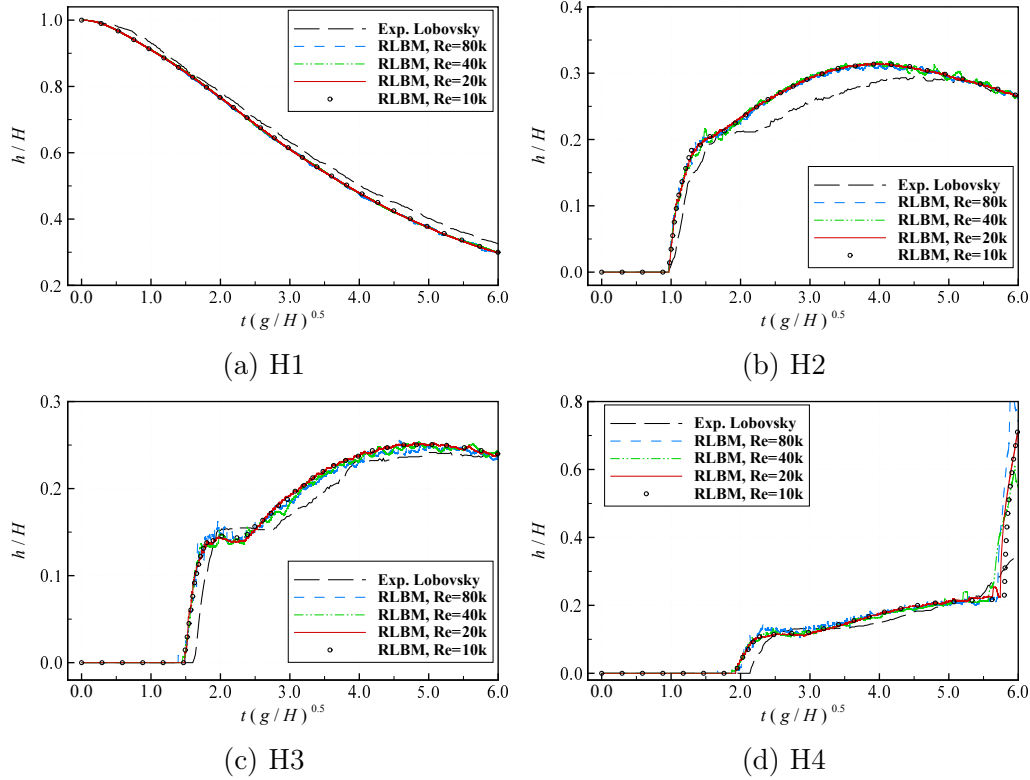


Figure 4.18 – Evolution of the water level at H1, H2, H3 and H4 positions, obtained with the RLBM at  $Re = 1.0 \times 10^4$ ,  $2.0 \times 10^4$ ,  $4.0 \times 10^4$  and  $8.0 \times 10^4$ .

the viscous effect is relatively too small to be observed, apart in the boundary layer which is not modeled as already discussed. With a Reynolds number starting from  $Re = 4.0 \times 10^4$ , small oscillations can be seen on the RLBM curves, which indicates that perturbations begin to occur on the free-surface. However, the oscillation of the RLBM result at  $Re = 8.0 \times 10^4$  is still weaker than that of the SRT-LBM result at  $Re = 2.0 \times 10^4$  (see Figure 4.15).

The pressure signals at the different Reynolds numbers are shown in Figure 4.19. One can observe that the peak values at the four pressure sensors tend to increase when the Reynolds number augments, and the scale of pressure oscillations also grows a lot. Once again, compared to the SRT-LBM results at the lower Reynolds number  $Re = 2.0 \times 10^4$ , i.e. Figure 4.19, the pressure evolution of the RLBM results are still more stable.

### Short comment on MRT-LBM

It is worth mentioning here that the MRT-LBM is absent in this test-case because its calculation is interrupted very fast due to numerical instability and it is not able to reproduce the dambreak completely. For example with  $Re = 1.0 \times 10^4$ , the MRT-LBM calculation is interrupted after the water front impacts on the left wall. The snapshot of the fluid system at a time closely before the interruption is

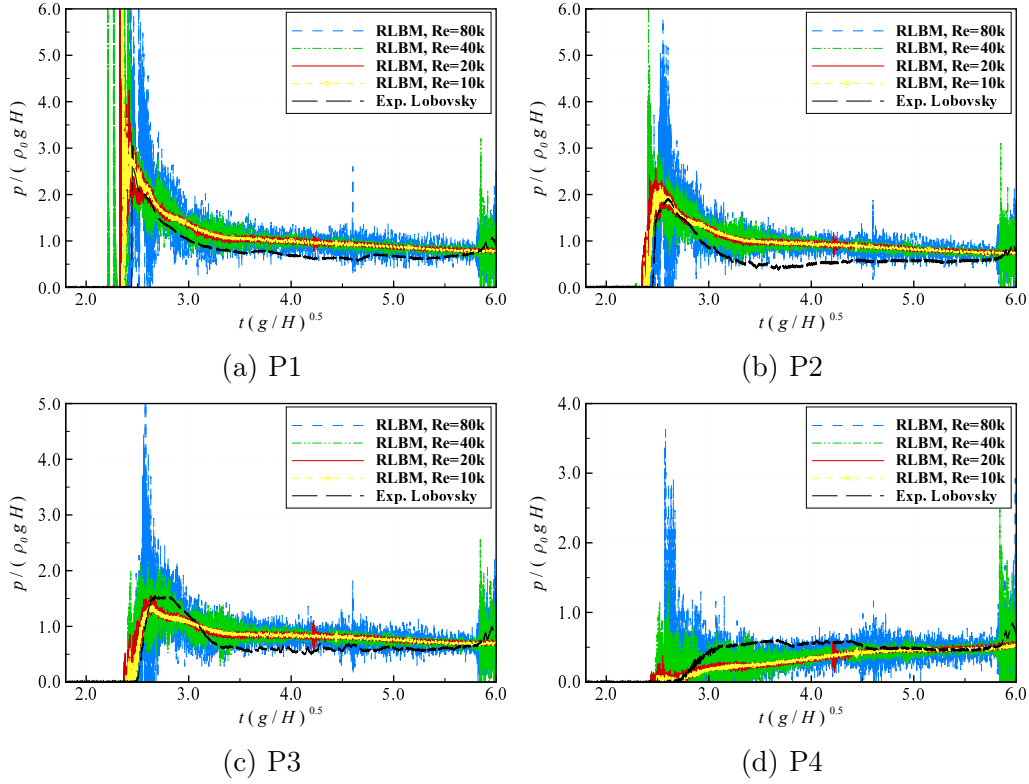


Figure 4.19 – Pressure signals at P1, P2, P3 and P4 positions, obtained with the RLBM at  $Re = 1.0 \times 10^4$ ,  $2.0 \times 10^4$ ,  $4.0 \times 10^4$  and  $8.0 \times 10^4$ .

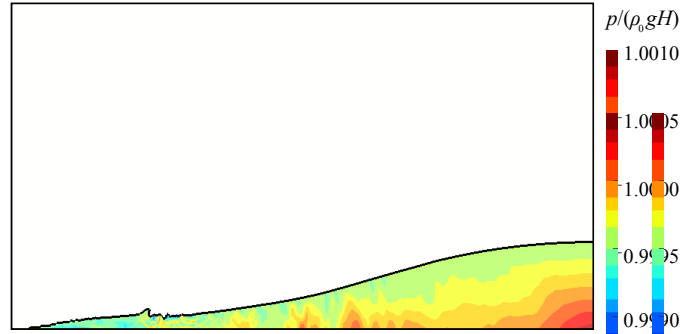


Figure 4.20 – Snapshot of the MRT-LBM result at  $t = 449.9\text{ms}$ .

shown in Figure 4.20. Although the pressure field near the bottom looks as smooth as in the RLBM result, a strange bump appears on the free-surface near the water front. This area is also where similar but smaller perturbations are observed in the SRT-LBM case as shown in Figure 4.13. As for the case  $Re = 2.0 \times 10^4$ , the interruption of the MRT-LBM computation occurs even earlier due to the disorder of the free-surface.

## 4.7 An improved free-surface LB model

In the previous section, the adopted VOF-based free-surface model [94] with RLBM has been validated through two simulations. Although good results have been obtained, compared with analytical or experimental solutions, there is still some room for improvements. In this section, a new way of reconstructing the distribution functions at the free-surface is proposed.

### 4.7.1 Dilemmas of the original free-surface LB model

The original free-surface model [94] calculates the missing distribution functions at the free-surface in a way to satisfy the dynamic boundary condition that the gas pressure imposed on the interface is balanced by the hydrodynamic force from the liquid side. Recalling Equations (4.12) and (4.13), the procedure reconstructs a target distribution function based on the post-collision one in the inversed direction. Such paired nature requires one to employ the reconstruction operation to four of the nine distribution functions, i.e.  $\forall \mathbf{n} \cdot \boldsymbol{\xi}_i < 0$ . However, this strict requirement may encounter some dilemma in certain situations.

One of the possible dilemma can be found at the edge of a convex free-surface profile. Figure 4.21 gives an example of the initial state of the dambreak test-case. The interface cell at the corner of the water column has five missing dis-

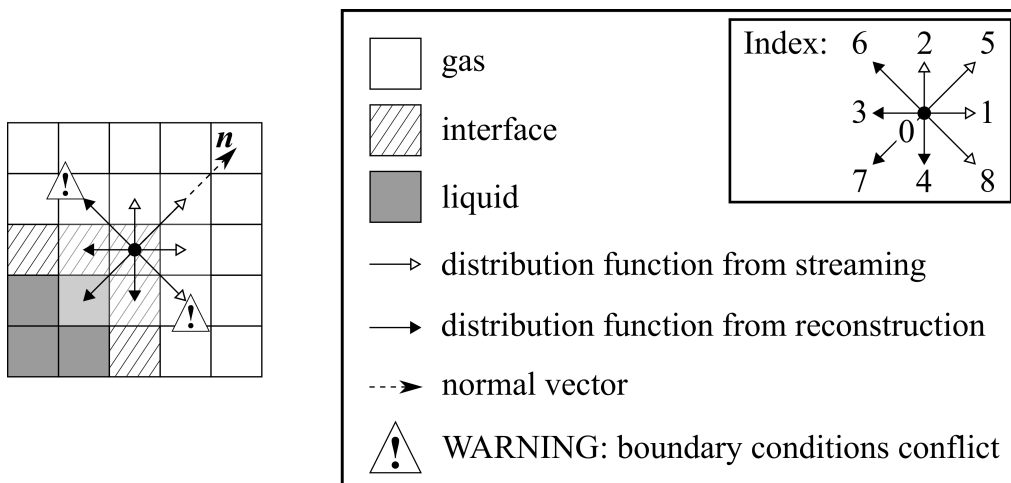


Figure 4.21 – Boundary treatment for the convex free-surface profile.

tribution function, which are  $f_3$ ,  $f_4$ ,  $f_6$ ,  $f_7$  and  $f_8$ . The criterion of  $\forall \mathbf{n} \cdot \boldsymbol{\xi}_i < 0$  only involves  $f_3$ ,  $f_4$  and  $f_7$ . In order to include the other two, one has to take  $\forall \mathbf{n} \cdot \boldsymbol{\xi}_i = 0$  into consideration. More generally, the criterion should be modified as  $\forall (\mathbf{n} \cdot \boldsymbol{\xi}_i \leq 0) \vee (flag(\mathbf{x} - \boldsymbol{\xi}_i \Delta t) \text{ is gas})$  for all the possible situations, where the symbol  $\vee$  denotes the logical "or". This new criterion may lead to an over-reconstructed set of distribution functions at the interface and hence disobeys the

hydrodynamic condition.

Another dilemma occurs at the three-phase point at the water front in the dambreak test-case, see Figure 4.22. At a boundary cell close to the free-slip solid

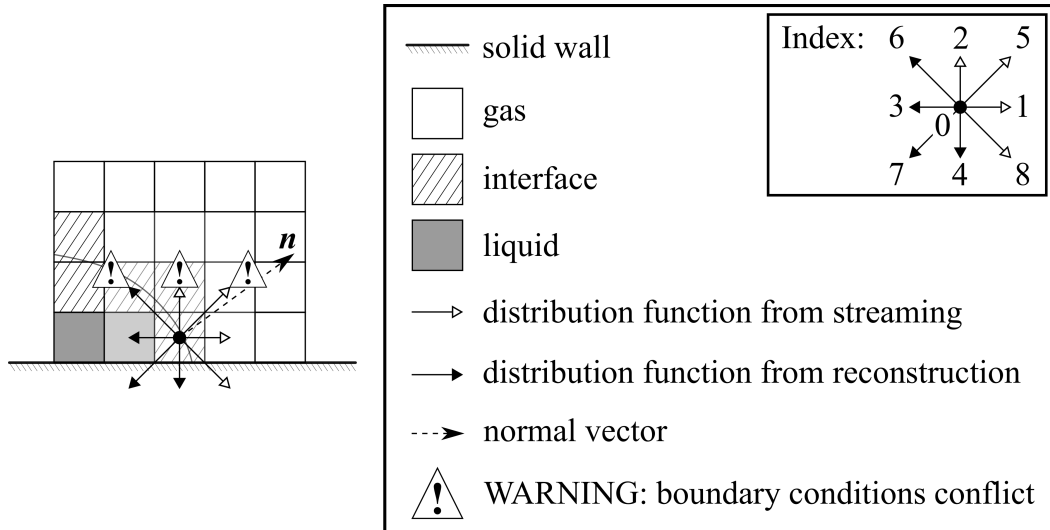


Figure 4.22 – Boundary treatment at the three-phase point.

wall, the distribution functions  $f_2$ ,  $f_5$  and  $f_6$  need to be computed by the specular boundary condition (see Section 2.6.2). However, the original free-surface model requires  $f_3$ ,  $f_4$ ,  $f_6$  and  $f_7$  to be reconstructed and  $f_1$ ,  $f_2$ ,  $f_5$  and  $f_8$  to be streamed. In this way, the two boundary conditions conflict, which means that if the dynamic condition is satisfied by the reconstruction procedure, then the free-slip condition cannot be guaranteed, and vice versa. To make matters worse, sometimes the number of distribution functions that can be streamed from neighboring cells are very limited, due to the incomplete neighborhood lattice near the wall, which causes greater confusion in the priority sequence among streaming, the specular rule and the reconstruction.

#### 4.7.2 A new distribution method for the distribution functions at the free-surface

To provide a countermeasure for the aforementioned dilemmas of the original model, a new way of reconstructing the distribution functions at the free-surface is proposed here. The idea is inspired by the work of Latt et al. [102], where a similar boundary condition was introduced for straight walls. The new reconstruction method deals with the equilibrium part of the distribution function and the non-equilibrium part separately. The equilibrium distribution function can be

computed from its definition, i.e.

$$f_i^{\text{eq}} = w_i \rho \left[ 1 + \frac{\boldsymbol{\xi}_i \cdot \mathbf{u}^*}{c_s^2} + \frac{\mathbf{u}^* \mathbf{u}^* : (\boldsymbol{\xi}_i \boldsymbol{\xi}_i - c_s^2 \mathbf{I})}{2c_s^4} \right], \quad (4.21)$$

if the density  $\rho$  and the fluid velocity  $\mathbf{u}^*$  are known. The non-equilibrium part is calculated in the same way as previously introduced in Section 3.4.1, which reads

$$f_i^{\text{neq}} \approx \frac{\tau \Delta t \rho}{c_s^2} (\boldsymbol{\xi}_i \boldsymbol{\xi}_i - c_s^2 \mathbf{I}) : \nabla \mathbf{u}^*. \quad (4.22)$$

Afterwards, the distribution function can be reconstructed as

$$f_i = f_i^{\text{eq}} + f_i^{\text{neq}}. \quad (4.23)$$

The remaining part is to determine the values of the macroscopic variables at the interface. In the present work, an inverse distance extrapolation is adopted. For an interface cell at position  $\mathbf{x}$ , its macroscopic variables are extrapolated from its neighboring liquid cells within a searching radius of  $r$ . The inverse distance weight of each supporting liquid cell at position  $\mathbf{x}_i$  reads

$$w_i^\dagger = \frac{1}{d_i^p}, \quad (4.24)$$

where  $d_i$  is the distance between  $\mathbf{x}$  and  $\mathbf{x}_i$ . Then any variable  $\phi(\mathbf{x})$ , such as the density and the flow velocity, can be calculated from

$$\phi(\mathbf{x}) = \frac{\sum_i w_i^\dagger \phi(\mathbf{x}_i)}{\sum_i w_i^\dagger}. \quad (4.25)$$

Consequently, the velocity gradient in Equation (4.22) can be obtained.

It is important to note here that the reconstruction (4.22) of the non-equilibrium distribution function is based on a Hermite regularization, as previously discussed in Section 3.4.1, so the present reconstruction method is expected to be more consistent with the RLBM scheme.

### 4.7.3 Algorithm

The proposed reconstruction method is to substitute the original one, while the rest ingredients of the free-surface model stay unchanged. The present algorithm is summarized as

---

**Algorithm:** FS-RLBM with new reconstruction procedure

---

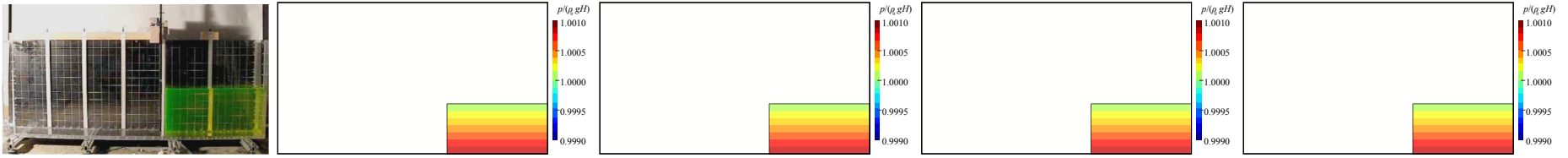
**Require:**  $f_i(\mathbf{x}, t^n)$ ,  $\rho(\mathbf{x}, t^n)$ ,  $\mathbf{u}(\mathbf{x}, t^n)$ ,  $\mathbf{F}(\mathbf{x}, t^n)$ ,  $\alpha(\mathbf{x}, t^n)$ ,  $m(\mathbf{x}, t^n)$  and *flag* array from the previous time-step

1. For liquid and interface cells, implement the collision and streaming procedure (i.e. from Step.1 to Step.6 in the RLBM algorithm shown in Section 3.2),
  2. For interface cells, compute the missing distribution functions by Equation (4.11),
  3. For liquid cells, adapt  $\rho(\mathbf{x}, t^{n+1})$ ,  $\mathbf{u}(\mathbf{x}, t^{n+1})$  by Equation (2.69),
  4. Extrapolate  $\rho(\mathbf{x}, t^{n+1})$ ,  $\mathbf{u}(\mathbf{x}, t^{n+1})$  by Equation (4.25) for interface cells,
  5. Reconstruct the distribution functions for interface cells by Equation (4.21-4.23),
  6. Adapt  $\rho(\mathbf{x}, t^{n+1})$ ,  $\mathbf{u}(\mathbf{x}, t^{n+1})$  by Equation (2.69) for interface cells,
  7. Follow Step.4 to Step.10 in Algorithm 4.5,
  8. Goto Step.1 for the next time-step.
- 

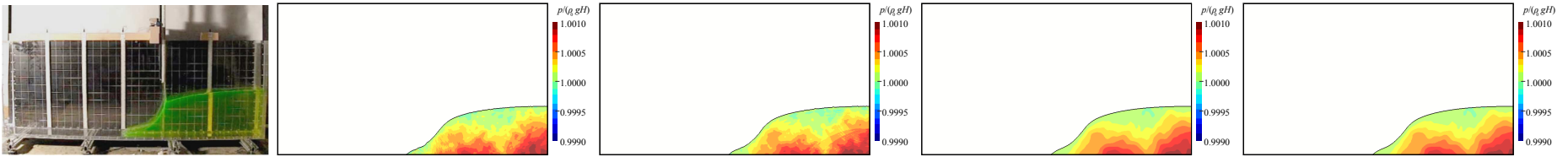
### 4.7.4 Validation

The new method is tested in the dambreak test-case, where the initialization of the simulation is as the same as that in Section 4.6.2. For comparison, the present modified free-surface model and the original one are employed with the standard SRT-LBM and the RLBM, respectively. Besides, in order to focus on the influence of the free-surface models, the Reynolds number in the simulation is reduced to  $Re = 3200$  so that the standard SRT-LBM can stay stable.

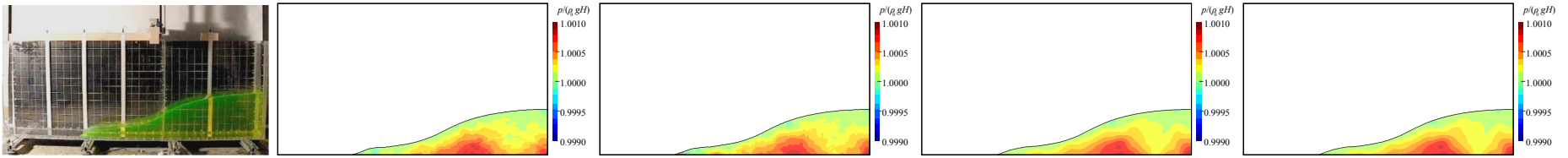
Several snapshots of the numerical results are exhibited in Figure 4.23. One can see that the dambreak flow is reproduced successfully by the four schemes, and the numerical flows are very similar to the experimental one although the Reynolds number is largely reduced in the simulation. From the pressure contours, one can observe that the present model performs as well as the original one, if not better, and it is the regularization procedure in the RLBM which dominates in smoothing the pressure field.



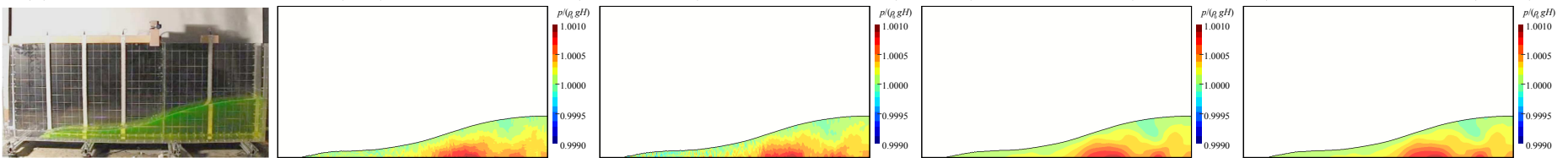
(a)  $t = 0.0\text{ms}$ : Experiment (left), FS1-SRT-LBM (middle left), FS2-SRT-LBM (middle), FS1-RLBM (middle right), and FS2-RLBM (right).



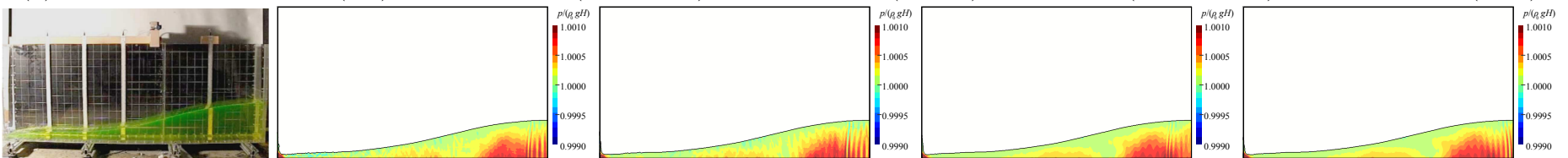
(b)  $t = 159.9\text{ms}$ : Experiment (left), FS1-SRT-LBM (middle left), FS2-SRT-LBM (middle), FS1-RLBM (middle right), and FS2-RLBM (right).



(c)  $t = 276.6\text{ms}$ : Experiment (left), FS1-SRT-LBM (middle left), FS2-SRT-LBM (middle), FS1-RLBM (middle right), and FS2-RLBM (right).



(d)  $t = 373.3\text{ms}$ : Experiment (left), FS1-SRT-LBM (middle left), FS2-SRT-LBM (middle), FS1-RLBM (middle right), and FS2-RLBM (right).



(e)  $t = 449.9\text{ms}$ : Experiment (left), FS1-SRT-LBM (middle left), FS2-SRT-LBM (middle), FS1-RLBM (middle right), and FS2-RLBM (right).

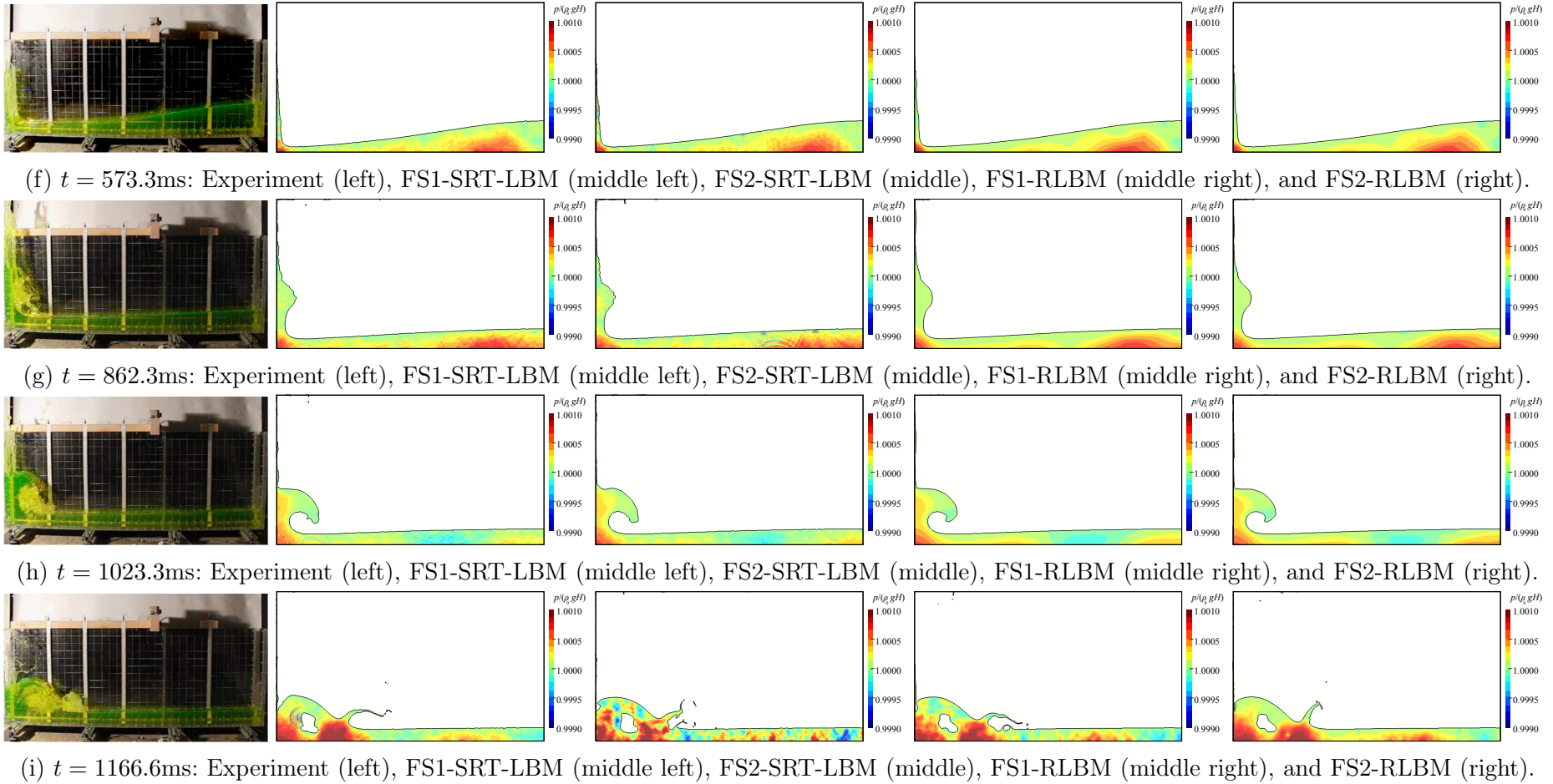


Figure 4.23 – Snapshots of the free-surface profiles and the pressure fields at time 0.0, 159.9, 276.6, 373.3, 449.9, 573.3, 862.3, 1023.3, 1166.6ms. The exhibited results are from the experiment (left), the original model with SRT-LBM (middle left, marked as FS1-SRT-LBM), the present model with SRT-LBM (middle, marked as FS2-SRT-LBM), the original model with RLBM (middle right, marked as FS1-RLBM) and the present model with RLBM (right, marked as FS2-RLBM).

However, if we zoom in a little by extracting the pressure signals at positions P1, P2, P3 and P4 (the coordinates of these positions can be found in Section 4.6.2), the advantage of the present model can be seen. Figure 4.24 gives the pressure signals recorded with the four schemes, where the results of both free-surface models with the standard SRT-LBM are shown in the left panels, and those of the two free-surface models with the RLBM are plotted in the right panels.

In association with the standard SRT-LBM, the present model provides results that are close to the results with the original model: the pressure oscillations are in the same range. As a contrast, in the RLBM framework, although the pressure oscillations have already been remarkably reduced by the RLBM, the present model is able to achieve even better results. Indeed, this improvement is not that prominent in the pressure curves, but this is due to the fact that the number of interface cells that are caught in the aforementioned dilemmas of the original model, is of a relatively small percentage during the whole calculation. Fairly speaking, one is still able to conclude that the present free-surface model is more consistent with the RLBM.

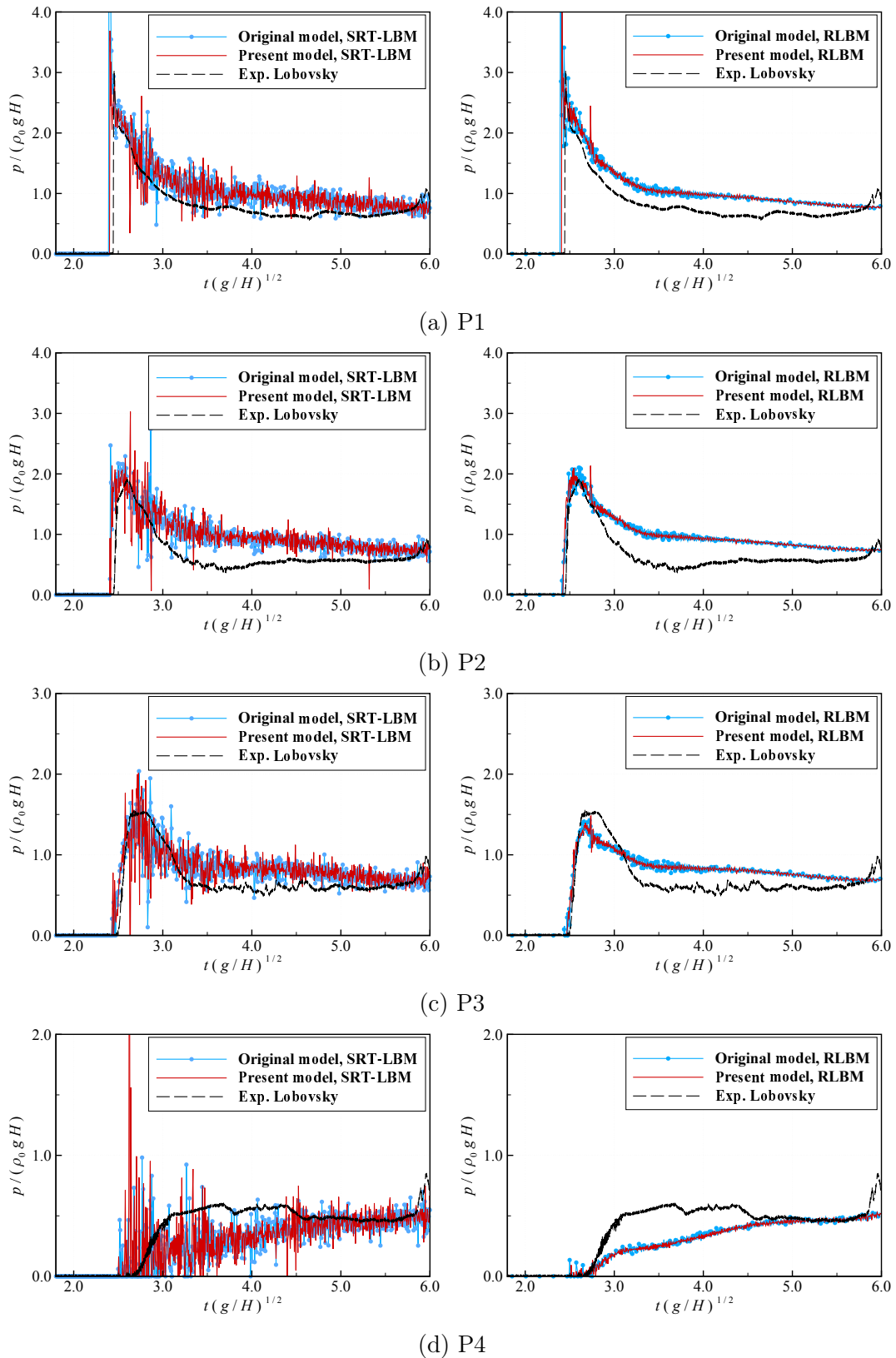
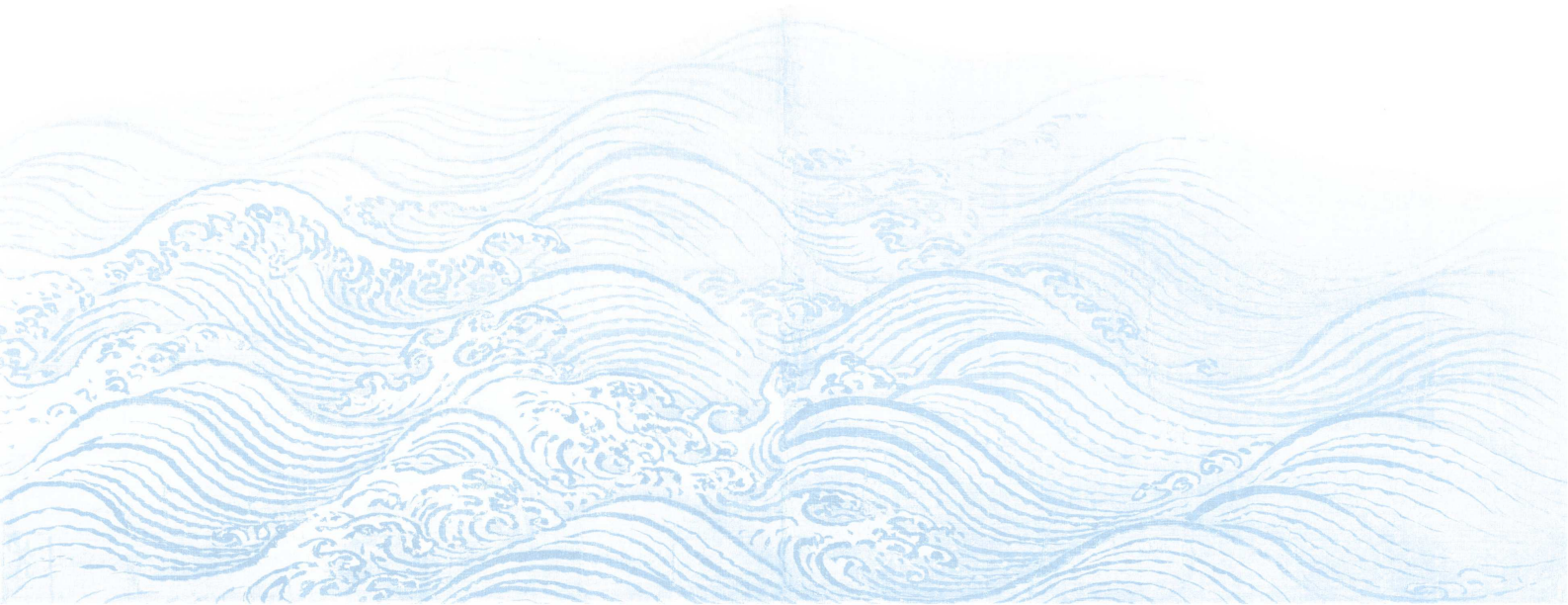


Figure 4.24 – Pressure signals at P1, P2, P3 and P4 positions, obtained from the original model with SRT-LBM, the present model with SRT-LBM, the original model with RLBM and the present model with RLBM.

# Chapter 5

## Conslusions and perspectives



## 5.1 Conclusions

The principal object of this thesis is to assess the applicability of the lattice Boltzmann method (LBM) to the free-surface flows with marine engineering problems as long-term objective. Taking into account the existence of extreme ocean conditions, the desired numerical method is expected to include a robust free-surface model for simulating large deformations of the interface, and to be stable for high Reynolds number flows. Aiming at such goal, the thesis can be concluded from the following four aspects.

Firstly, a comprehensive review has been made in Chapter 1 on the free-surface lattice Boltzmann (LB) models and the LB stabilization techniques. Between the two categories of free-surface LB models, the multi-phase LB models are usually easy to implement due to their global operations, but the insuperable difficulty is the large density ratio at the water-air interface, which is only asymptotically approached by few published articles. On the contrary, the single-phase model is born to be friendly to large density ratios; as a return it requires much work on the treatment of the free-surface boundary. As for the stabilization techniques, the regularized LBM (RLBM) is considered to be the most appealing one among the various possibilities, since it is more consistent with the Hermite representation of LBM and consequently requests the smallest modification to the standard LBM. In this way, an optimized strategy for simulating high-Reynolds-number free-surface flow has been made, which is to employ a volume-of-fluid (VOF) based single-phase LB model within the RLBM.

The second part, consisting of Chapters 2 and 3, elaborately reformulates the underlying theory of how the LBM tackles incompressible fluid flows. By adopting a truncated Hermite expansion and making use of the Gauss-Hermite quadrature, the concept of the LBM is stated as using a minimized discrete velocity set to include the same amount of macroscopic hydrodynamic information as the continuous Boltzmann equation. Besides, the Navier-Stokes equations are proved to be recovered from the LB equation through a detailed multi-scale analysis. From this perspective, the RLBM is explained as a Hermite regularization of the distribution function onto the Hilbert subspace spanned by the first several Hermite basis elements. Specifically, it is pointed out that the starting order of the regularization should vary for different force models, which is verified on a Poiseuille flow simulation. Afterwards, two simulations are carried out: both the Taylor-Green vortex and the lid-driven cavity flows show that the RLBM has 2<sup>nd</sup>-order accuracy, and that the benefits in accuracy outshines its relatively large demand of CPU time. Furthermore, on the lid-driven cavity flow, it is also shown how the RLBM permit to get a drastic reduction of the spurious pressure oscillations introduced from

the boundary treatment and the intrinsic instability of the standard LBM at high Reynolds numbers.

In the third part, in Chapter 4, the implementation of the adopted VOF-based single-phase free-surface model in the RLBM is described. In addition to the basic ingredients of the original model [94], some additional techniques that ensure the robustness are highlighted, including the adapted criteria of flag change, the dos and don'ts of the cell flag evolution, and the normal vector based distribution rule of the excess cell mass. The adopted model with the RLBM is examined in two test-cases. Good results have been obtained for the viscous standing wave test-case, compared with the analytical solution, and it is validated that the truncation of high-order components during the regularization does not generate extra numerical dissipation. In the following test-case, the dambreak flow has been successfully reproduced, and the pressure signals are very well compared with benchmark experiment data. It is shown that the RLBM can afford large Reynolds number dambreak flows, for it remarkably reduces the pressure oscillation and consequently maintains smooth free-surface profiles and pressure fields. Shortly speaking, the RLBM with the adopted free-surface model does provide a reliable way for simulating free-surface flows.

Lastly, the original free-surface model is modified with a new reconstruction method for the distribution functions at the interface, which is presented in the latter part of Chapter 4. The dilemmas of determining how many distribution functions should be reconstructed, that the original model encounters, are exemplified at first. In order to get rid of these awkward situations, a new reconstruction method is proposed, which computes the equilibrium distribution function from macroscopic variables that are extrapolated from the neighboring liquid cells by an inverse distance weighting, and obtains the non-equilibrium part through a regularization procedure. Such reconstruction method is proven to be more consistent with the RLBM, as expected, as it provides the smallest level of spurious pressure oscillation in the dambreak test-case.

## 5.2 Perspectives

Based on what has been achieved in this thesis work, our present in-house LB solver can be further extended from the following several perspectives.

Firstly, in terms of accelerating the calculation, the present code will be armed with parallel computing technique. Noting that the adopted free-surface model involves frequent searching operation and information exchange between lattice cells, this part should be carefully considered in order to reach optimized acceleration ratio. Furthermore, other advanced acceleration techniques may be applied,

such as parallel GPU implementation [32].

Secondly, for large scale test-cases and long-term simulation, developing adaptive mesh refinement and adaptive time step modules can be beneficial, since they may get rid of the constraint of the uniform time-space lattice in the standard LBM and thus improve the efficiency.

Thirdly, in the long-term future where real marine engineering applications are the targets, some necessary models need to be implemented to the present solver, including the fluid-structure interaction. The very first step could be developing a hybrid solver of the immersed boundary (IB) method and the LBM [42, 114] and introducing the present free-surface model into it. Then, starting from some simple test-cases such as the flow past a full immersed object or fixed moving rigid body, one could step by step simulate freely moving floating body, simple-shaped ship resistance, multiple floating body, etc., and eventually study real marine application like moored floating platforms, floating or immersed wave energy converter farm, and so on.

# Appendix A

## Some mathematical tools

### A.1 Operations on vectors and matrices

#### A.1.1 Dot product of two vectors

The dot product of two vectors  $\mathbf{a} = [a_1, a_2, \dots, a_n]$  and  $\mathbf{b} = [b_1, b_2, \dots, b_n]$ , marked as  $c = \mathbf{a} \cdot \mathbf{b}$ , is a scalar calculated as

$$c = \sum_{i=1}^n a_i b_i. \quad (\text{A.1})$$

Specially, the dot product of a vector  $\mathbf{a}$  and itself is marked as  $\mathbf{a}^2 = \mathbf{a} \cdot \mathbf{a}$  in the thesis.

#### A.1.2 Dyadic product of two vectors

The dyadic product of two vectors  $\mathbf{a} = [a_1, a_2, \dots, a_m]$  and  $\mathbf{b} = [b_1, b_2, \dots, b_n]$ , marked as  $\mathbf{c} = \mathbf{a}\mathbf{b}$ , is a  $[m \times n]$  matrix where its element  $c_{ij}$  is calculated as

$$c_{ij} = a_i b_j. \quad (\text{A.2})$$

#### A.1.3 Double dot product of two matrices

The double dot product of two  $[m \times n]$  matrices  $\mathbf{A}$  and  $\mathbf{B}$ , marked as  $c = \mathbf{A} : \mathbf{B}$ , is a scalar calculated as

$$c = \sum_{i=1}^m \sum_{j=1}^n A_{ij} B_{ij}. \quad (\text{A.3})$$

Specifically, if  $\mathbf{A}$  and  $\mathbf{B}$  are vectors, the double dot product shall degenerate into a dyadic product. Moreover, if matrix  $\mathbf{A}$  and  $\mathbf{B}$  are respectively the dyadic product of two pairs of  $n$ -rank vectors, i.e.,  $\mathbf{A} = \mathbf{a}\mathbf{b}$  and  $\mathbf{B} = \mathbf{c}\mathbf{d}$ , then the following

equation can be obtained based on Equation (A.1), (A.2) and (A.3)

$$\mathbf{ab} : \mathbf{cd} = (\mathbf{a} \cdot \mathbf{c}) (\mathbf{b} \cdot \mathbf{d}). \quad (\text{A.4})$$

## A.2 Velocity moments of functions in a special form

In addition, for any function, defined on the  $D2Q9$  lattice, that takes the following form,

$$\phi_i = w_i \left[ A + \frac{\mathbf{B} \cdot \boldsymbol{\xi}_i}{c_s^2} + \frac{\mathbf{C} : (\boldsymbol{\xi}_i \boldsymbol{\xi}_i - c_s^2 \mathbf{I})}{2c_s^4} \right], \quad (\text{A.5})$$

its first several velocity moments can be easily computed as

$$\left\{ \begin{array}{l} \sum_i \phi_i = A, \\ \sum_i \boldsymbol{\xi}_i \phi_i = \mathbf{B}, \\ \sum_i \boldsymbol{\xi}_i \boldsymbol{\xi}_i \phi_i = A c_s^2 \mathbf{I} + \frac{\mathbf{C} + \mathbf{C}^T}{2}. \end{array} \right. \quad (\text{A.6})$$

Here  $w_i$ ,  $\boldsymbol{\xi}_i$  and  $c_s$  are respectively the weights, the lattice speeds and the sound speed in the  $D2Q9$  lattice.

## A.3 Gauss-Hermite quadrature

For any function  $\phi(x)$ , the integral in the form of  $\int_{-\infty}^{+\infty} \phi(x) e^{-x^2}$  can be approximated by the Gauss-Hermite quadrature as

$$\int_{-\infty}^{+\infty} \phi(x) e^{-x^2} \approx \sum_{i=1}^n w_i \phi(x_i), \quad (\text{A.7})$$

where  $n$  is the number of the chosen sample points,  $x_i$  with  $(i = 1, 2, \dots, n)$  are the roots of the Hermite polynomial  $\mathcal{H}_n(x)$ , and the associated weights are given as

$$w_i = \frac{2^{n-1} n! \sqrt{\pi}}{n^2 [\mathcal{H}_{n-1}(x_i)]^2}. \quad (\text{A.8})$$

## A.4 Hermite expansion by Hermite polynomials

For any function  $\phi(\boldsymbol{\xi})$  that is square integrable, it can be expanded by the Hermite polynomials as

$$\phi(\boldsymbol{\xi}) = \omega(\boldsymbol{\xi}) \sum_{n=0}^{\infty} \frac{1}{n!} \mathbf{a}^{(n)} : \mathcal{H}^{(n)}(\boldsymbol{\xi}), \quad (\text{A.9})$$

where  $\omega(\boldsymbol{\xi})$  is the weighting function,  $\mathcal{H}^{(n)}(\boldsymbol{\xi})$  is the  $n^{\text{th}}$ -order Hermite polynomial, and  $\mathbf{a}^{(n)}$  is the corresponding expanding coefficient. Respectively, the weighting function  $\omega(\boldsymbol{\xi})$  is given as

$$\omega(\boldsymbol{\xi}) = \frac{1}{(2\pi)^{D/2}} \exp\left(-\frac{\boldsymbol{\xi} \cdot \boldsymbol{\xi}}{2}\right), \quad (\text{A.10})$$

the  $n^{\text{th}}$ -order Hermite polynomial  $\mathcal{H}^{(n)}(\boldsymbol{\xi})$  is

$$\mathcal{H}^{(n)}(\boldsymbol{\xi}) = \frac{(-1)^n}{\omega(\boldsymbol{\xi})} \nabla_{\boldsymbol{\xi}}^n \omega(\boldsymbol{\xi}), \quad (\text{A.11})$$

and the corresponding expanding coefficient  $\mathbf{a}^{(n)}(\boldsymbol{\xi})$  is computed as

$$\mathbf{a}^{(n)} = \int \phi(\boldsymbol{\xi}) \mathcal{H}^{(n)}(\boldsymbol{\xi}) d\boldsymbol{\xi}. \quad (\text{A.12})$$

It is important to note that the Hermite polynomials are mutually orthogonal in a way that

$$\int \omega(\boldsymbol{\xi}) \mathcal{H}^{(m)}(\boldsymbol{\xi}) \mathcal{H}^{(n)}(\boldsymbol{\xi}) d\boldsymbol{\xi} = \begin{cases} 0, & (\text{if } m \neq n) \\ 1. & (\text{if } m = n) \end{cases} \quad (\text{A.13})$$



# Appendix B

## Multi-relaxation-time collision model

As an alternative collision operator, the multi-relaxation-time (MRT) collision model is introduced to reduce the numerical instability of the SRT scheme under high Reynolds number conditions. The MRT model was designed with an idea of relaxing different distribution function momenta to their equilibrium states in different rates. A standard MRT equation can be expressed as:

$$f_i(\mathbf{x} + \mathbf{e}_i dt, t + dt) - f_i(\mathbf{x}, t) = -\tilde{\Lambda}_{ij} [f_j - f_j^{\text{eq}}] \quad (\text{B.1})$$

where Einstein notation is adopted.  $\tilde{\Lambda} = \mathbf{M}^{-1} \mathbf{\Lambda} \mathbf{M}$  is the collision matrix, in which  $\mathbf{M}$  is an orthogonal transformation matrix. In  $D2Q9$  lattice, the transformation matrix is given as:

$$\mathbf{M} = \begin{bmatrix} 1 & 1 & 1 & 1 & 1 & 1 & 1 & 1 & 1 \\ -4 & -1 & -1 & -1 & -1 & 2 & 2 & 2 & 2 \\ 4 & -2 & -2 & -2 & -2 & 1 & 1 & 1 & 1 \\ 0 & 1 & 0 & -1 & 0 & 1 & -1 & -1 & 1 \\ 0 & -2 & 0 & 2 & 0 & 1 & -1 & -1 & 1 \\ 0 & 0 & 1 & 0 & -1 & 1 & 1 & -1 & -1 \\ 0 & 0 & -2 & 0 & 2 & 1 & 1 & -1 & -1 \\ 0 & 1 & -1 & 1 & -1 & 0 & 0 & 0 & 0 \\ 0 & 0 & 0 & 0 & 0 & 1 & -1 & 1 & -1 \end{bmatrix} \quad (\text{B.2})$$

Subsequently the distribution functions are projected onto the moment space:

$$\mathbf{m} = \mathbf{M} \mathbf{f} = (\rho, e, \varsigma, j_x, q_x, j_y, q_y, p_{xx}, p_{xy})^T \quad (\text{B.3})$$

The corresponding equilibrium moments are:

$$\begin{aligned}
 \mathbf{m}^{\text{eq}} &= (\rho, e^{\text{eq}}, \varsigma^{\text{eq}}, j_x, q_x^{\text{eq}}, j_y, q_y^{\text{eq}}, p_{xx}^{\text{eq}}, p_{xy}^{\text{eq}})^{\text{T}} \\
 &= \rho (1, -2 + 3|\mathbf{v}|^2, 1 - 3|\mathbf{v}|^2, v_x, -v_x, v_y, -v_y, v_x^2 - v_y^2, v_x v_y)^{\text{T}} \quad (\text{B.4})
 \end{aligned}$$

where  $\mathbf{f} = (f_1, f_2, \dots, f_8)^{\text{T}}$ ,  $|\mathbf{v}|^2 = \mathbf{v} \cdot \mathbf{v}$ ,  $e$  is the energy mode,  $\varsigma$  is related to the energy square,  $(j_x, j_y)$  are the momentum components,  $(q_x, q_y)$  correspond to energy flux.

# Appendix C

## A choice between an open-source software and an in-house code

Before starting a numerical research in the field of computational fluid dynamics (CFD), one should choose an appropriate numerical tool at first. The various numerical tools based on the lattice Boltzmann method (LBM) lies in two categories, that are either to use an open-source LBM solver like PALABOS <sup>(i)</sup>, OpenLB <sup>(ii)</sup> and waLBerla <sup>(iii)</sup>, or to develop one's own in-house code. The author made the decision after spending more than six months in the beginning of this study, trying to use the open-source PALABOS.

The advantages of PALABOS can be illustrated by showing the following two simple tests. In the first example, see Figure (C.1), which is the flow around an airfoil, the major difficulty for LBM coding can be addressed as the lattice representation of the complex geometry and the implementation of the bounce-back non-slip boundary condition on the airfoil surface. As a contrast, the PALABOS provides embedded modules for allocating the boundary lattice nodes based on the airfoil profile and setting up the bounce-back rule along the complex curve. The second example, see Figure (C.2) which is the Rayleigh-Taylor instability, is more related to the present study, since the multi-phase flow offers an access to the marine free-surface flows if it is capable for simulating large density ratios. Nevertheless, the example showed here is to state that the PALABOS has been equipped with multi-phase modules. Besides, the PALABOS also benefits from its built-in modules for conveniently extracting datas into files.

In one word, the PALABOS might be a powerful tool for those who truly understand the underling mechanisms in the basic modules beneath the simple call statements. However, the configuration of the PALABOS solver with multiple

---

<sup>(i)</sup><http://www.palabos.org>

<sup>(ii)</sup><https://www.openlb.net>

<sup>(iii)</sup><http://walberla.net>

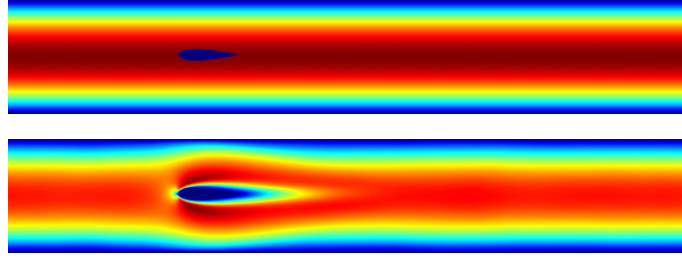


Figure C.1 – Snapshots of the velocity contour of the flow around an airfoil, where the upper one is the initial state.

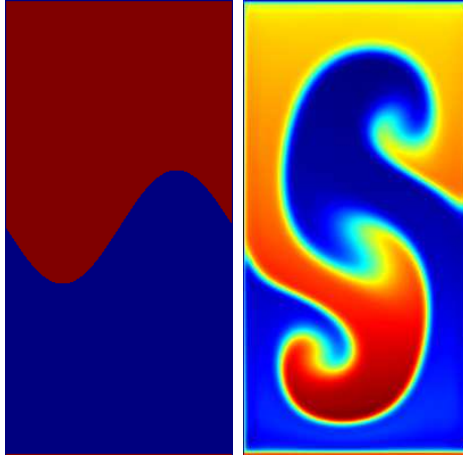


Figure C.2 – Snapshots of the pressure contour of the Rayleigh-Taylor instability, where the left one is the initial state.

layers is very enormous and complex. The author personally find out that it is hard to make changes to the embedded modules. For this subjective reason, it seems to the author that the disadvantages of adopting PALABOS overshadow its advantages, so the author decided to develop an in-house code, which is elaborately explained in the thesis.

# Bibliography

- [1] Takashi Abe. Derivation of the lattice boltzmann method by means of the discrete ordinate method for the boltzmann equation. *Journal of Computational Physics*, 131(1):241–246, 1997.
- [2] Regina Ammer, Matthias Markl, Ulric Ljungblad, Carolin Körner, and Ulrich Råde. Simulating fast electron beam melting with a parallel thermal free surface lattice boltzmann method. *Computers & Mathematics with Applications*, 67(2):318–330, 2014.
- [3] Daniela Anderl, Simon Bogner, Cornelia Rauh, Ulrich Råde, and Antonio Delgado. Free surface lattice boltzmann with enhanced bubble model. *Computers & Mathematics with Applications*, 67(2):331–339, 2014.
- [4] S Ansumali, IV Karlin, Ch E Frouzakis, and KB Boulouchos. Entropic lattice boltzmann method for microflows. *Physica A: Statistical Mechanics and its Applications*, 359:289–305, 2006.
- [5] Santosh Ansumali and Iliya V Karlin. Single relaxation time model for entropic lattice boltzmann methods. *Physical Review E*, 65(5):056312, 2002.
- [6] Elham Attar and Carolin Körner. Lattice boltzmann method for dynamic wetting problems. *Journal of colloid and interface science*, 335(1):84–93, 2009.
- [7] Elham Attar and Carolin Körner. Lattice boltzmann model for thermal free surface flows with liquid–solid phase transition. *International Journal of Heat and Fluid Flow*, 32(1):156–163, 2011.
- [8] Jie Bao and Laura Schaefer. Lattice boltzmann equation model for multi-component multi-phase flow with high density ratios. *Applied Mathematical Modelling*, 37(4):1860–1871, 2013.
- [9] A Bauereiß, T Scharowsky, and C Körner. Defect generation and propagation mechanism during additive manufacturing by selective beam melting. *Journal of Materials Processing Technology*, 214(11):2522–2528, 2014.

- [10] O Behrend, R Harris, and PB Warren. Hydrodynamic behavior of lattice boltzmann and lattice bhatnagar-gross-krook models. *Physical Review E*, 50(6):4586, 1994.
- [11] Roberto Benzi, Sauro Succi, and Massimo Vergassola. The lattice boltzmann equation: theory and applications. *Physics Reports*, 222(3):145–197, 1992.
- [12] Prabhu Lal Bhatnagar, Eugene P Gross, and Max Krook. A model for collision processes in gases. i. small amplitude processes in charged and neutral one-component systems. *Physical review*, 94(3):511, 1954.
- [13] Bruce M Boghosian, Peter J Love, Peter V Coveney, Iliya V Karlin, Sauro Succi, and Jeffrey Yepez. Galilean-invariant lattice-boltzmann models with h theorem. *Physical Review E*, 68(2):025103, 2003.
- [14] Simon Bogner, Regina Ammer, and Ulrich Rude. Boundary conditions for free interfaces with the lattice boltzmann method. *Journal of Computational Physics*, 297:1–12, 2015.
- [15] Simon Bogner, Jens Harting, and Ulrich Rude. Direct simulation of liquid–gas–solid flow with a free surface lattice boltzmann method. *International Journal of Computational Fluid Dynamics*, 31(10):463–475, 2017.
- [16] Simon Bogner and Ulrich Rude. Simulation of floating bodies with the lattice boltzmann method. *Computers & Mathematics with Applications*, 65(6):901–913, 2013.
- [17] Simon Bogner, Ulrich Rude, and Jens Harting. Curvature estimation from a volume-of-fluid indicator function for the simulation of surface tension and wetting with a free-surface lattice boltzmann method. *Physical Review E*, 93(4):043302, 2016.
- [18] O Botella and R Peyret. Benchmark spectral results on the lid-driven cavity flow. *Computers & Fluids*, 27(4):421–433, 1998.
- [19] M’hamed Bouzidi, Mouaouia Firdaouss, and Pierre Lallemand. Momentum transfer of a boltzmann-lattice fluid with boundaries. *Physics of fluids*, 13(11):3452–3459, 2001.
- [20] AJ Briant, AJ Wagner, and JM Yeomans. Lattice boltzmann simulations of contact line motion. i. liquid-gas systems. *Physical Review E*, 69(3):031602, 2004.

- 
- [21] Federico Brogi, Orestis Malaspinas, Bastien Chopard, and Costanza Bonadonna. Hermite regularization of the lattice boltzmann method for open source computational aeroacoustics. *The Journal of the Acoustical Society of America*, 142(4):2332–2345, 2017.
- [22] Nianzheng Cao, Shiyi Chen, Shi Jin, and Daniel Martinez. Physical symmetry and lattice symmetry in the lattice boltzmann method. *Physical Review E*, 55(1):R21, 1997.
- [23] Hudong Chen. Volumetric formulation of the lattice boltzmann method for fluid dynamics: Basic concept. *Physical Review E*, 58(3):3955, 1998.
- [24] Hudong Chen, Shiyi Chen, and William H Matthaeus. Recovery of the navier-stokes equations using a lattice-gas boltzmann method. *Physical Review A*, 45(8):R5339, 1992.
- [25] Li Chen, Qinjun Kang, Yutong Mu, Ya-Ling He, and Wen-Quan Tao. A critical review of the pseudopotential multiphase lattice boltzmann model: Methods and applications. *International Journal of Heat and Mass Transfer*, 76:210–236, 2014.
- [26] Shiyi Chen and Gary D Doolen. Lattice boltzmann method for fluid flows. *Annual review of fluid mechanics*, 30(1):329–364, 1998.
- [27] Shiyi Chen, Zheng Wang, Xiaowen Shan, and Gary D Doolen. Lattice boltzmann computational fluid dynamics in three dimensions. *Journal of Statistical Physics*, 68(3-4):379–400, 1992.
- [28] Ming Cheng, Jinsong Hua, and Jing Lou. Simulation of bubble–bubble interaction using a lattice boltzmann method. *Computers & Fluids*, 39(2):260–270, 2010.
- [29] SS Chikatamarla, Santosh Ansumali, and Ilya V Karlin. Entropic lattice boltzmann models for hydrodynamics in three dimensions. *Physical review letters*, 97(1):010201, 2006.
- [30] SS Chikatamarla, IV Karlin, et al. Entropic lattice boltzmann method for multiphase flows. *Physical review letters*, 114(17):174502, 2015.
- [31] Andrea Colagrossi, Matteo Antuono, Antonio Souto-Iglesias, and David Le Touzé. Theoretical analysis and numerical verification of the consistency of viscous smoothed-particle-hydrodynamics formulations in simulating free-surface flows. *Physical Review E*, 84(2):026705, 2011.

- [32] Georges-Henri Cottet, Jean-Matthieu Etancelin, Franck Pérignon, Christophe Picard, Florian De Vuyst, and Christophe Labourdette. Is gpu the future of scientific computing?[le gpu est-il le futur du calcul scientifique?]. In *Annales mathématiques Blaise Pascal*, volume 20, pages 75–99, 2013.
- [33] Paul J Dellar. Bulk and shear viscosities in lattice boltzmann equations. *Physical Review E*, 64(3):031203, 2001.
- [34] Paul J Dellar. An interpretation and derivation of the lattice boltzmann method using strang splitting. *Computers & Mathematics with Applications*, 65(2):129–141, 2013.
- [35] Dominique d’Humières. Generalized lattice-boltzmann equations. *Rarefied gas dynamics*, 1992.
- [36] Dominique d’Humières. Multiple-relaxation-time lattice boltzmann models in three dimensions. *Philosophical Transactions of the Royal Society of London A: Mathematical, Physical and Engineering Sciences*, 360(1792):437–451, 2002.
- [37] Dominique d’Humières, Pierre Lallemand, and Uriel Frisch. Lattice gas models for 3d hydrodynamics. *EPL (Europhysics Letters)*, 2(4):291, 1986.
- [38] François Dubois, Tony Fevrier, and Benjamin Graille. Lattice boltzmann schemes with relative velocities. *Communications in Computational Physics*, 17(4):1088–1112, 2015.
- [39] Abbas Fakhari and Mohammad H Rahimian. Phase-field modeling by the method of lattice boltzmann equations. *Physical Review E*, 81(3):036707, 2010.
- [40] Giacomo Falcucci, Stefano Ubertini, Chiara Biscarini, Silvia Di Francesco, Daniele Chiappini, Silvia Palpacelli, Alessandro De Maio, and Sauro Succi. Lattice boltzmann methods for multiphase flow simulations across scales. *Communications in Computational Physics*, 9(2):269–296, 2011.
- [41] Hongli Fan, Raoyang Zhang, and Hudong Chen. Extended volumetric scheme for lattice boltzmann models. *Physical Review E*, 73(6):066708, 2006.
- [42] Julien Favier, Alistair Revell, and Alfredo Pinelli. A lattice boltzmann-immersed boundary method to simulate the fluid interaction with moving and slender flexible objects. *Journal of Computational Physics*, 261:145–161, 2014.

- 
- [43] Olga Filippova and Dieter Hänel. Grid refinement for lattice-bgk models. *Journal of Computational physics*, 147(1):219–228, 1998.
- [44] Uriel Frisch, Dominique d’Humières, Brosl Hasslacher, Pierre Lallemand, Yves Pomeau, and Jean-Pierre Rivet. Lattice gas hydrodynamics in two and three dimensions. Technical report, Los Alamos National Lab., NM (USA); Observatoire de Nice, 06 (France); Ecole Normale Supérieure, 75-Paris (France), 1986.
- [45] Uriel Frisch, Brosl Hasslacher, and Yves Pomeau. Lattice-gas automata for the navier-stokes equation. *Physical review letters*, 56(14):1505, 1986.
- [46] Martin Geier, Andreas Greiner, and Jan G Korvink. Cascaded digital lattice boltzmann automata for high reynolds number flow. *Physical Review E*, 73(6):066705, 2006.
- [47] UKNG Ghia, Kirti N Ghia, and CT Shin. High-re solutions for incompressible flow using the navier-stokes equations and a multigrid method. *Journal of computational physics*, 48(3):387–411, 1982.
- [48] Robert A Gingold and Joseph J Monaghan. Smoothed particle hydrodynamics: theory and application to non-spherical stars. *Monthly notices of the royal astronomical society*, 181(3):375–389, 1977.
- [49] Irina Ginzbourg and D d’Humières. Local second-order boundary methods for lattice boltzmann models. *Journal of Statistical Physics*, 84(5-6):927–971, 1996.
- [50] Irina Ginzburg. A free-surface lattice boltzmann method for modelling the filling of expanding cavities by bingham fluids. *Philosophical Transactions of the Royal Society of London A: Mathematical, Physical and Engineering Sciences*, 360(1792):453–466, 2002.
- [51] Irina Ginzburg. Equilibrium-type and link-type lattice boltzmann models for generic advection and anisotropic-dispersion equation. *Advances in water resources*, 28(11):1171–1195, 2005.
- [52] Irina Ginzburg. Generic boundary conditions for lattice boltzmann models and their application to advection and anisotropic dispersion equations. *Advances in Water Resources*, 28(11):1196–1216, 2005.
- [53] Irina Ginzburg. Variably saturated flow described with the anisotropic lattice boltzmann methods. *Computers & fluids*, 35(8-9):831–848, 2006.

- [54] Irina Ginzburg. Lattice boltzmann modeling with discontinuous collision components: Hydrodynamic and advection-diffusion equations. *Journal of Statistical Physics*, 126(1):157–206, 2007.
- [55] Irina Ginzburg and Dominique d’Humières. Multireflection boundary conditions for lattice boltzmann models. *Physical Review E*, 68(6):066614, 2003.
- [56] Irina Ginzburg and Konrad Steiner. Lattice boltzmann model for free-surface flow and its application to filling process in casting. *Journal of Computational Physics*, 185(1):61–99, 2003.
- [57] Irina Ginzburg, Frederik Verhaeghe, and Dominique d’Humières. Two-relaxation-time lattice boltzmann scheme: About parametrization, velocity, pressure and mixed boundary conditions. *Communications in computational physics*, 3(2):427–478, 2008.
- [58] Daryl Grunau, Shiyi Chen, and Kenneth Eggert. A lattice boltzmann model for multiphase fluid flows. *Physics of Fluids A: Fluid Dynamics*, 5(10):2557–2562, 1993.
- [59] Denis Gueyffier, Jie Li, Ali Nadim, Ruben Scardovelli, and Stéphane Zaleski. Volume-of-fluid interface tracking with smoothed surface stress methods for three-dimensional flows. *Journal of Computational physics*, 152(2):423–456, 1999.
- [60] Andrew K Gunstensen, Daniel H Rothman, Stéphane Zaleski, and Gianluigi Zanetti. Lattice boltzmann model of immiscible fluids. *Physical Review A*, 43(8):4320, 1991.
- [61] Zhaoli Guo and Chang Shu. *Lattice Boltzmann method and its applications in engineering*, volume 3. World Scientific, 2013.
- [62] Zhaoli Guo, Chuguang Zheng, and Baochang Shi. Discrete lattice effects on the forcing term in the lattice boltzmann method. *Physical Review E*, 65(4):046308, 2002.
- [63] J Hardy, O De Pazzis, and Yves Pomeau. Molecular dynamics of a classical lattice gas: Transport properties and time correlation functions. *Physical review A*, 13(5):1949, 1976.
- [64] J Hardy, Yves Pomeau, and O De Pazzis. Time evolution of a two-dimensional model system. i. invariant states and time correlation functions. *Journal of Mathematical Physics*, 14(12):1746–1759, 1973.

- 
- [65] Xiaoyi He, Shiyi Chen, and Gary D Doolen. A novel thermal model for the lattice boltzmann method in incompressible limit. *Journal of Computational Physics*, 146(1):282–300, 1998.
- [66] Xiaoyi He, Shiyi Chen, and Raoyang Zhang. A lattice boltzmann scheme for incompressible multiphase flow and its application in simulation of rayleigh–taylor instability. *Journal of Computational Physics*, 152(2):642–663, 1999.
- [67] Xiaoyi He and Li-Shi Luo. Lattice boltzmann model for the incompressible navier–stokes equation. *Journal of statistical Physics*, 88(3-4):927–944, 1997.
- [68] Xiaoyi He and Li-Shi Luo. A priori derivation of the lattice boltzmann equation. *Physical Review E*, 55(6):R6333, 1997.
- [69] Xiaoyi He and Li-Shi Luo. Theory of the lattice boltzmann method: From the boltzmann equation to the lattice boltzmann equation. *Physical Review E*, 56(6):6811, 1997.
- [70] Xiaoyi He, Xiaowen Shan, and Gary D Doolen. Discrete boltzmann equation model for nonideal gases. *Physical Review E*, 57(1):R13, 1998.
- [71] Xiaoyi He, Raoyang Zhang, Shiyi Chen, and Gary D Doolen. On the three-dimensional rayleigh–taylor instability. *Physics of Fluids*, 11(5):1143–1152, 1999.
- [72] Xiaoyi He, Qisu Zou, Li-Shi Luo, and Micah Dembo. Analytic solutions of simple flows and analysis of nonslip boundary conditions for the lattice boltzmann bgk model. *Journal of Statistical Physics*, 87(1-2):115–136, 1997.
- [73] F J Higuera and J Jimenez. Boltzmann approach to lattice gas simulations. *EPL (Europhysics Letters)*, 9(7):663, 1989.
- [74] Shuling Hou, J Sterling, Shiyi Chen, and GD Doolen. A lattice boltzmann subgrid model for high reynolds number flows. *arXiv preprint comp-gas/9401004*, 1994.
- [75] Haibo Huang, Manfred Krafczyk, and Xiyun Lu. Forcing term in single-phase and shan-chen-type multiphase lattice boltzmann models. *Physical Review E*, 84(4):046710, 2011.
- [76] Kerson Huang. *Statistical mechanics*, 1987.
- [77] Antonio Huerta, Ted Belytschko, Sonia Fernández-Méndez, Timon Rabczuk, Xiaoying Zhuang, and Marino Arroyo. Meshfree methods. *Encyclopedia of Computational Mechanics Second Edition*, pages 1–38, 2018.

- [78] Morten A Hygum, Iliya V Karlin, and Vladimir N Popok. Free surface entropic lattice boltzmann simulations of film condensation on vertical hydrophilic plates. *International Journal of Heat and Mass Transfer*, 87:576–582, 2015.
- [79] Takaji Inamuro, Nobuharu Konishi, and Fumimaru Ogino. A galilean invariant model of the lattice boltzmann method for multiphase fluid flows using free-energy approach. *Computer physics communications*, 129(1-3):32–45, 2000.
- [80] Takaji Inamuro, Tajima Ogata, S Tajima, and N Konishi. A lattice boltzmann method for incompressible two-phase flows with large density differences. *Journal of Computational physics*, 198(2):628–644, 2004.
- [81] Takaji Inamuro, Takaaki Yokoyama, Kentaro Tanaka, and Motoki Taniguchi. An improved lattice boltzmann method for incompressible two-phase flows with large density differences. *Computers & Fluids*, 137:55–69, 2016.
- [82] Muhammad Izham, Tomohiro Fukui, and Koji Morinishi. Application of regularized lattice boltzmann method for incompressible flow simulation at high reynolds number and flow with curved boundary. *Journal of Fluid Science and Technology*, 6(6):812–822, 2011.
- [83] David Jacqmin. Calculation of two-phase navier–stokes flows using phase-field modeling. *Journal of Computational Physics*, 155(1):96–127, 1999.
- [84] Christian Janssen and Manfred Krafczyk. A lattice boltzmann approach for free-surface-flow simulations on non-uniform block-structured grids. *Computers & Mathematics with Applications*, 59(7):2215–2235, 2010.
- [85] AN Kalarakis, VN Burganos, and AC Payatakes. Galilean-invariant lattice-boltzmann simulation of liquid-vapor interface dynamics. *Physical review e*, 65(5):056702, 2002.
- [86] Iliya V Karlin, Antonio Ferrante, and Hans C Öttinger. Perfect entropy functions of the lattice boltzmann method. *EPL (Europhysics Letters)*, 47(2):182, 1999.
- [87] Iliya V Karlin, Alexander N Gorban, Sauro Succi, and V Boffi. Maximum entropy principle for lattice kinetic equations. *Physical Review Letters*, 81(1):6, 1998.
- [88] Iliya V Karlin and S Succi. Equilibria for discrete kinetic equations. *Physical Review E*, 58(4):R4053, 1998.

- 
- [89] Ilya V Karlin, Fabian Bösch, and SS Chikatamarla. Gibbs' principle for the lattice-kinetic theory of fluid dynamics. *Physical Review E*, 90(3):031302, 2014.
- [90] JMVA Koelman. A simple lattice boltzmann scheme for navier-stokes fluid flow. *EPL (Europhysics Letters)*, 15(6):603, 1991.
- [91] Carolin Körner. Foam formation mechanisms in particle suspensions applied to metal foams. *Materials Science and Engineering: A*, 495(1-2):227–235, 2008.
- [92] Carolin Körner, Elham Attar, and Peter Heinl. Mesoscopic simulation of selective beam melting processes. *Journal of Materials Processing Technology*, 211(6):978–987, 2011.
- [93] Carolin Körner, Andreas Bauereiß, and Elham Attar. Fundamental consolidation mechanisms during selective beam melting of powders. *Modelling and Simulation in Materials Science and Engineering*, 21(8):085011, 2013.
- [94] Carolin Körner, Michael Thies, Torsten Hofmann, Nils Thürey, and Ulrich Rüde. Lattice boltzmann model for free surface flow for modeling foaming. *Journal of Statistical Physics*, 121(1-2):179–196, 2005.
- [95] Seiichi Koshizuka and Yoshiaki Oka. Moving-particle semi-implicit method for fragmentation of incompressible fluid. *Nuclear science and engineering*, 123(3):421–434, 1996.
- [96] Manfred Krafczyk, Jonas Tölke, and Li-Shi Luo. Large-eddy simulations with a multiple-relaxation-time lbe model. *International Journal of Modern Physics B*, 17(01n02):33–39, 2003.
- [97] AL Kupershtokh, DA Medvedev, and DI Karpov. On equations of state in a lattice boltzmann method. *Computers & Mathematics with Applications*, 58(5):965–974, 2009.
- [98] A Kuzmin, AA Mohamad, and S Succi. Multi-relaxation time lattice boltzmann model for multiphase flows. *International Journal of Modern Physics C*, 19(06):875–902, 2008.
- [99] Pierre Lallemand and Li-Shi Luo. Theory of the lattice boltzmann method: Dispersion, dissipation, isotropy, galilean invariance, and stability. *Physical Review E*, 61(6):6546, 2000.

- [100] Jonas Latt and Bastien Chopard. Lattice boltzmann method with regularized non-equilibrium distribution functions. *arXiv preprint physics/0506157*, 2005.
- [101] Jonas Latt and Bastien Chopard. Lattice boltzmann method with regularized pre-collision distribution functions. *Mathematics and Computers in Simulation*, 72(2-6):165–168, 2006.
- [102] Jonas Latt, Bastien Chopard, Orestis Malaspinas, Michel Deville, and Andreas Michler. Straight velocity boundaries in the lattice boltzmann method. *Physical Review E*, 77(5):056703, 2008.
- [103] M Latva-Kokko and Daniel H Rothman. Diffusion properties of gradient-based lattice boltzmann models of immiscible fluids. *Physical Review E*, 71(5):056702, 2005.
- [104] Sébastien Leclaire, Marcelo Reggio, and Jean-Yves Trépanier. Isotropic color gradient for simulating very high-density ratios with a two-phase flow lattice boltzmann model. *Computers & Fluids*, 48(1):98–112, 2011.
- [105] Sébastien Leclaire, Marcelo Reggio, and Jean-Yves Trépanier. Numerical evaluation of two recoloring operators for an immiscible two-phase flow lattice boltzmann model. *Applied Mathematical Modelling*, 36(5):2237–2252, 2012.
- [106] Taehun Lee and Ching-Long Lin. Pressure evolution lattice-boltzmann-equation method for two-phase flow with phase change. *Physical Review E*, 67(5):056703, 2003.
- [107] Taehun Lee and Ching-Long Lin. A stable discretization of the lattice boltzmann equation for simulation of incompressible two-phase flows at high density ratio. *Journal of Computational Physics*, 206(1):16–47, 2005.
- [108] Taehun Lee and Lin Liu. Lattice boltzmann simulations of micron-scale drop impact on dry surfaces. *Journal of Computational Physics*, 229(20):8045–8063, 2010.
- [109] Q Li, Kai Hong Luo, XJ Li, et al. Forcing scheme in pseudopotential lattice boltzmann model for multiphase flows. *Physical Review E*, 86(1):016709, 2012.
- [110] Qing Li, Kai Hong Luo, QJ Kang, YL He, Q Chen, and Q Liu. Lattice boltzmann methods for multiphase flow and phase-change heat transfer. *Progress in Energy and Combustion Science*, 52:62–105, 2016.

- 
- [111] Yanbing Li, Richard Shock, Raoyang Zhang, and Hudong Chen. Numerical study of flow past an impulsively started cylinder by the lattice-boltzmann method. *Journal of Fluid Mechanics*, 519:273–300, 2004.
- [112] Ye Li and Yi-Hsiang Yu. A synthesis of numerical methods for modeling wave energy converter-point absorbers. *Renewable and Sustainable Energy Reviews*, 16(6):4352–4364, 2012.
- [113] Zhe Li, Wenjin Cao, and David Le Touzé. On the coupling of a direct-forcing immersed boundary method and the regularized lattice boltzmann method for fluid-structure interaction. submitted.
- [114] Zhe Li, Julien Favier, Umberto D’Ortona, and Sébastien Poncet. An immersed boundary-lattice boltzmann method for single-and multi-component fluid flows. *Journal of Computational Physics*, 304:424–440, 2016.
- [115] Luo Li-shi. The lattice-gas and lattice boltzmann methods: past, present, and future. 2000.
- [116] James Lighthill and MJ Lighthill. *Waves in fluids*. Cambridge university press, 2001.
- [117] CY Lim, C Shu, XD Niu, and YT Chew. Application of lattice boltzmann method to simulate microchannel flows. *Physics of fluids*, 14(7):2299–2308, 2002.
- [118] Zhong Linhao, Feng Shide, and Gao Shouting. Wind-driven ocean circulation in shallow water lattice boltzmann model. *Advances in Atmospheric Sciences*, 22(3):349–358, 2005.
- [119] SV Lishchuk, CM Care, and I Halliday. Lattice boltzmann algorithm for surface tension with greatly reduced microcurrents. *Physical review E*, 67(3):036701, 2003.
- [120] Haifei Liu, Jian Guo Zhou, and Richard Burrows. Multi-block lattice boltzmann simulations of subcritical flow in open channel junctions. *Computers & Fluids*, 38(6):1108–1117, 2009.
- [121] Haihu Liu, Qinjun Kang, Christopher R Leonardi, Sebastian Schmieschek, Ariel Narváez, Bruce D Jones, John R Williams, Albert J Valocchi, and Jens Harting. Multiphase lattice boltzmann simulations for porous media applications. *Computational Geosciences*, 20(4):777–805, 2016.

- [122] Libor Lobovský, Elkin Botia-Vera, Filippo Castellana, Jordi Mas-Soler, and Antonio Souto-Iglesias. Experimental investigation of dynamic pressure loads during dam break. *Journal of Fluids and Structures*, 48:407–434, 2014.
- [123] Jianhua Lu, Haifeng Han, Baochang Shi, and Zhaoli Guo. Immersed boundary lattice boltzmann model based on multiple relaxation times. *Physical Review E*, 85(1):016711, 2012.
- [124] Li-Shi Luo. Unified theory of lattice boltzmann models for nonideal gases. *Physical review letters*, 81(8):1618, 1998.
- [125] Li-Shi Luo, Wei Liao, Xingwang Chen, Yan Peng, Wei Zhang, et al. Numerics of the lattice boltzmann method: Effects of collision models on the lattice boltzmann simulations. *Physical Review E*, 83(5):056710, 2011.
- [126] Daniel Lycett-Brown and Kai H Luo. Multiphase cascaded lattice boltzmann method. *Computers & Mathematics with Applications*, 67(2):350–362, 2014.
- [127] Orestis Malaspinas. Increasing stability and accuracy of the lattice boltzmann scheme: recursivity and regularization. *arXiv preprint arXiv:1505.06900*, 2015.
- [128] Salvatore Marrone, MAGD Antuono, A Colagrossi, G Colicchio, D Le Touzé, and G Graziani.  $\delta$ -sph model for simulating violent impact flows. *Computer Methods in Applied Mechanics and Engineering*, 200(13-16):1526–1542, 2011.
- [129] Salvatore Marrone, Andrea Colagrossi, Andrea Di Mascio, and David Le Touzé. Analysis of free-surface flows through energy considerations: Single-phase versus two-phase modeling. *Physical Review E*, 93(5):053113, 2016.
- [130] Nicos S Martys, Xiaowen Shan, and Hudong Chen. Evaluation of the external force term in the discrete boltzmann equation. *Physical Review E*, 58(5):6855, 1998.
- [131] Denis Matha, Markus Schlipf, Andrew Cordle, Ricardo Pereira, and Jason Jonkman. Challenges in simulation of aerodynamics, hydrodynamics, and mooring-line dynamics of floating offshore wind turbines. Technical report, National Renewable Energy Lab.(NREL), Golden, CO (United States), 2011.
- [132] Guy R McNamara and Gianluigi Zanetti. Use of the boltzmann equation to simulate lattice-gas automata. *Physical review letters*, 61(20):2332, 1988.

- 
- [133] Renwei Mei, Li-Shi Luo, and Wei Shyy. An accurate curved boundary treatment in the lattice boltzmann method. *Journal of computational physics*, 155(2):307–330, 1999.
- [134] A Montessori, G Falcucci, P Prestininzi, M La Rocca, and S Succi. Regularized lattice bhatnagar-gross-krook model for two-and three-dimensional cavity flow simulations. *Physical Review E*, 89(5):053317, 2014.
- [135] Shiladitya Mukherjee and John Abraham. A pressure-evolution-based multi-relaxation-time high-density-ratio two-phase lattice-boltzmann model. *Computers & fluids*, 36(6):1149–1158, 2007.
- [136] XB Nie, SY Chen, Mark O Robbins, et al. A continuum and molecular dynamics hybrid method for micro-and nano-fluid flow. *Journal of Fluid Mechanics*, 500:55–64, 2004.
- [137] XD Niu, C Shu, YT Chew, and TG Wang. Investigation of stability and hydrodynamics of different lattice boltzmann models. *Journal of statistical physics*, 117(3-4):665–680, 2004.
- [138] Xiao-Dong Niu, Shi-Aki Hyodo, Toshihisa Munekata, and Kazuhiko Suga. Kinetic lattice boltzmann method for microscale gas flows: issues on boundary condition, relaxation time, and regularization. *Physical review E*, 76(3):036711, 2007.
- [139] CM Pooley and K Furtado. Eliminating spurious velocities in the free-energy lattice boltzmann method. *Physical Review E*, 77(4):046702, 2008.
- [140] YH Qian, Dominique d’Humières, and Pierre Lallemand. Lattice bgk models for navier-stokes equation. *EPL (Europhysics Letters)*, 17(6):479, 1992.
- [141] Yue-Hong Qian. Fractional propagation and the elimination of staggered invariants in lattice-bgk models. *International journal of modern physics C*, 8(04):753–761, 1997.
- [142] Yue-Hong Qian, S Succi, and SA Orszag. Recent advances in lattice boltzmann computing. In *Annual reviews of computational physics III*, pages 195–242. World Scientific, 1995.
- [143] Marc B Reider and James D Sterling. Accuracy of discrete-velocity bgk models for the simulation of the incompressible navier-stokes equations. *Computers & fluids*, 24(4):459–467, 1995.

- [144] T Reis and TN Phillips. Lattice boltzmann model for simulating immiscible two-phase flows. *Journal of Physics A: Mathematical and Theoretical*, 40(14):4033, 2007.
- [145] Denis Ricot, Simon Marié, Pierre Sagaut, and Christophe Bailly. Lattice boltzmann method with selective viscosity filter. *Journal of Computational Physics*, 228(12):4478–4490, 2009.
- [146] Michele La Rocca, Claudia Adduce, Valentina Lombardi, Giampiero Sciortino, and Reinhard Hinkelmann. Development of a lattice boltzmann method for two-layered shallow-water flow. *International Journal for Numerical Methods in Fluids*, 70(8):1048–1072, 2012.
- [147] Daniel H Rothman and Jeffrey M Keller. Immiscible cellular-automaton fluids. *Journal of Statistical Physics*, 52(3-4):1119–1127, 1988.
- [148] U Rüde and N Thürey. Free surface lattice-boltzmann fluid simulations with and without level sets. In *Proceedings of Vision, Modeling and Visualization*, pages 199–208, 2004.
- [149] Rick Salmon. The lattice boltzmann method as a basis for ocean circulation modeling. *Journal of Marine Research*, 57(3):503–535, 1999.
- [150] Rick Salmon. Lattice boltzmann solutions of the three-dimensional planetary geostrophic equations. *Journal of Marine Research*, 57(6):847–884, 1999.
- [151] M Sbragaglia, R Benzi, L Biferale, S Succi, K Sugiyama, and F Toschi. Generalized lattice boltzmann method with multirange pseudopotential. *Physical Review E*, 75(2):026702, 2007.
- [152] James Albert Sethian. *Level set methods and fast marching methods: evolving interfaces in computational geometry, fluid mechanics, computer vision, and materials science*, volume 3. Cambridge university press, 1999.
- [153] Xiaowen Shan. Analysis and reduction of the spurious current in a class of multiphase lattice boltzmann models. *Physical Review E*, 73(4):047701, 2006.
- [154] Xiaowen Shan and Hudong Chen. Lattice boltzmann model for simulating flows with multiple phases and components. *Physical Review E*, 47(3):1815, 1993.
- [155] Xiaowen Shan and Hudong Chen. Simulation of nonideal gases and liquid-gas phase transitions by the lattice boltzmann equation. *Physical Review E*, 49(4):2941, 1994.

- 
- [156] Xiaowen Shan and Hudong Chen. A general multiple-relaxation-time boltzmann collision model. *International Journal of Modern Physics C*, 18(04):635–643, 2007.
- [157] Xiaowen Shan and Xiaoyi He. Discretization of the velocity space in the solution of the boltzmann equation. *Physical Review Letters*, 80(1):65, 1998.
- [158] Xiaowen Shan, Xue-Feng Yuan, and Hudong Chen. Kinetic theory representation of hydrodynamics: a way beyond the navier–stokes equation. *Journal of Fluid Mechanics*, 550:413–441, 2006.
- [159] Zi-yuan Shi, Yong-hua Yan, Fan Yan, Yue-hong Qian, and Guo-hui Hu. A lattice boltzmann method for simulation of a three-dimensional drop impact on a liquid film. *Journal of Hydrodynamics*, 20(3):267–272, 2008.
- [160] Joseph Smagorinsky. General circulation experiments with the primitive equations: I. the basic experiment. *Monthly weather review*, 91(3):99–164, 1963.
- [161] James D Sterling and Shiyi Chen. Stability analysis of lattice boltzmann methods. *Journal of Computational Physics*, 123(1):196–206, 1996.
- [162] Sauro Succi. Lattice boltzmann 2038. *EPL (Europhysics Letters)*, 109(5):50001, 2015.
- [163] Sauro Succi. Lattice boltzmann beyond navier-stokes: Where do we stand? In *AIP Conference Proceedings*, volume 1786, page 030001. AIP Publishing, 2016.
- [164] Kai Sun, Tianyou Wang, Ming Jia, and Gang Xiao. Evaluation of force implementation in pseudopotential-based multiphase lattice boltzmann models. *Physica A: Statistical Mechanics and its Applications*, 391(15):3895–3907, 2012.
- [165] Michael R Swift, E Orlandini, WR Osborn, and JM Yeomans. Lattice boltzmann simulations of liquid-gas and binary fluid systems. *Physical Review E*, 54(5):5041, 1996.
- [166] Michael R Swift, WR Osborn, and JM Yeomans. Lattice boltzmann simulation of nonideal fluids. *Physical review letters*, 75(5):830, 1995.
- [167] Naoki Takada, Masaki Misawa, Akio Tomiyama, and Shigeo Hosokawa. Simulation of bubble motion under gravity by lattice boltzmann method. *Journal of nuclear science and technology*, 38(5):330–341, 2001.

- [168] Mohamed Mahdi Tekitek, M Bouzidi, François Dubois, and Pierre Lallemand. Adjoint lattice boltzmann equation for parameter identification. *Computers & fluids*, 35(8-9):805–813, 2006.
- [169] Guido Thömmes, Mohammed Seaïd, and Mapundi K Banda. Lattice boltzmann methods for shallow water flow applications. *International Journal for Numerical Methods in Fluids*, 55(7):673–692, 2007.
- [170] Nils Thürey, Richard Keiser, Mark Pauly, and Ulrich Rüde. Detail-preserving fluid control. In *Proceedings of the 2006 ACM SIGGRAPH/Eurographics symposium on Computer animation*, pages 7–12. Eurographics Association, 2006.
- [171] Nils Thürey, C Körner, and U Rüde. Interactive free surface fluids with the lattice boltzmann method. *Technical Report05-4. University of Erlangen-Nuremberg, Germany*, 2005.
- [172] Nils Thürey, Thomas Pohl, Ulrich Rüde, Markus Oechsner, and Carolin Körner. Optimization and stabilization of lbm free surface flow simulations using adaptive parameterization. *Computers & fluids*, 35(8-9):934–939, 2006.
- [173] Nils Thürey and Ulrich Rüde. Stable free surface flows with the lattice boltzmann method on adaptively coarsened grids. *Computing and Visualization in Science*, 12(5):247–263, 2009.
- [174] Nils Thürey, Ulrich Rüde, and Marc Stamminger. Animation of open water phenomena with coupled shallow water and free surface simulations. In *Proceedings of the 2006 ACM SIGGRAPH/Eurographics symposium on Computer animation*, pages 157–164. Eurographics Association, 2006.
- [175] Jonas Tölke. Lattice boltzmann simulations of binary fluid flow through porous media. *Philosophical Transactions of the Royal Society of London A: Mathematical, Physical and Engineering Sciences*, 360(1792):535–545, 2002.
- [176] Alexander J Wagner. An h-theorem for the lattice boltzmann approach to hydrodynamics. *EPL (Europhysics Letters)*, 44(2):144, 1998.
- [177] Alexander J Wagner. The origin of spurious velocities in lattice boltzmann. *International Journal of Modern Physics B*, 17(01n02):193–196, 2003.
- [178] Yan Wang, Chang Shu, HB Huang, and CJ Teo. Multiphase lattice boltzmann flux solver for incompressible multiphase flows with large density ratio. *Journal of Computational Physics*, 280:404–423, 2015.

- 
- [179] Rodney A Worthing, Joel Mozer, and Guy Seeley. Stability of lattice boltzmann methods in hydrodynamic regimes. *Physical Review E*, 56(2):2243, 1997.
- [180] Xiu Qing Xing, David Lee Butler, and Chun Yang. Lattice boltzmann-based single-phase method for free surface tracking of droplet motions. *International journal for numerical methods in fluids*, 53(2):333–351, 2007.
- [181] YY Yan and YQ Zu. A lattice boltzmann method for incompressible two-phase flows on partial wetting surface with large density ratio. *Journal of Computational Physics*, 227(1):763–775, 2007.
- [182] Wen-An Yong and Li-Shi Luo. Nonexistence of h theorems for the athermal lattice boltzmann models with polynomial equilibria. *Physical Review E*, 67(5):051105, 2003.
- [183] David L Youngs. Time-dependent multi-material flow with large fluid distortion. *Numerical methods for fluid dynamics*, 1982.
- [184] Huidan Yu, Li-Shi Luo, and Sharath S Girimaji. Les of turbulent square jet flow using an mrt lattice boltzmann model. *Computers & Fluids*, 35(8-9):957–965, 2006.
- [185] Zhao Yu, Liang-Shih Fan, et al. Multirelaxation-time interaction-potential-based lattice boltzmann model for two-phase flow. *Physical Review E*, 82(4):046708, 2010.
- [186] Peng Yuan and Laura Schaefer. Equations of state in a lattice boltzmann model. *Physics of Fluids*, 18(4):042101, 2006.
- [187] Junfeng Zhang and Fuzhi Tian. A bottom-up approach to non-ideal fluids in the lattice boltzmann method. *EPL (Europhysics Letters)*, 81(6):66005, 2008.
- [188] Raoyang Zhang, Hudong Chen, Yue Hong Qian, and Shiyi Chen. Effective volumetric lattice boltzmann scheme. *Physical review E*, 63(5):056705, 2001.
- [189] Raoyang Zhang, Xiaowen Shan, and Hudong Chen. Efficient kinetic method for fluid simulation beyond the navier-stokes equation. *Physical Review E*, 74(4):046703, 2006.
- [190] Zhuangming Zhao, Ping Huang, Yineng Li, and Junmin Li. A lattice boltzmann method for viscous free surface waves in two dimensions. *International Journal for Numerical Methods in Fluids*, 71(2):223–248, 2013.

- [191] HW Zheng, Chang Shu, and Yong-Tian Chew. A lattice boltzmann model for multiphase flows with large density ratio. *Journal of Computational Physics*, 218(1):353–371, 2006.
- [192] JG Zhou. A lattice boltzmann model for the shallow water equations. *Computer methods in applied mechanics and engineering*, 191(32):3527–3539, 2002.



---

**Titre :** Étude de l'applicabilité de la méthode de Boltzmann sur réseau aux problèmes hydrodynamiques à surface libre du génie maritime

**Mots clés :** génie maritime, LBM, surface libre, régularisation

**Résumé :** La simulation numérique des écoulements à surface libre pour les applications du génie maritime est un problème qui présente de grands défis dans le domaine de la dynamique des fluides numérique (CFD). On propose dans cette thèse une solution, qui consiste à utiliser la méthode de Boltzmann sur réseau régularisée (RLBM) avec un modèle de surface libre basé sur le volume-de-fluide (VOF), et on étudie sa faisabilité et sa fiabilité.

Les connaissances théoriques de la méthode de Boltzmann sur réseau (LBM) sont présentées dans un premier temps, sur la base d'un développement polynomial d'Hermite et d'une analyse de Chapman-Enskog. De cette perspective, l'idée de la RLBM se résume comme étant la régularisation d'Hermite des fonctions de distribution. Dans les cas tests suivants du vortex de Taylor-Green et de la cavité entraînée, il est vérifié que la RLBM

possède une précision de second ordre et une stabilité améliorée.

On a alors ensuite implémenté le modèle de surface libre dans la RLBM. Sur la simulation d'une onde de gravité visqueuse stationnaire et d'un écoulement de dambreak, il est montré que la régularisation stabilise fortement le calcul en réduisant les oscillations de pression, ce qui est très bénéfique pour obtenir des écoulements à surface libre précis, et que la RLBM n'introduit pas non plus de dissipation numérique supplémentaire.

De plus, une nouvelle méthode de reconstruction des fonctions de distribution à la surface libre est proposée. Le modèle proposé est ainsi plus consistant avec la RLBM, ce qui offre un moyen efficace pour simuler des écoulements à surface libre à un grand nombre de Reynolds en génie maritime.

---

**Title :** Investigation of the applicability of the lattice Boltzmann method to free-surface hydrodynamic problems in marine engineering

**Keywords :** marine engineering, LBM, free-surface, regularization

**Abstract :** The numerical simulation of the free-surface flows for marine engineering applications is a very challenging issue in the field of computational fluid dynamics (CFD). In this thesis, we propose a solution, which is to use the regularized lattice Boltzmann method (RLBM) with a volume-of-fluid (VOF) based single-phase free-surface lattice Boltzmann (LB) model, and we investigate its feasibility and its reliability.

The theoretical insights of the lattice Boltzmann method (LBM) are given at first, through the Hermite expansion and the Chapman-Enskog analysis. From this perspective, the idea of the RLBM is summarized as the Hermite regularization of the distribution functions. On the test-cases of the Taylor-Green vortex and the lid-driven cavity flow, the RLBM is verified to have a 2<sup>nd</sup>-order

accuracy and an improved stability.

The adopted free-surface model is then implemented into the RLBM and validated through simulating a viscous standing wave and a dambreak flow problems. It is shown that the regularization not only strongly stabilizes the calculation by reducing spurious pressure oscillations, which is very beneficial for obtaining accurate free-surface motions, but also does not introduce any extra numerical dissipation.

Furthermore, a new reconstruction method for the distribution functions at the free-surface is proposed. The present model is more consistent with the RLBM, which provides an effective way for simulating high-Reynolds-number free-surface flows in marine engineering.